



Politecnico  
di Torino

ScuDo

Scuola di Dottorato - Doctoral School  
WHAT YOU ARE, TAKES YOU FAR

Doctoral Dissertation  
Doctoral Program in Metrology (35<sup>th</sup> cycle)

# Impedance spectroscopy: non-invasive measurements for human tissues characterization

By

**Isabella Sannino**

\*\*\*\*\*

**Supervisors:**

Prof. Sabrina Grassini, Supervisor  
Prof. Pasquale Arpaia, Co-Supervisor

**Doctoral Examination Committee:**

Prof. Lorenzo Ciani, referee, Università degli Studi di Firenze  
Prof. Lorenzo Scalise, referee, Università Politecnica delle Marche  
Prof. Guido Perrone, Politecnico di Torino  
Prof. Tolou Shokuhfar, University of Illinois Chicago  
Prof. Mario Alovisei, Università di Torino.

Politecnico di Torino  
2023

## **Declaration**

I hereby declare that, the contents and organization of this dissertation constitute my own original work and does not compromise in any way the rights of third parties, including those relating to the security of personal data.

Isabella Sannino

2023

\* This dissertation is presented in partial fulfillment of the requirements for **Ph.D. degree** in the Graduate School of Politecnico di Torino (ScuDo).

*To those who dare to dream even in their darkest days*

## **Acknowledgements**

I would like to acknowledge the Laboratory of Augmented Reality for Health Monitoring (ARHeMLab) of the Università degli Studi di Napoli, Federico II, for the collaboration on the topics related to the research in diabetology.

I would like to extend my sincere thanks to Centro di Eccellenza per la Ricerca, la Didattica e l'Assistenza in Campo Odontostomatologico - Dental School of Università degli studi di Torino. I also express my gratitude to Professor Nicola Scotti, for the collaboration on the topic related to carious lesions detection and for his support during the research activities.

## **Abstract**

Impedance spectroscopy is considered a powerful, painless, and harmless measurement technique in many medical fields. This dissertation focuses on the application of impedance spectroscopy in medicine, by paying particular attention to drug bioavailability assessment and tissue characterization.

Diabetes is one of the most widely spread non-communicable chronic diseases worldwide, thus full control of blood glucose concentration is a challenge with a relevant clinical, social, and economic impact. To date, instruments capable to measure in-vivo the delivered amount of insulin immediately after administration have not been developed. The most popular methods for assessing insulin bioavailability are often invasive or have high latency. Thus, the demand for painless and non-invasive analytical methods to achieve effective glucose monitoring in diabetics is significantly increasing.

An insulin meter, based on an on-chip transducer, for real-time non-invasive monitoring of insulin absorption is presented. The instrument, prototyped by using off-the-shelf components, analyses the electrical impedance in the frequency domain and its variations over time in order to monitor the diffusion of insulin from the administration site. The instrument was metrologically characterized in the laboratory, in-vitro, and ex-vivo. The insulin bioavailability is assessed non-invasively and in real-time, after the administration in a specific injection site, of a known amount of drug, as in common diabetic therapy. The Insulin Meter implements a personalized model identification by measuring step by step the impedance variation corresponding to the injection of a known amount of insulin, improving thus the inter-and intra-individual reproducibility.

Then, with the aim to improve the sensitivity of the measurement method, a numerical model of the tissue based on “Finite Element Method” is proposed for the measurement of insulin transdermal delivery. In order to improve the accuracy of the insulin absorption assessment, an experimental campaign was carried out to assess

---

the impact of mechanical stresses acting on the human abdomen on the impedance spectroscopy, in particular, due to the pressure exerted during the injecting phase and the tissue defamation because of breathing.

Furthermore, tissue characterization by impedance spectroscopy has been applied to dental disease assessment. In particular, a simple automatic approach for the assessment of tooth demineralization, which represents the earlier stage of the dynamic carious process, was developed. The proposed approach based on impedance measurements and classification algorithms was tested and validated in-vitro. The possibility to use of impedance spectroscopy measurements in caries detection is based on the typical loss of mineral components due to the caries process, resulting in an increased porosity of the tooth structure, which entails a higher liquid content than healthy tissue. In parallel, a dental tissue characterization by scanning electron microscopy and Raman spectroscopy to assess demineralized and sound teeth was performed.

This work proved the possibility to discriminate between sound and demineralized teeth, and thus the carious lesion, by using impedance spectroscopy measurements. Therefore, impedance measurement can be considered an additional diagnostic method in dental practice thanks to its safety, reliability, simplicity, rapid response, cost-effectiveness, robustness, and adequate detection limit. Further work will include the development of a low-cost device for in-vivo application in dental practices.

Thus, the objective of the research work presented in this dissertation is to propose impedance spectroscopy measurement as an additional tool in different medical applications. It has been pursued, in diabetology, by developing a new instrument able to detect non-invasively the amount of insulin absorbed by the tissue. In dentistry, a non-invasive and fast approach for assessing dental caries has been proposed.

# Preface

This Ph.D. thesis addresses the use of impedance spectroscopy as a new possible measurement approach in some medical applications, in particular in diabetology and dentistry.

About diabetology, motivations for this research work can be found in the lack of scientific literature on specific methodology to non-invasively and in real-time assess the amount of insulin absorbed during the injection, at the injection point. Despite diabetes relevant clinical, social, and economic impact, and above all, its importance for the health of numerous diabetic patients. Thus, this research work proposes an instrument able to face the increasing demand for non-invasive analytical methods to achieve effective glucose monitoring to implement in the newest artificial pancreas, in order to customize insulin therapies.

As far as concerned dentistry, also in this case, despite the impedance spectroscopy finds application in several medical and industrial fields, it is not employed in dental practice, in particular for caries detection. Therefore, this research work proved the possibility to discriminate between sound and demineralized teeth, and thus the carious lesion, by using impedance spectroscopy measurements. Providing, thus, to the dentists a non-invasive, safe, reliable, simple, cost-effective, and with rapid response additional diagnostic method.

The dissertation work is organized as follows:

**Chapter 1** This chapter provides an overview of the different applications of impedance spectroscopy in medicine, by paying particular attention to drug bioavailability assessment and tissue characterization.

**Chapter 2** This chapter deals with a measurement method for assessing insulin bioavailability in diabetology. In the first part, an Insulin Meter, based on an on-chip transducer, for real-time non-invasive monitoring of insulin absorption is presented

## Preface

---

and metrologically characterized in laboratory, in-vitro, and ex-vivo. The second part of the chapter describes a numerical model of the tissue based on FEM, proposed to improve the sensitivity of the previous measurement method and to experimentally identify a relationship between applied force and impedance measurements.

**Chapter 3** This chapter describes a simple automatic approach for the assessment of tooth demineralization, and carious lesions, by using impedance spectroscopy measurements. Dental tissues are characterized also by SEM and Raman Spectroscopy.

**Chapter 4** This last chapter summarises the results obtained during the different studies, reporting the main contributions to the development of a new measurements method for impedance tissue characterization.



# Contents

<b>Preface</b>	<b>vii</b>
<b>List of Figures</b>	<b>xii</b>
<b>List of Tables</b>	<b>xix</b>
<b>1 Impedance measurements in biomedical applications</b>	<b>1</b>
1.1 Impedance of human tissues . . . . .	1
1.2 Impedance measurements in diabetology . . . . .	7
1.3 Impedance measurements in dentistry . . . . .	13
<b>2 Impedance measurements in diabetology</b>	<b>20</b>
2.1 Insulin measurement in diabetology . . . . .	20
2.1.1 Basic Idea . . . . .	23
2.1.2 Measurement method . . . . .	24
2.2 Insulin Meter . . . . .	25
2.3 Design . . . . .	25
2.3.1 Architecture . . . . .	26
2.3.2 Operation . . . . .	26
2.3.3 Bioavailability monitoring . . . . .	28
2.4 Realization . . . . .	29

## Contents

---

2.4.1	Hardware, firmware, and software . . . . .	30
2.4.2	Calibration . . . . .	34
2.5	Metrological characterization of the Insulin Meter . . . . .	35
2.5.1	In-vitro metrological characterization of the Insulin Meter .	35
2.5.2	Ex-vivo metrological characterization . . . . .	44
2.6	Conclusions . . . . .	46
2.7	Measurement method optimization by FEM modeling . . . . .	47
2.7.1	Insulin injection site . . . . .	48
2.7.2	Tissues mechanical properties . . . . .	51
2.7.3	Numerical modeling . . . . .	53
2.7.4	Tissues electrical properties . . . . .	56
2.8	Experimental activity . . . . .	60
2.8.1	Data processing . . . . .	63
2.8.2	Conclusions . . . . .	64
<b>3</b>	<b>Impedance measurements in dentistry</b>	<b>66</b>
3.1	Human teeth structure: anatomy and composition . . . . .	66
3.1.1	Tooth anatomy . . . . .	68
3.1.2	Tooth composition . . . . .	70
3.2	Tooth demineralization . . . . .	72
3.2.1	Dental caries . . . . .	74
3.3	Cariou lesion detection: Experimental procedure . . . . .	76
3.3.1	Impedance Measurements and Data Acquisition . . . . .	79
3.3.2	Equivalent Electrical Circuit . . . . .	84
3.4	Demineralization: Experimental procedure . . . . .	86
3.4.1	Raman Spectroscopy . . . . .	88
3.4.2	Scanning Electron Microscopy (SEM) . . . . .	101

3.4.3	Impedance Measurements and Data Acquisition . . . . .	102
3.4.4	Equivalent Electrical Circuit . . . . .	109
3.4.5	Classification Algorithm . . . . .	113
3.4.6	Performance evaluation of multiple classifiers . . . . .	116
<b>4</b>	<b>Conclusions</b>	<b>129</b>
	<b>References</b>	<b>133</b>

# List of Figures

1.1	Equivalent circuit of human skin impedance measurement [1]. . . .	5
1.2	Schematic representation of the main components of human skin [1].	6
1.3	Different insulin devices: insulin pen, syringe with a vial of insulin, glucometer and test strips, infusion set, and lancing device [1]. . . .	9
1.4	Glucometer with pen blood lancet and test strip. A drop of blood, collected by pricking the finger with the lancet, is spilled on a disposable test strip and then analyzed by the device. Finally, the device displays the blood glucose level in units of mg/dL or mmol/L [1]. . .	10
1.5	Glucowatch (A) and Pendra (B) continuous glucose monitors [1]. . .	13
2.1	Artificial Pancreas components schematic representation [1]. . . .	21
2.2	On the left, lipohypertrophic lesions below the navel [2], on the right a typical insulin injection on the abdomen [1]. . . . .	22
2.3	Schematic representation of insulin measurement method phases [1].	24
2.4	Architecture of the Insulin Meter [3]. . . . .	26
2.5	Model of insulin appearance: the linear relationship between the percentage impedance variation and the amount of insulin [1]. . . .	28
2.6	Insulin appearance personalized model used to assess the disappearance of insulin [1]. . . . .	29
2.7	Insulin Meter Prototype board: motherboard ADuCM350 Vers.A with (A) daughterboard BIO3Z for 4-wire bioimpedance measurement, (B) battery, (C) ON and Reset buttons, and (D) display [3]. . .	31

2.8	Daughterboard schematic, in red the three resistors in series that limit the current (RCALi, input for the calibration resistor, $AN_A$ , the auxiliary channels, and AFEi, inputs for the analog front-end) [4]. . . . .	32
2.9	Insulin Meter user interface [1]. . . . .	33
2.10	Impedance magnitude at 1 kHz at varying the resistance value of the RC loop: theoretical trend (continuous line), Insulin Meter ( $\times$ ), and reference LCR Meter (+) [1]. . . . .	35
2.11	Example of insulin injection on eggplant. . . . .	37
2.12	In-vitro drift (average on 10 measurements) in four-wires (+) and in two-wires ( $\times$ ) configuration [1]. . . . .	39
2.13	Impedance percentage magnitude variation vs the amount of insulin for in-vitro experiments in 5-mm setup. . . . .	39
2.14	Impedance percentage magnitude variation vs the amount of insulin for in-vitro experiments in 12-mm setup. . . . .	40
2.15	Example of $1-\sigma$ repeatability according to the amount of injected insulin in-vitro for the 5 mm. . . . .	42
2.16	Example of $1-\sigma$ repeatability according to the amount of injected insulin in-vitro for the 12 mm. . . . .	42
2.17	Percentage accuracy of the personalized (+) and the generic ( $\times$ ) model vs the amount of insulin, in-vitro experiments for A) the 12-mm and B) the 5-mm setup. . . . .	43
2.18	Example of a typical impedance percentage magnitude variation according to the insulin in ex-vivo experiments [1]. . . . .	44
2.19	Percentage accuracy of personalized (+) and generic ( $\times$ ) model vs amount of drug in ex-vivo experiments [1]. . . . .	45
2.20	Insulin absorption rate according to the different injection sites. . . . .	48
2.21	Human abdomen stratification and insulin injection. . . . .	50
2.22	The Finite Element Model of abdominal portion [5]. . . . .	52
2.23	Abdominal portion total displacement: A) at frequency= 19.76 Hz B) at frequency= 27.32 Hz [5]. . . . .	55

## List of Figures

---

2.24	$\Delta Z$ [%] vs distance between Voltmetric electrodes. . . . .	60
2.25	Optimal electrodes configuration. . . . .	60
2.26	Experimental set up including: Analog AduCM350, dynamometer, electrodes FIAB PG 500, tripod, and camera. . . . .	61
2.27	Picture of volunteer's abdomen on the left; Impedance magnitude time-trace at 10 kHz. Impedance variation due to four cycles of compression and relaxation of the tissue, on the right [6]. . . . .	62
2.28	Impact of breathing intensity on impedance measurements. Normal breathing a, strong breathing b) [6]. . . . .	63
2.29	Average percentage impedance magnitude variation during force application. . . . .	63
2.30	Impedance variation in function of the applied increasing and decreasing force. . . . .	64
3.1	Maxillary and mandibular adult arches representation. The two arches are divided into 2 sub-arches or four quadrants (red), divided by the median sagittal plane. Teeth are numbered sequentially starting from the right maxillary third molar (number 1 black) or according to the quadrant, from mesial to distal in each quarter (red numbers). Teeth orientation are: labial, buccal, lingual, and palatal [7].	67
3.2	Teeth present in the dental arch of adults: the incisors (4), the canines (2), the premolars (4), and the molars (6). With 16 teeth in the maxilla, the bony upper part of the jaw, and 16 teeth in the mandible, the bony lower part of the jaw. . . . .	68
3.3	Normal tooth anatomy and a cross-section view. . . . .	70
3.4	SEM image of the organized enamel rods (prism) after dental enamel demineralization, residual hydroxyapatite crystallises show a rod-like morphology in the lesion on the enamel surface. . . . .	72
3.5	ICDAS clinical visual codes, based on evidence of the histological severity of carious lesions at different caries stage [8]. . . . .	75

3.6	Impedance measurements experimental setup: the measuring cell includes the examined tooth, placed in 3D-printed PLA support, partially immersed in the solution, mainly physiological saline solution; the working electrode on the tooth surface while the counter electrode is in the solution; both electrodes connected to a computer-controlled Potentiostat [9]. . . . .	78
3.7	Extracted sound tooth on the left; on the right extracted decayed tooth with a carious lesion in correspondence of green arrow D3, while D1 and D2 are sound enamel areas. . . . .	80
3.8	Impedance spectra, represented as Bode diagrams, of a carious tooth. Black and red lines, respectively D1 and D2, are the spectra collected on an intact area of the tooth. The green line, i.e. D3, spectrum collected in correspondence of a carious lesion [9]. . . . .	80
3.9	Red lines: different measurements performed on multiple points of the same decayed tooth. Black lines: different measurements performed on multiple points of the same sound tooth [9]. . . . .	81
3.10	Measurements collected using the agar probe. Red lines: measurements collected on different points of multiple decayed teeth. Blue lines: measurements collected on different points of multiple sound teeth [10]. . . . .	82
3.11	Frequency at which the impedance phase reaches $-45^\circ$ both for sound teeth (black icons) and carious teeth ( red icons). Different markers correspond to different teeth [9]. . . . .	83
3.12	Equivalent electrical circuit that models impedance spectra collected on sound and demineralized teeth [9]. . . . .	85
3.13	Lower central incisor cut and covered with the protective coating but a selected window. . . . .	87
3.14	Representative Raman spectra collected on one healthy and one demineralized tooth. On the left the spectra in the range $200\text{ cm}^{-1}$ - $2000\text{ cm}^{-1}$ , while on the right an enlarged section is shown, in the range $800\text{ cm}^{-1}$ - $1200\text{ cm}^{-1}$ . . . . .	91

## List of Figures

---

3.15	Portable modular spectrometer by BWTEK used to perform Raman analysis. . . . .	92
3.16	Raman spectra of enamel, with the corresponding vibrational modes (v: stretching vibration) of the peaks considered for data elaboration.	92
3.17	Example of a spectrum processing with a Lorentzian fitting. . . . .	94
3.18	Average intensity peak at $960\text{ cm}^{-1}$ of different samples before (red) and post demineralization (red). . . . .	95
3.19	Box plot of average intensity peak at $960\text{ cm}^{-1}$ of different samples before (green) and after demineralization (red). . . . .	96
3.20	On the left: Box plot of Average FWHM at $960\text{ cm}^{-1}$ ; on the right: Box plot of Average Area at $960\text{ cm}^{-1}$ , for both red are teeth before the demineralization, while greed teeth post demineralization. The horizontal lines are the minimum and the maximum values, the median is the line that divides the box into two parts, and the square in the middle of the box is the mean value. The upper line of the box is the upper quartile, it indicates that 75% of the data fall below the upper quartile. The bottom line of the box is the lower quartile, it represents the 25% of data that fall below the lower quartile. × represents the 99% and 1% percentile. . . . .	96
3.21	Average crystallinity before (red) and post demineralization (green) of different samples. . . . .	97
3.22	Box plot of Average intensity Crystallinity of different samples before (green) and after demineralization (red). The horizontal lines are the minimum and the maximum values, the median is the line that divides the box into two parts, and the square in the middle of the box is the mean value. The upper line of the box is the upper quartile, it indicates that 75% of the data fall below the upper quartile. The bottom line of the box is the lower quartile, it represents the 25% of data that fall below the lower quartile. × represents the 99% and 1% percentile. . . . .	98
3.23	Demineralization Degree. . . . .	99
3.24	Crystallinity variation according to the Demineralization Degree. . . . .	99



## List of Figures

3.25	Crystallinity variation according to the intensity peak at $960\text{cm}^{-1}$ . . . . .	100
3.26	Carbonate Phosphate ratio Before (red) and Post demineralization (green). . . . .	100
3.27	Scanning electron microscope (SEM) images of healthy enamel on the left and demineralized enamel surface on the right. . . . .	102
3.28	Impedance spectra collected on a demineralized tooth. Spectra were collected on three different areas on the tooth surface, before and after demineralization. A phase shift of about one decade due to demineralization is clearly visible. . . . .	103
3.29	Impedance spectra collected on a non-demineralized tooth. Spectra were collected on three different areas on the tooth surface, before and after the demineralization treatment. No significant phase shift is visible in the spectra: the measurement area did not exhibit any demineralization. . . . .	104
3.30	Impedance spectra collected on a non-demineralized tooth. Spectra were collected on three different areas on the tooth surface, before and after the demineralization treatment. In this case, no significant phase shift is visible in the spectra. . . . .	105
3.31	Scanning electron microscope (SEM) image of tooth enamel surface post demineralization treatment unevenly demineralized . . . . .	106
3.32	SEM image of tooth enamel surface post demineralization treatment. . . . .	107
3.33	Frequency at which the impedance phase reaches $-45^\circ$ both for demineralized teeth (in red) and for before demineralization (in green) . . . . .	108
3.34	Equivalent electric circuit used to model the impedance spectra acquired on the teeth. . . . .	109
3.35	Bode diagrams, on the left, and Nyquist diagram, on the right, of a tooth before demineralization modeled through Ivium software, blue dots are experimental data, while the continuous line represents the model. . . . .	110
3.36	Bode diagrams, on the left, and Nyquist diagram, on the right, of a demineralization tooth modeled through Ivium software, blue dots are experimental data, while the continuous line represents the model . . . . .	111

## List of Figures

---

3.37	Caption . . . . .	112
3.38	The used classifier with an inverted sigmoid as decision function [11].	114
3.39	"First plot shows the average phase of all samples, where blue dots represent measurements carried out before the demineralization, while orange dots post-demineralization. The bottom plot shows average phase difference before and after demineralization for each frequency. The frequency spans in the range 1 Hz to 1 kHz. The highest value of average phase difference is achieved at a frequency of about 15 Hz." [11] . . . . .	115
3.40	Employed classifier results. Blue dots: the predicted values of the neural network on all the samples. Orange dots: the expected values. Classification errors are marked by red circles. [11] . . . . .	116
3.41	Result of the Nearest Neighbors classifier with 82.2% accuracy. Red dots are not-demineralized teeth while blue dots are demineralized teeth. . . . .	118
3.42	Result of Linear SVM with linear Kernel classifier with accuracy 76%	119
3.43	Result of Radial Basis Function SVM with 79% accuracy . . . . .	120
3.44	Result of Gaussian Process classifier with 76.0% accuracy. . . . .	121
3.45	Result of the Decision tree classifier with 74.0% accuracy. . . . .	122
3.46	Result of Random Forest classifier with 80.0% accuracy. . . . .	123
3.47	Result of Neural Net Multilayer Perceptron classifier with 77.2% accuracy. . . . .	124
3.48	Result of Ada Boost classifier with 79.0% accuracy. . . . .	125
3.49	Result of Gaussian Naive Bayes classifier with 76.0% accuracy . . .	126
3.50	Result of Quadratic Discriminant Analysis with 75% accuracy. . . .	127
3.51	Results of performance of each classifier: F-score (blue), Recall (pink), and Precision (grey). . . . .	128

# List of Tables

2.1	Nonlinearity of the Insulin Meter for the 5-mm setup . . . . .	41
2.2	Metrological parameters of pig abdominal non-perfused muscle and eggplants. [1] . . . . .	45
2.3	Mechanical and Anatomical parameters. . . . .	52
2.4	First Natural Frequencies of human abdomen tissues. [5] . . . . .	55
2.5	Different tissues parameters value of Cole-Cole equation according to Gabriel [12]. . . . .	59
2.6	Means characteristics of volunteers enrolled in the study. . . . .	60
3.1	Risk factors associated with tooth demineralization. . . . .	73
3.2	Equivalent electrical circuit parameters computed for a tooth with carious lesion, where D3 is the area with carious lesion (results coming from the spectra reported in Fig. 3.8) . . . . .	86
3.3	Equivalent electrical circuit parameters computed for a tooth before and after demineralization (results coming from the spectra reported in Fig. 3.28) . . . . .	111
3.4	Percentage variation relative to the equivalent electrical circuit parameters reported in Table 3.3 . . . . .	112
3.5	Equivalent electrical circuit parameters computed for a tooth before and after demineralization (results coming from the spectra reported in Fig. 3.37). . . . .	112

## List of Tables

---

3.6	Percentage variation relative to the equivalent electrical circuit parameters reported in Table 3.5. . . . .	113
3.7	Average Nearest Neighbours classifier's performance. . . . .	118
3.8	Support Vector Machine with linear Kernel classifier's performance. . . . .	119
3.9	RBF SVM classifier's performance. . . . .	120
3.10	Gaussian Process classifier's performance. . . . .	121
3.11	Decision tree classifier's performance. . . . .	121
3.12	Random Forest classifier's performance. . . . .	122
3.13	Multilayer Perceptron Neural Net classifier's performance. . . . .	124
3.14	Ada Boost classifier's performance. . . . .	125
3.15	Gaussian Naive Bayes classifier's performance. . . . .	126
3.16	Quadratic Discriminant Analysis classifier's performance. . . . .	127
3.17	Performance of different classification algorithms. . . . .	128

# Chapter 1

## Impedance measurements in biomedical applications

Some of the work described in this chapter has been previously published in [1], [9], [10].

### 1.1 Impedance of human tissues

Biological organisms and their component organs, tissues and cells have specific electrical impedance properties. Under alternating electrical excitation, biological tissues are characterized by a complex electrical impedance that depends on tissue composition, structures, health status, applied signal frequency, and amplitude. The injected electrical current, used for impedance measurements, and that crosses the biological tissues under test is harmless, thus, it causes no damage or alterations of any kind to the tissues. It means, from a physiological point of view, that no excitable tissue should be stimulated, such as nerve or muscle, especially skeletal, cardiac, or smooth. Hence, impedance spectroscopy may be considered a powerful method, painless and harmless, for characterizing the biophysical features of the tissues.

The electrical proprieties of biological tissues depend both on the microscopic structure of cellular media, and the physiologic and pathological state of the tissue. Thus, the impedance varies from tissue to tissue and subject to subject, so the electrical proprieties of biological tissues differ due to the type of considered tissue.

## **Impedance measurements in biomedical applications**

---

Specifically, tissue structure, composition, and health status as well as applied signal frequency, amplitude, and measurement direction, since most tissues are anisotropic.

Impedance measurement methods can successfully investigate the physiological or pathological status of biological tissues, therefore, they are very used in a lot of different medical fields. In the following section, some examples of different impedance medical applications are shown.

In the last decades, electrical impedance systems have been developed for general or targeted medical applications. Among these applications, one of the most popular is Electrical Impedance Tomography (EIT), a medical imaging technique used for continuous real-time lung aeration monitoring [13], and still in pneumology, for monitoring patients during mechanical lung ventilation [14].

"More in general, bioelectrical impedance analysis (BIA) is a useful tool in clinical practice, as it allows to evaluate the biological fluid amount. In particular, the alteration in the patients' hydration by pathological conditions such as hemodialysis [15] or ambulatory peritoneal dialysis [16], and liver cirrhosis [17] can be assessed. Another well-established approach, which includes impedance of extremities in the cardiology field, is limb Impedance Plethysmography (IPG), that has found a remarkable place in clinical practice. IPG measures variation in the electrical impedance corresponding to a change in the blood volume of a specific body segment, say chest, calf, or any other regions of the body. In particular, IPG can be used to measure blood flow in a limb or digit; hence, this technique has been widely applied for the evaluation of patients at risk or suspected to have lower extremity Deep Venous Thrombosis (DVT) [18].

In brief, IPG is easy to perform and turns out to be non-invasive compared to venography; it does not require a skilled operator and can help physicians to detect alteration in blood flow, DVT, arterial and veins insufficiency or occlusive disease, blood clots in limbs or pulmonary emboli [19, 20]. IPG represents an alternative that allows the study of the cardiovascular system in a totally non-invasive and risk-free way for patients." [1]

A further application in cardiology, which uses the characteristic impedance of the blood and tissue in the thorax, that changes with respiration and the cardiac cycle, largely due to the changes in thoracic vascular volume, is Thoracic Electrical Bioimpedance (TEB), also known as Impedance Cardiography (ICG).

"The ICG is essentially similar to the IPG procedure: one pair of electrodes, usually placed at the base of the neck, injects an alternating electric current (frequency

## 1.1 Impedance of human tissues

---

range of 20 kHz-100 kHz). Correspondingly, another two electrodes, placed on the xiphoid or xiphisternal joint, measure the related voltage. TEB depends on biological composition, breathing, blood circulation, and blood volume of thoracic vessels. After processing to remove the respiratory component, the change in impedance from the baseline impedance,  $Z_0$ , is related to the cardiac cycle. Therefore, the analysis of  $Z_0$  allows to evaluate the heart health status along with calculations of certain hemodynamic parameters including stroke volume, cardiac output, cardiac index, systemic vascular resistance, and left work index [21, 22]."[1]

Some other applications of impedance include the opportunity to use BIA in Sports Medicine, to assess physical performance and evaluate athletes' muscle strength and sports performance as well as efficiency [23, 24]. Because impedance measurements can assess changes in the volume, or fluid distribution of tissues, related to physiological activities. While in nutrition, BIA has many characteristics of an ideal technique for studying body composition [25] but is also a key factor for general human health status evaluation. "In clinical practice, measurement of total body bioimpedance is the most broadly used method for quickly estimating whole body compartments, in terms of total-body water, fat-free mass, fat mass, or other body compartments [26]."[1]

Considering impedance application in dermatology, impedance measurements are used to investigate various diseases and evaluate the effectiveness of medicament, to investigate different pathologies, and evaluate the effectiveness of medical treatments [27]. While in cosmetology impedance measurements are used to monitor the hydration level of the skin, namely the water content, which determines the skin smoothness and softness, whose assessment is useful to evaluate the function of anti-aging and miniaturization treatments in cosmetology [28].

Indeed, impedance measurement varies from a healthy to a diseased tissue allowing thus to discriminate between cancerous and healthy tissues [29]. Some devices which exploit impedance measurements are used to differentiate between malignant melanoma and benign skin lesions [30].

Actually, healthy and cancerous tissues differ morphologically; this difference is reflected in a change of electrical proprieties. As a matter of fact, blood is a good conductor of electricity, and the cancerous tissue, in order to grow faster and uncontrolled, needs more blood than healthy tissue. Therefore, this latter, less rich in blood, shows higher impedance.

## Impedance measurements in biomedical applications

---

Impedance spectroscopy provides a method for the detection of early changes in extracellular fluid. Lymphedema affects the lymphatic system and it is characterized by the accumulation of protein-rich fluid in the interstitial spaces. This fluid build-up might result in swelling in various areas of the body and cause discomfort [31]; moreover, it is often a side effect of cancer treatments. Thus, impedance spectroscopy represents a practical and reliable method for documenting the presence of lymphedema, especially for the follow-up of patients under treatment for cancer [32].

Above all, in order to improve the characterization of human tissues is imperative to enhance the comprehension of the impedance characteristics of the skin, as well as to optimize the skin impedance models.

As already mentioned, "the most promising techniques for the characterization of the physiological and structural properties of biological tissues are based on the evaluation of the electrical conduction phenomena within them. In particular, Electrical Impedance Spectroscopy (EIS) measurements [33][34] are in fact absolutely non-destructive and low invasive. Basically, EIS applies low-intensity electric currents, over a wide frequency range, to provide more meaningful independent information on the electrical characteristics of a tissue. In general, electrical models of the tissues are developed and identified using EIS. In EIS experiments, the perturbation is constituted by a sinusoidal signal of slight amplitude, from tens to hundreds of mV [35] of a sinewave  $\Delta E_{sen}(\omega t)$  superimposed on a continuous bias voltage,  $E_0$ . The system response to this perturbation is a sinusoidal current:  $\Delta I_{sen}(\omega t - \phi)$ .

To obtain a linear response of the tissue, a sufficiently small amplitude of the applied signal is chosen. By varying the frequency of the applied voltage, the impedance of the material under examination is obtained as a function of the frequency. The spectrum of this impedance is typically represented graphically by means of the Bode and Nyquist diagrams."[1]

"In this type of experimental investigation, two main sources of uncertainty are highlighted: the electrode polarization and the inductance of the conductor cables. They occur at different frequency intervals: for low frequency ( $<100$  Hz), the burden of the electrode polarization is dominant, while for high frequency ( $>1$  MHz), the inductance of the cable involves significant uncertainty. However, suitable mathematical models to correct the deterministic part can be defined, starting from the actual measurement data. These models return a set of values for the parameters under consideration, used to derive an equivalent circuit model as close as possible



## 1.1 Impedance of human tissues

to reality. Obviously, there are some peculiarities in the electrical properties of biological tissues. Firstly, in biological tissues, the charge carriers of electric currents are represented by ions. For this reason, the conductivity of biological tissues is strongly dependent on parameters such as concentration, effective charge, diffusion coefficients, and the types of ions involved in the process. In electrical circuits, the current density does not affect the properties of the circuit (at least up to about  $100 \text{ A/cm}^2$ ) and passive circuits follow Ohm's law. On the other hand, the linearity of the tissues properties is considered as constant until the injected current does not exceed  $1 \text{ mA/cm}^2$  (this value is also a function of the frequency). Therefore, the need to identify a linearity region is evident."[1]

"Although the properties of electronic circuits and biological tissues are different, the latter can be described by means of suitable circuit models. The experimental results of the impedance spectroscopy of a tissue can be analyzed in terms of an equivalent electrical circuit model [36, 37], in order to find the impedance equals or that reflects the measured data. The type of electrical components of the model and their interconnections control the shape of the impedance spectrum of the model. In an electrical model, each component represents a physical process of conduction within and on the surface of the biological tissue. The choice of the model derives from the knowledge of its characteristics. The same impedance spectrum can be modeled by multiple equivalent electrical circuits, so the model must be selected correctly before its use."[1]

"The impedance of biological tissue can be measured starting from an interaction between an electric current with the tissue at cellular and molecular level. The electrical properties of skin have been studied for over a century. An equivalent circuit, with a resistor ( $R_e$ ) in series with the parallel of a resistor ( $R_{skin}$ ) and a particular capacitor ( $CPE$ ), has been used successfully to describe the skin's electrical properties (Fig. 1.1)."[1] "In this model,  $CPE$  is a pseudo-capacitance, represented by

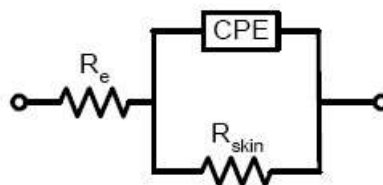


Fig. 1.1 Equivalent circuit of human skin impedance measurement [1].

## Impedance measurements in biomedical applications

---

a special element, called Constant Phase Element (*CPE*), as described by Cole-Cole [38]. It represents the properties of the stratum corneum, the skin's most superficial layer. Conversely,  $R_e$  represents the resistance associated with the deeper tissues. From this circuit, more complex linear and non-linear circuits have been proposed in order to model skin's electrical properties more closely. Additional resistors and capacitors, as well as inductors, voltage sources, and diodes, have been involved. Nevertheless, the abovementioned circuit has proved to be an optimal linear model, where additional resistors and capacitors do not provide statistically significant improvement." [1]

Since the electrical impedance is strictly connected to the physiological and chemical structure of the tissue under test, a deep knowledge of the skin anatomy is required.

"Skin impedance is an important aspect of bioimpedance and can be used to analyze the condition of the human body. Accurate researches have been carried out on a combination of skin characteristics and bioimpedance parameters [39, 37]." [1]

"The skin is the most extensive organ of the human body, with an average surface area, in adults, of almost 2 m<sup>2</sup>. The skin is extremely dynamic, due to its ability to absorb mechanical stress, prevent excessive loss of liquids, facilitate heat exchange, protect from sun radiation, and so on. Such a wide variety of functions are ensured by three superimposed layers of different chemical composition and morphological structure (Fig. 1.2): the *dermis*, the *viable epidermis* and the *stratus corneum*.

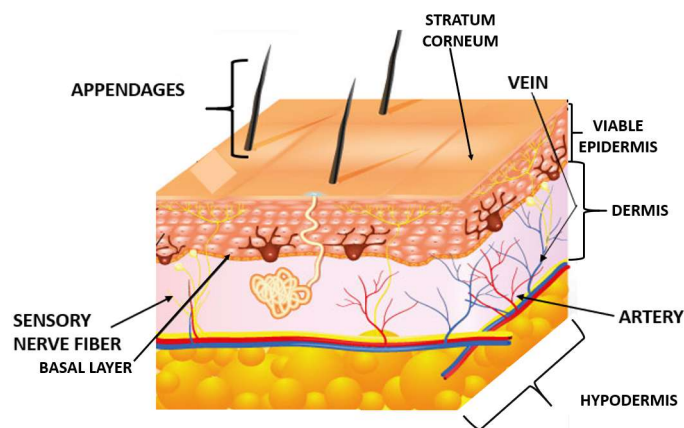


Fig. 1.2 Schematic representation of the main components of human skin [1].

The deepest part of the skin is the *dermis* (or corium), which nourishes and supports the epidermis, with thickness varying from about 500  $\mu\text{m}$ -2000  $\mu\text{m}$  according

## 1.2 Impedance measurements in diabetology

---

to the body site [40]. It contains a connective tissue, formed from an interwoven network of collagen and elastic fibers. The dermis contains numerous blood and lymph vessels, nerves, nerve endings, and sweat glands, providing the transpiration and the base of the pilosebaceous system. In transdermal drug delivery applications, drugs are supposed to be preliminary carried into the dermis and then into blood vessels.

The next layer is called *viable epidermis*, with thickness also greatly variable, around 150  $\mu\text{m}$ . It is divided into four sublayers vertically: *stratum lucidum*, *stratum granulosum*, *stratum spinosum*, and *stratum basale* [41]. The viable epidermis is hydrophilic since it is composed by 40% of protein, around 40%-60% of water, and lipid, and besides, there are no blood vessels [42].

The stratum corneum is the most superficial layer of the skin. It consists of flat cells and corneocytes, which are dead cells without nuclei, embedded into a highly-ordered and dense lipid matrix, which form an impermeable lining and a natural barrier in transdermal transport [43, 44]. This barrier allows the retention of water inside the body and guarantees protection from external substances, such as toxins and microorganisms. The thickness of the stratum corneum varies considerably among different individuals and different body sites. As an example, the thickness of the forearm is about 10  $\mu\text{m}$  - 40  $\mu\text{m}$  [45]. Moreover, it has been proven that the stratum corneum has a negative charge [46, 47], which promotes the transport through the skin of cations rather than anions. Additionally, the skin has a pH between 3 and 4 [48, 44]. Therefore, some techniques such as mesoporation and iontophoresis, which exploit both the negative charge and the pH of the skin, can be used in order to increase its permeability. In brief, the stratum corneum properties highly affect the measurement of skin impedance and the assessment of skin permeability due to its peculiar physiological structure."[1]

Finally, "a better understanding of the impedance characteristics of the skin, as well as the optimization of the skin impedance models, are imperative in order to optimize the evaluation of the tissue health status"[1]

## 1.2 Impedance measurements in diabetology

"Diabetes is one of the most spread non-communicable diseases worldwide. Globally, the number of people with diabetes, according to International Diabetes Federation, is

## **Impedance measurements in biomedical applications**

---

currently around 463 million and is expected to increase to 700 million by 2045. This disease is the fifth leading cause of death in most developed countries; after all, four million deaths are related to diabetes and its complications [49]. Diabetes treatment and related complications costs affect health services and national productivity, as well as individuals and families. Its financial burden has a relevant impact on the economy of the society.

Strictly speaking, diabetes is a condition that impairs the body's ability to process blood glucose, otherwise informally known as "blood sugar". Blood glucose is one of the main energy sources of our body and it derives principally from food intake. The hormone, which promotes the absorption of glucose from the blood into cells to be used for energy, is the insulin produced by the islets of Langerhans of the pancreas. When our body does not produce insulin, or its amount is not sufficient, the glucose is not able to reach the cells, and over time, its accumulation in the blood can cause serious health problems.

Different kinds of diabetes can occur, and managing the condition depends on the type. Not all diabetes forms arise from obesity or unhealthy lifestyle but appear also in childhood indeed. Although there is no permanent cure, diabetes can be managed and patients can stay healthy. The most common types of are type 1, type 2, and gestational diabetes. Among them, people with type-1 diabetes are insulin-dependent: they must take artificial insulin daily to stay alive since their body fails to produce it. Therefore, the frequent monitoring of blood glucose concentration is a crucial part of diabetic management. Nowadays, insulin treatment strategies consist of either multiple-daily insulin injections or continuous subcutaneous insulin infusion with a pump.

Patients with chronic conditions, such as diabetes mellitus, require self-management in homecare settings; in fact, the self-monitoring of blood glucose (SMBG) (by the patient themselves or with the assistance of relatives), in daily life, is made by a blood strip and a lancing device (Fig. 1.3). Although devices tend to be almost fully automated and require only a few simple user operations to go from sample preparation to test results, frequent finger pricks can become rather painful if a regular monitoring is necessary [50].

Despite modern devices (smaller, more reliable, with reduced blood sample requirement, faster) and easier to use compared to those used about 15 years ago, there is an increasing demand for non-invasive analytical methods to achieve ef-

## 1.2 Impedance measurements in diabetology

---



Fig. 1.3 Different insulin devices: insulin pen, syringe with a vial of insulin, glucometer and test strips, infusion set, and lancing device [1].

fective glucose monitoring in diabetics. A painless device would motivate people suffering from diabetes to monitor their glucose concentration more frequently or even continuously.

The progress of the Blood Glucose Monitoring Devices BGMD is more oriented to non-invasive methods, in order to avoid blood drawing, the insertion of needles, or any kind of sensor under the skin. The main aim is to measure blood glucose level only by placing the sensor on the human target area. In view of the fact that minimally invasive devices, continuously monitoring blood glucose, are already available. However, these devices use subcutaneous sensors, and they are not really comfortable for patients. Moreover, they require continuous calibration and have to be removed and placed surgically by a physician.

The most popular blood glucose monitors almost exclusively adopt enzymatic analysis methods, based on glucose oxidase and glucose dehydrogenase, owing to their better sensitivity, reproducibility, and easy maintenance, as well as their affordable cost [51]. The enzymatic reaction products are detected photometrically or electrochemically in glucose test strips and glucometers. In the reflectometric method, the intensity of the color of the chromogen, generated by the reaction, is measured. On the other hand, the impedancemetric method measures the electrical conductivity of the blood, induced by the current generated by the redox reaction

## Impedance measurements in biomedical applications

---

itself. An example of a typical glucometer is shown in Fig. 1.4)."[1]



Fig. 1.4 Glucometer with pen blood lancet and test strip. A drop of blood, collected by pricking the finger with the lancet, is spilled on a disposable test strip and then analyzed by the device. Finally, the device displays the blood glucose level in units of mg/dL or mmol/L [1].

"A first classification of non-invasive blood glucose monitoring (NBGM) could be based on their technologies. Optical monitoring technologies involving infrared (IR), mid-infrared (MIR) spectroscopy based on light in the 2500 nm-10.000 nm spectrum and near-infrared (NIR) region of the electromagnetic spectrum (750 nm-2500 nm), are available for glucose detection. Once a tissue is illuminated, the light attenuation and its resulting spectrum, which represent its optical signature, are strongly related to physicochemical parameters such as tissue composition, changes in body temperature, blood pressure, skin hydration, concentrations of triglyceride, and albumin [52].

However, it is difficult to figure out glucose-specific information from such spectra. Especially because glucose molecules are predominantly located in the interstitial fluid, at the junction between the epidermis and dermis; rather than in the dermis, which is the target region for spectroscopy [53]. In addition, the interstitial glucose concentration is proportional to the blood concentration, albeit with a delay of 10 min [54]. NIR and MIR spectroscopy are applied on the earlobe, finger pulp forearm, lip mucosa, oral mucosa, tongue, nasal septum, cheek, and

## 1.2 Impedance measurements in diabetology

---

arm. The measurement takes approximately 1 min and allows for quasi-continuous glucose monitoring for one day without recalibration [55]. NIR diffuse reflectance measurements, performed on the finger, show a correlation with blood glucose; nevertheless, the predictions are often not sufficiently accurate to be clinically acceptable [56].

Another method based on the assessment of the glucose concentration of interstitial fluid (ISF), as abovementioned closely related to the blood glucose level, has been applied to continuous glucose monitoring using impedance measurements [57]. In particular, the measurement of normal skin impedance has been proposed to determine the volume of the ISF extracted transdermally, which is linked in turn to glucose concentration. Actually, the transdermal permeation rate of glucose molecules is inversely proportional to the skin impedance in the normal direction. Furthermore, transdermal permeation of the skin defines the volume of extracted ISF.

Impedance spectroscopy has been proposed as a possible approach for non-invasive glycemia monitoring. However, only a few studies report data about impedance related to glucose concentration, especially below the MHz band [58]. Li et al. investigate the dielectric properties of aqueous solutions with different glucose concentrations, by considering also the blood volume pulsation in a full cardiac cycle, and by measuring bioimpedance difference for NBGM [59].

Tissue dielectric constant has been employed also as an indicator of skin water content, whose changes, especially in the foot, are linked to diabetes mellitus. The dielectric constant might be a valuable technique to screen for early changes in foot skin features, that may tend to cause diabetes mellitus-related edema [60].

Another study suggests that tissue dielectric constant, used to assess skin water content, is inversely related to glycated hemoglobin, HbA1c. Changes in dermal water are related to glucose control as measured by HbA1c or fasting glucose. The HbA1c value reveals the average plasma glucose levels during the last 2 to 3 months and has been considered, for a long time, the standard for assessing blood glucose control over longer periods [61].

The electrical impedance measurement of blood has a positive correlation with blood glucose values. Impedance sensing devices, with different working electrode areas, can investigate the glucose concentrations present in human blood. Within

## **Impedance measurements in biomedical applications**

---

this framework, the impedance value increases with the rise of glucose concentration in blood, independently from the specific body area under test [62].

Finally, it is beyond doubt that despite the promising advances, we are only at the beginning of non-invasive glucose biosensor development, which combines accurate real-time glucose monitoring, with long-term stability and appreciable accuracy." [1]

"Non-invasive methods for glucose monitoring and/or less invasive are more desirable alternatives than the above-mentioned technology. One of the first attempts to apply bioimpedance measurement to non-invasive continuous glucose monitoring was carried out by the Caddiff's group in 2003 [63].

The sensor for impedance measurement had the size of a wristwatch and holed an open resonant circuit coupled to the skin and a circuit. Its clinical trials highlighted a good correlation between changes in blood glucose and sensor results. However, the main constraint was the calibration, with the patient unmoving for 60 min before the measurement.

According to these studies, Pendragon Medical Ltd of Switzerland, developed a commercial wrist-watch: Pendra, Fig. 1.5 B [64]. The back of the watch had a tape that allowed the contact with the skin to perform impedance measurements through its open resonant circuit at 1 Hz-200 MHz. Unfortunately, once launched on the market, more than 30% of the patients could not use the device, since their skin types and basic skin impedance were unsuitable. Overall, the measurements also showed poor correlation with conventional glucose meters and, therefore, the product was withdrawn from the market [65].

Another attempt, to use a "smart watch" as a non-invasive glucose monitor, was the biographer GlucoWatch®, Fig. 1.5 A, (Cygnus Inc.) [66]. The device extracts glucose concentrations through intact skin in interstitial fluid (ISF), where it is measured by an amperometric biosensor by reverse iontophoresis (RI). Clinical trials of the GlucoWatch showed adequate precision for home blood-glucose monitoring. However, the device was not designed to replace a regular blood glucose meter. Eventually, GlucoWatch was retracted from the market because of reported skin irritation caused by the RI process, the long necessary warm-up time (2-3 h), and the need for calibration using standard blood glucose strips [67]." [1]

"Considering the last failures, researchers need to focus on the production of reliable, efficient, and non-invasive glucose monitoring platforms. A proposal for a



### 1.3 Impedance measurements in dentistry

---

new device that exploits bioimpedance to assess insulin absorption is shown in the next chapters." [1]

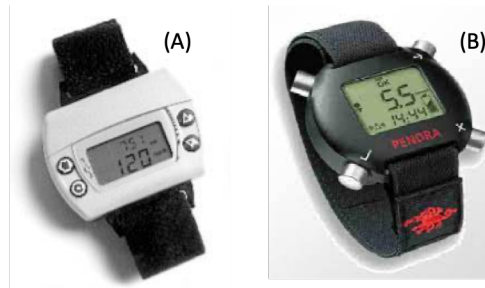


Fig. 1.5 Glucowatch (A) and Pendra (B) continuous glucose monitors [1].

### 1.3 Impedance measurements in dentistry

"Oral diseases afflict nearly 3.5 billion people worldwide, according to the Global Burden of Disease Study 2017 [68]. Among them, untreated caries in permanent teeth affect 2.4 billion people, of which more than 530 million children suffer from caries of primary teeth, representing, thus, one of the most prevalent health conditions worldwide." [9]

"Oral diseases affect people throughout their lifetime, having a significant impact on the quality of life, causing pain, anxiety, stress, functional constraints, social handicap, and disfigurement by tooth loss." [9]

World Health Organization estimates that between 60% and 90% of school-age children worldwide have dental caries, while periodontal disease affects about 14% of middle-aged adults, with varying incidence between different regions.

In Italy, the carious disease affects 43% of children up to 12 years of age, and the incidence increases with increasing age, reaching 88% of individuals between the ages of 19 and 25 that have carious lesions. Therefore, untreated caries of permanent teeth is the most common pathology at a global level [69].

Treatments for oral health conditions are expensive and usually are not included in Universal Health Coverage (UHC). The financial burden of oral diseases has been estimated as direct costs, annual global expenditure of about US\$ 387 billion, and US\$ 323 billion in indirect costs. Where indirect costs represent productivity losses

## **Impedance measurements in biomedical applications**

---

due to the above-mentioned implications of oral diseases.

Among them, edentulism has the highest global economic burden impact, followed by caries of both permanent and deciduous teeth. In particular, Italy is the fifth country in the world with the highest direct annual expenditure related to the leading five oral diseases with 19.2 billion US\$.

However, the costs of oral diseases and other non-communicable diseases could be decreased through public health interventions, taking advantage of prevention and limiting common risk factors. Unfortunately, most middle-income and low countries do not have adequate services available to prevent and treat oral health conditions [70].

One of the abovementioned leading five oral diseases is dental caries, also referred as 'tooth decay'; it is a multifactorial disease that destroys dental hard tissues over time, through endogenous bacteria located on the tooth's natural surface in the bacterial biofilm (dental plaque).

The oral plaque bacteria, mainly mutants streptococci and lactobacilli, which are naturally present in the oral cavity, ferment the carbohydrates and sugars contained in foods and drinks, and thus produce weak organic acids which demineralize tooth tissues.

The acids start to propagate into the enamel, the external part of the dental crown, which is predominantly mineral in content. The enamel consists of mineral calcium phosphate, arranged in a crystal structure known as hydroxyapatite ( $Ca_{10}(PO_4)_6(OH)_2$ ), which gives it a glass-like appearance. The continuous changes in pH in the oral environment, due to the accumulated plaque and daily diet, lead to constant surface changes in enamel; in particular the acid exposure lead to enamel demineralization due to the precipitation of calcium and phosphate from the tightly packed hydroxyapatite lattice. The expression 'dental caries' or 'caries' may refer to both the carious lesion (cavitated or non-cavitated) and the caries process itself [71][72].

Dental caries take place in whichever form and position on the teeth in the mouth. Hence, they "can be classified into several categories according to different parameters. They can vary from the incipient caries on the outer enamel surface, which generally are non-cavitated, to the subsurface enamel layer demineralization with pit and fissure caries, or secondary caries, to the lesions that involve a deeper part of the tooth such as enamel caries, dentinal caries, root caries." [11]

Cavitations, in either opaque or discolored enamel, appear as a result of demineralized dentine which causes the collapse of the overlying enamel.

### 1.3 Impedance measurements in dentistry

---

As a matter of fact, the cavitation size does not always reflect the degree of damage that occurred to the dentine; only minimal cavitation might be visible despite a fairly deep dentine demineralization. "However, the caries process is similar for all types of caries and teeth and it always starts with demineralization. Nevertheless, the human body has its own mechanism to repair dental caries lesions. Indeed, demineralization can be stopped and even reserved by calcium and phosphate, together with fluoride and other minerals present in human saliva. This process, named remineralization, together with demineralization occurs numerous times daily with the final outcome the cavitation or the reversal of dental caries [73–75]."[11]

Some medications, in particular for pediatric use, include added sweeteners, such as saccharose, with the purpose to reduce the bitter taste, which over time favor the erosion, carious degradation, and destruction processes [76].

Another dental treatment that increases the tooth surface roughening and softening, and thus the potential for demineralization, is tooth whitening; this latter even though not risk-free, is one of the most popular aesthetic dental procedure [77]. The application on the enamel surface of remineralizing solutions or toothpaste shows a considerable increase in mineral content. Therefore, innovative remineralization agents, such as fluoride, casein phosphopeptide–amorphous calcium phosphate, are used to restore carious lesions in conservative dentistry as novel non-invasive treatments [78].

As mentioned before, "dental caries is a multifactorial disease that can affect different parts of the teeth, including the enamel covering the crown, the cementum, a thin layer which covers the outside of the root, and the dentine, the tissue underneath both the enamel and the cementum. Dental caries is a chronic disease whose evolution is slow in most people. Its initial stages are usually asymptomatic, with symptoms starting after the carious lesion reaches the dentine [79]. However, the disease is initially reversible but can be stopped at any stage, even when part of the dentine or enamel is damaged (cavitation). Hence, it is crucial to reduce the caries development by intervening as soon as possible to avoid further tooth damage and invasive interventions." [9]

Moreover, "dental caries is a complex disease, thus, several measurement criteria have been developed to identify its presence, and like many noncommunicable diseases, caries can be prevented and controlled through a range of approaches." [9]

"The early caries detection and caries lesion management should involve the minimally-invasive approach capable of preventing disease progression and to enable

## **Impedance measurements in biomedical applications**

---

targeted and cost-effective management of dental caries in order to improve patients' compliance. Nevertheless, the assessment of the absence or presence of dental caries is strongly dependent on the selected diagnostic procedures; this greatly affects dentists' treatment decisions. Despite the considerable number of new diagnostic methods and diagnostic tools developed in the dental industry in recent years, their diagnostic accuracy is still uncertain. Indeed, the effectiveness of these diagnostic methods is ambiguous, since they generally report a high sensitivity and good reproducibility, conversely, they exhibit a low specificity, as highlighted in the review Fors et al. [80]. However, the visual examination remains the preferred choice owing to its reliability, simplicity, and adequate validity, especially for early occlusal caries detection and assessment [81, 82]. Generally, this latter is combined with bitewing radiography (BWR) [83], a method aimed at registering caries extensions into dentin in relation to the dental pulp; it is also greatly recommended to detect occlusal caries and for the diagnosis of interproximal caries [84]" [9]. Moreover, "during the clinical detection of caries, sharp dental explorers are often used on diagnosis of fissures caries, causing damage to the enamel already weakened due to the carious attack [85][86]." [10]

In order to overcome the low sensitivity and reproducibility of the visual examination, which is still considered the golden standard for caries detection, thanks to its high specificity, several standardized indices have been created. Among them, "one of the most popular is the International Caries Detection and Assessment System (ICDAS), a standardized visual detection system, with a clinical scoring system used in dental education, clinical practice, research, and epidemiology for detection and assessment of caries activity [87]". [9]

The need to reduce the potential health risk of ionizing radiations exposure and to reduce inter-subjects variability, and at the same time, increase the sensitivity and assessment of early carious lesions, leads to the use of several X-ray-free diagnostic methods.

"Among them, laser or light fluorescence are suitable methods for the quantitative assessment of early enamel lesions in visually inaccessible areas thanks to the change in the light characteristic due to the difference in fluorescence observed between healthy and demineralized enamel [88]." [10]. The amount of fluorescence radiance loss is connected to the mineral loss, due to demineralization or carious lesions, thus, it is possible to evaluate the development of the carious lesion over time, by monitoring the change in fluorescence radiance and change in surface properties of

### 1.3 Impedance measurements in dentistry

---

tooth structure.

"Other devices exploit Near-Infrared Light Transillumination (NILT); these techniques are suitable for enamel caries detection and monitoring by using different wavelengths. Nevertheless, they cannot precisely determine the depth of the lesion in dentin [89]." [10]

"The use of impedance spectroscopy techniques in the medical field is very promising also for the development of in-vivo measurements, representing a safe alternative to ionizing radiography to detect caries, therefore, suitable for young patients and pregnant women [90]. Moreover, this technique could bring the additional advantage to enable the use of portable and low-cost instrumentation [34]". [10].

"The use of impedance spectroscopy in caries detection relies on the characteristic loss of mineral in the caries process, leading to an increased porosity in the tooth structure. This increased porosity results in a higher liquid content, from the oral environment filled with ions, than healthy tissue. Electrical measurement detects this variation by decreasing the electrical resistance or impedance [91].

Moreover, impedance spectroscopy is employed to determine root canal length as well as to characterize the enamel and dentin structures, since the dentine conductivity, due to its dentinal tubules full of liquid, is appreciably higher than the enamel. In addition, impedance spectroscopy techniques have been used to investigate the effect of smear layer [92] and dentine conditioners [93, 94] on dentine impedance, also to identify micro-leakage between the tooth and filling materials difficult to detect [95],[96]. First studies to investigate the feasibility of the use of impedance spectroscopy for caries detection date back to a couple of decades ago." [9]

The review [97] tries to evaluate the accuracy of different electrical conductance devices compared to standard detection methods, in particular for the detection and diagnosis of caries in different kinds of patients (both children and adults).

The review shows that the diagnostic accuracy of used methods to assess non-cavitated coronal dental caries, for the analyzed studies, has a piece of low certain evidence, a limited number of dental surface studies, and inconsistency owing to the variability of results. The review focused in particular on a few commercially available devices: Electronic Caries Monitor (ECM) (Lode Diagnostics, Groningen, The Netherlands), CarieScan Pro (CarieScan Ltd, Dundee, Scotland), and Vanguard electronic caries detector (Massachusetts Manufacturing Corp, Cambridge, Massachusetts, USA). The latter is no more available on the market.

The first one, namely ECM in its different versions, works at a single fixed-frequency

## **Impedance measurements in biomedical applications**

---

alternating current and with a probe, which requires a conducting medium to be placed. The measurement last 5 s and it shows a score connected to the caries progression, and thus, to the degree of porosity in the tooth structure. The device requires the accurate positioning of the probe to effectively detect caries, and the contact media spread over the surface of the tooth [98]. The device sensitivity and specificity for enamel caries detection were 61% and 68% respectively. Another limit was the selection of the different cut-offs required to perform the measurement; and despite different cutoffs were used, the device is still operator dependent and uncertain as an objective measurement method for dental caries [99] [100].

On the other hand, the CarieScan Pro device tries to overcome the limit of adequate placement of the tip and the spread of a contact media over the surface of the tooth, by deploying a multiple metal fibers tip that can adapt to different surface areas of the tooth. Moreover, the device uses an alternating current impedance spectroscopy technique to detect carious lesions. The results are shown on a display and a colored light-emitting diode (LED) displays different values and colors according to the depth of the carious lesion. In particular, the measurements last between 3 s and 5 s; and the presence of caries probability in the contact site of the device is associated with the following ranges: 0-50 low probability; from 51-90 moderate probability; and from 91-100 high probability. However, for both abovementioned devices, the tooth surface should be properly isolated and dried.

The device manufacturer claims that this caries detection method is highly successful, and it can reach a sensitivity of approximately 95% and a specificity of approximately 93%. Although, the result of the study [101] would not suggest the use of CariesScan as the first method to assess dental caries, just an adding tool to the oral investigation, since the device readings over-diagnosis in some cases would lead to unnecessary dental treatment. Indeed, the sensitivity calculated in this study was only 68.8% with a device cut off at 50; and with the same cutoff, the CariesScan Pro shows a specificity of 78.7%, which was supposed to be 93% according to the manufacturer, which dropped to 45.9% when the selected cutoff was 30. Also the study [102] would not recommend the use of CarieScan Pro to detect the carious lesions in dentine or enamel of non-cavitated molars. The device had a high specificity for cutoff values over 50, but a poor sensitivity, indeed the accuracy ranged between 0.52 and 0.70. Finally, CariesScan Pro revealed a high potential, but not high performance in detecting occlusal caries. Actually, sensitivity and specificity values for enamel caries detection are weak, the same for discrimination of the dentin caries [81][103].

### **1.3 Impedance measurements in dentistry**

---

Considering the limits of modern available devices, part of this dissertation will deal with the application of impedance spectroscopy as a non-invasive technique for the detection of carious lesions and the assessment of the demineralization, the earlier stage of the carious process. In the next chapter the design and development of a non-invasive though rather effective solution to detect carious lesions, as well as the experimental design and the obtained results will be described.

# Chapter 2

## Impedance measurements in diabetology

Some of the work described in this chapter has been previously published in [1], [5], [6],[104], and [105].

### 2.1 Insulin measurement in diabetology

"Diabetes Mellitus is a chronic metabolic disorder characterized by endogenous inability to control glycaemic excursions. Injecting exogenous insulin to restore normoglycaemia is not only a life-saving treatment for type-1 diabetes mellitus patients, but also a benefit for patients with type-2 diabetes mellitus that cannot properly clear circulating blood glucose, owing to insulin resistance. Sustained periods of hyper- or hypo-glycemia, characterized by oscillations between these states, can adversely affect health status. In fact, a poor glycaemic control leads to long-term complications, including retinopathy, nephropathy, neuropathy, an increased risk of cardiovascular disease, and so, a significant increase in mortality."[1]

As amply treated in the first chapter, "for diabetic patients, a full control of blood glucose level is a challenge with a relevant clinical, social, and economic impact.

The more and more promising technology advances in blood glucose self-monitoring provide new devices, which are smaller, faster, more reliable, and easier to use, as well as with reduced blood samples. However, the demand for non-invasive



## 2.1 Insulin measurement in diabetology

analytical methods increases more and more to achieve effective glucose monitoring in diabetics. In particular, accurate real-time glucose monitoring is required in combination with long-term stability.

The Artificial Pancreas (AP, Fig. 2.1) represents a promising response to this demand; however, it presents more than a few limitations. The AP, known also as closed-loop control of blood glucose concentration (BGC), mainly consists of a glucose sensor, control algorithms, and an insulin infusion device (Insulin Pump). The glucose sensor, generally placed on the arm, is fundamental in order to monitor the variability over time of BGC, tailor insulin dosage, and measure the efficacy of therapy after administration. Continuous glucose monitoring is performed in

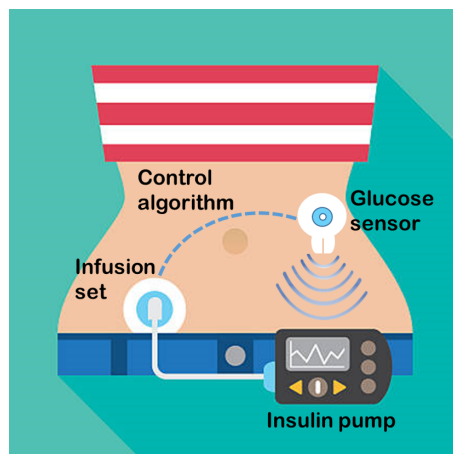


Fig. 2.1 Artificial Pancreas components schematic representation [1] .

the interstitial fluid, thus, it is associated with a time delay implicit from plasma concentration. Above all, the latency (on average 6.8 min and up to almost 10 min [106]) introduced by semi-non-invasive glucose meters, requires the AP external input to improve the glycemia regulation. The AP loop is closed automatically in case of basal insulin administration; on the other hand, in case of bolus administration, the system cannot react instantaneously to the quick BGC variation caused by food ingestion. Thus, to maintain glycaemic levels in an acceptable range, external inputs are needed, such as: Total Daily Dose of insulin (TDD), carbintake, basal/bolus ratio, basal segments, carbohydrate-to-insulin ratio (CIR), target range, insulin sensitivity factor (ISF) and, insulin duration of action. Especially, the levels of ISF and insulin duration are fixed during the initial calibration of the device (AP or insulin pump), carried out usually more than once a day. However, these parameters may significantly change depending on the kinetics of insulin absorption.

## Impedance measurements in diabetology

---

Moreover, commercial insulin pumps assess the amount of glucose in the blood in order to identify the insulin absorption curve. In this manner, suitable software packages (e.g., Bolus Wizard [107]) determine the insulin to be administered during the day. Nevertheless, the amount of glucose in the blood is not a direct indication of punctual insulin absorption. This issue is particularly evident in the case of skin alteration, such as lipo-hypertrophic nodules [108]. These nodules are associated with poor metabolic control and with considerable intra-individual glycaemic instability (Fig. 2.2). Actually, different classes of drugs, used in insulin therapies, have delayed and variable absorption if injected into lipohypertrophic nodules [109][2].

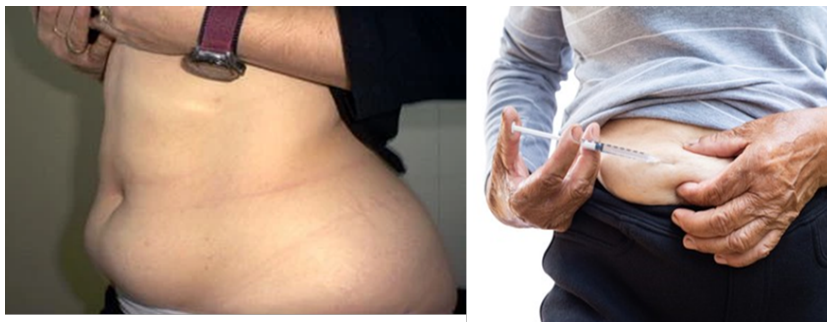


Fig. 2.2 On the left, lipohypertrophic lesions below the navel [2], on the right a typical insulin injection on the abdomen [1].

These problems affect also advanced automated diabetic therapy, where the identification of optimal doses and administration intervals are estimated on an empirical basis. Thus, a proper insulin bolus administration is not ensured by real-time monitoring of the insulin amount actually absorbed, namely bioavailable [110]. Unfortunately, to date, the main methods for assessing insulin bioavailability, i.e. the fraction (%) of administered drug that reaches the systemic circulation, are invasive or have high latency [111].

Therefore, a non-invasive method turns out to be extremely useful for monitoring the disappearance of insulin from the administration site. Furthermore, the possibility to estimate the insulin disappearance curve could provide a sound basis for the analysis of personalized therapies in different conditions of use, and could improve the effectiveness of the bolus wizard for diabetic patients as well."[1]

### 2.1.1 Basic Idea

"Impedance spectroscopy might be considered as a potential method for monitoring the progressive disappearance of a drug, subcutaneously administered, in order to obtain an indicator for the individual absorption rate.

According to the well-known concept of bioimpedance [112, 113], a tissue is considered as an electrolytic solution containing a certain number of cells. A solution is a homogeneous mixture of two or more substances. An electrolyte solution is a solution that generally contains ions, atoms or molecules, and it is electrically conductive. The substances that are dissolved are called solutes. The solute amount in a solution is evaluated by solution impedance measurement. In the same way, the insulin amount in the biological tissue is assessed by the caused impedance variation. Based on these principles, a measurement method for measuring insulin bioavailability exploits the following basic ideas [114]:

- The insulin bioavailability is a physical quantity that can be measured indirectly. Indeed, it is assessed starting from the administration volume of insulin disappearance in the biological tissue over time;
- Impedance spectroscopy is a non-invasive measurement and the disappearance of a certain insulin amount (ml) generates an equivalent impedance change, measured in the administration volume. The impedance phase is not considered in the measurement due to its low linearity and monotonicity. Therefore, the result is expressed only by impedance magnitude.
- The relationship between impedance variation and insulin decrease can be properly modeled by a linear relationship [115][104];
- A linear model for each subject is determined for every specific condition (personalized medicine) during each administration. Thus, both inter-individual and intra-individual reproducibility of the bioavailability measures is guaranteed and improved;
- The personalized linear model is characterized metrologically in order to assess the resolution, the reproducibility, and the sensibility of the insulin amount evaluation;

## Impedance measurements in diabetology

- Electrochemical cell studies and an experimental campaign on eggplants were carried out in [115], by demonstrating the impedance magnitude variability as a function of the insulin amount variation (ml) in a solution.

The purpose of the measurement method presented below is to discriminate the electrical effects of the insulin administered in the subcutaneous tissue."[1]

### 2.1.2 Measurement method

"The method for measuring the amount of insulin actually conveyed under the skin is illustrated in Fig. 2.3. It is based on the following main phases."

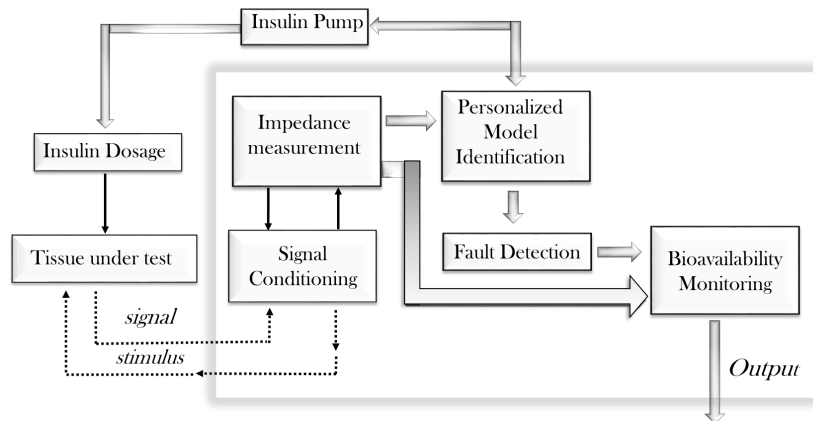


Fig. 2.3 Schematic representation of insulin measurement method phases [1].

"Firstly, the impedance measurement is measured by sending a sinusoidal current stimulus, with a specific amplitude and frequency, to the tissue under test, where the insulin is injected. Then, throughout the analog signal conditioning, the corresponding voltage drop, through the voltage meter, is assessed. The insulin is injected at known steps of a known amount by an insulin pump or an insulin pen, used as a reference for the calibration. Thus, the corresponding impedance variation, measured step by step, allows to perform a personalized model identification (insulin appearance model). During the insulin administration, the personalized individual model parameters are assessed during the off-line metrological characterization. Then a fault detection technique is applied to check if the personalized individual model parameters are within the uncertainty limits range. Thus, the insulin absorbed by the

tissue is measured, through an assessment of the impedance variation according to an insulin disappearance model (bioavailability monitoring)."[1]

## 2.2 Insulin Meter

"A device, namely Insulin Meter, based on an on-chip transducer, for real-time non-invasive monitoring of insulin absorption is presented in this chapter. The instrument, prototyped by using all off-the-shelf components, analyzes the electrical bioimpedance in the frequency domain and its variations over time. Once insulin has been injected into the tissue under test by the insulin pump in known doses, the transducer measures step by step the corresponding impedance variation. Thus, the insulin meter carries out a personalized model identification. The personalized model of insulin appearance is specific for each subject. It is identified and validated during each insulin administration. Thus, inter-and-intra individual reproducibility is enhanced. Then, the insulin bioavailability over time is assessed indirectly by monitoring its time-dependent disappearance from the administration volume of biological tissue. The concept, the whole system design, along with the hardware and software realization are described hereafter. Finally, the instrument calibration is reported." [1]

## 2.3 Design

"The *Insulin Meter*, an on-chip instrument, monitors the amount of drug actually penetrated into the tissue, after a transdermal treatment, by assessing the difference between the impedance magnitude before and after the administration. Instead of assessing the appearance of the drug, the *Insulin Meter* is able to measure the disappearance of the drug from the injection site. Thus, the drug bioavailability is assessed indirectly. Below, the *Architecture* and the *Operation* of the instrument are reported"[1]

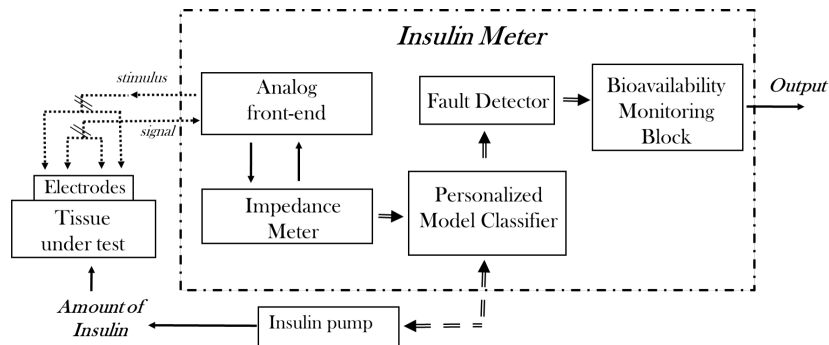


Fig. 2.4 Architecture of the Insulin Meter [3].

### 2.3.1 Architecture

"The architecture of the Insulin Meter is highlighted in Fig. 2.4. Four pre-gelled *Electrodes*, two amperometric and two voltmetric, are applied on a specific body area, the *Tissue Under Test*, where the insulin is administrated. Actually, the *Tissue Under Test* can be whatever biological tissue, ranging from eggplants to pig skin, and human skin. A given sinusoidal current is imposed, and a corresponding voltage drop is measured by the *Impedance Meter* through the *Analog front-end*.

When the *Insulin Pump* administers the insulin amount at fixed steps, the transducer measures the corresponding impedance variation. Subsequently, starting from these measurements, the Insulin Meter identifies a personalized model experimentally through the *Personalized Model Classifier*.

The parameters of the identified model are checked by the *Fault Detector* to verify if they fall within the uncertainty limits fixed during the off-line metrological characterization. If so, the *Bioavailability Monitoring block* assesses the insulin amount systemically absorbed (and, therefore, disappeared from the tissue under test), by measuring the impedance variation." [1]

### 2.3.2 Operation

"The Insulin Meter operates according to the following steps:

- *Tissue preparation*: generally, the tissue must be appropriately treated before the measurement. In particular, the surface of the stratum corneum has to be

removed in order to increase the stability of electrode-skin contact. Moreover, the thinning of the stratum corneum is useful to decrease the negative impact of its impedance on the measurement sensitivity. The corneum abrasion can be carried out by an acetone gauze, an abrasive film, or an adhesive tape. Nevertheless, the residual stratum corneum still represents a relevant uncertainty source. Furthermore, the sebum is removed to reduce the measurement uncertainty related to the pH of the skin;

- *Electrodes Application*: the four-electrodes configuration is used to soften the impact of the electrolytic gel on the impedance drift. Adhesive pre-gelled electrodes FIAB PG500 (Vecchio, Florence, Italy) [116] are employed to reduce the movement artifacts and to improve the electrodes-skin contact. Moreover, a personalized 3-D printed support in Thermoplastic polyurethane (TPU) is used to stabilize the measurement setup and to improve the placement on the anatomical site;
- *Reproducibility Enhancement*: the average of the impedance magnitude acquired at each measurement cycle is used to reduce the single measurement uncertainty. As concern the inter-individual reproducibility, each individual exhibits a different behaviour our or of the tissue impedance, due especially to the variability of the stratum corneum thickness and hydration. The reproducibility is improved by normalizing the impedance average to its pre-administration value;
- *Model Construction*: the impedance is measured at the frequency of 1 kHz after each step of insulin administration. The calibration model is determined from the injection process and it associates the impedance variation to the insulin amount. The relationship between the impedance variation and the drug amount is well modeled by a linear relationship (Fig. 2.5). During the injection phase, this model is identified both for each subject and for each particular physiological condition of the same subject. Therefore, the intra-subjective and inter-subjective reproducibility is improved;
- *Fault Detection*: a compatibility check is implemented between the linear model identified and the tolerance range resulting from the initial metrological characterization of the Insulin Meter;

## Impedance measurements in diabetology

---

- *Bioavailability Monitoring*: the impedance variations are measured over time to assess the corresponding insulin absorption (insulin disappearance) through the linear model built in the injection phase (insulin appearance). In the following subsection, a specific focus on bioavailability measurement is presented." [1]

### 2.3.3 Bioavailability monitoring

"Increasing gradually the amount of drug while measuring impedance variations allows to identifying a custom relationship for the specific tissue under test. An example of a typical model built after the insulin injection is presented below (Fig. 2.5). In the same figure, the relationship between the amount of drug, injected by the insulin pump in known steps, and the percentage impedance variation is highlighted by the linear regression line. This model represents the insulin appearance model. It can be employed for monitoring the insulin disappearance, due to the absorption by the human body, and thus the bioavailability." [1]

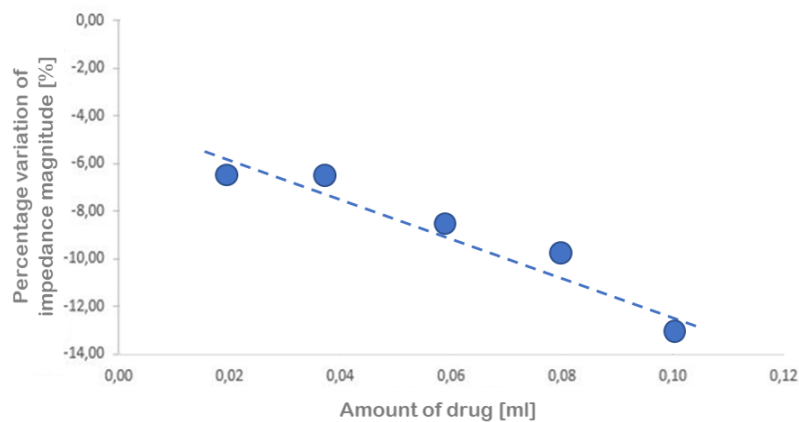


Fig. 2.5 Model of insulin appearance: the linear relationship between the percentage impedance variation and the amount of insulin [1].



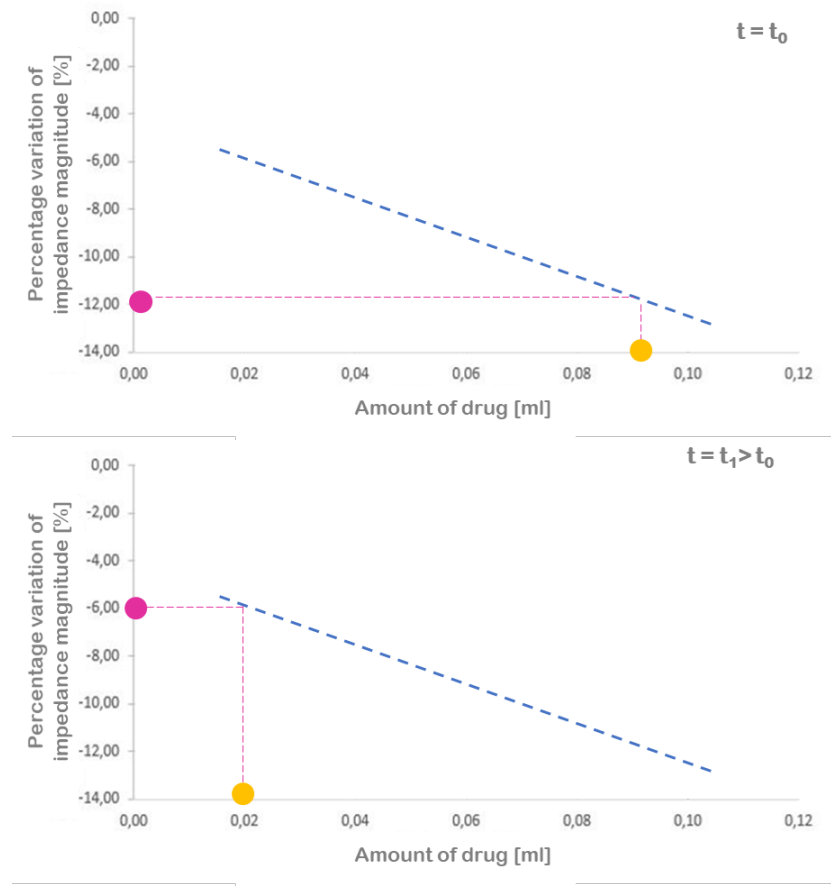


Fig. 2.6 Insulin appearance personalized model used to assess the disappearance of insulin [1].

"The appearance model allows to estimate around 0,09 ml of a drug still in situ, and, therefore, not absorbed (yellow dot). An inverse model of insulin appearance is used in the absorption (disappearance) phase. At the instant  $t_1$  (bottom of Fig. 2.6), an impedance measurement detects a percentage variation of -6 % compared to the impedance value before injection. In this case, 0,02 ml of a drug is estimated to be still in situ. Consequently, almost all the insulin was absorbed." [1]

## 2.4 Realization

"Off-the-shelf components are exploited for the Insulin Meter realization. Therefore, the cost of procurement and development results is very low, and also maintenance

## Impedance measurements in diabetology

---

is almost cheap. The instrument can be connected to pre-gelled electrodes in a framework of in-vivo clinical trials. Power is supplied from a laptop via a USB cable, or via its own battery, during in-vivo working. Fig. 2.7 shows the prototype board of the insulin meter with motherboard provided as evaluation kit [117] from Analog Device." [1]

### 2.4.1 Hardware, firmware, and software

**Hardware** "The instrument, here presented, consists of a black rigid outer case, specifically designed and 3D-printed in order to guarantee the insulation of all the components. The case contains a motherboard, the Eval-ADuCM350 EBZ Vers. A, equipped with an analog front-end and a processor ARM Cortex-M3 at 16 MHz, specifically designed for high-precision data acquisition. The motherboard imposes the sinusoidal input signal with its 16-bit DAC, and it is able to convert the sensed current signal into a voltage signal by means of its 16-bit to 160 kSa/s ADC. The motherboard performs a Discrete Fourier Transform (DFT) on 2048 points, which is used for ac impedance measurements. It presents the real and imaginary parts of a complex result [112, 113].

The motherboard (Fig.2.7) presents a slot for the daughterboard of signal conditioning. The daughterboard "4-Wire Bio Impedance Configuration 4W-BIO3Z" of Fig. 2.7 (A) can perform 4-wire measurements. The Insulin Meter provides a collection of power modes and features; The three main supply options include: a USB cable, battery, and 3.3 V via external transformer and wall socket. The battery solution, shown in Fig. 2.7 (B), might be adopted when the device is used as an actual portable system, potentially applicable in several e-health scenarios, and for home-care of chronic patients, as well as for continuous daily monitoring (i.e., Holter monitoring). At this aim, the user can verify, at any time, the measurement process by means of an 8-digit ADuCM350-GPIO-REV-B LCD of the Analog Device, shown in Fig.2.7 (D), and a selector.

Finally, the board is connected to the biological tissue under test through four electrodes. One of the key challenges in bioimpedance measurement systems is the electrode placement. The design of a bioimpedance device cannot avoid considering and reducing the adverse effects connected to electrode polarization, the high contact impedance, the noise of the interface, and the artifacts due to movements along with

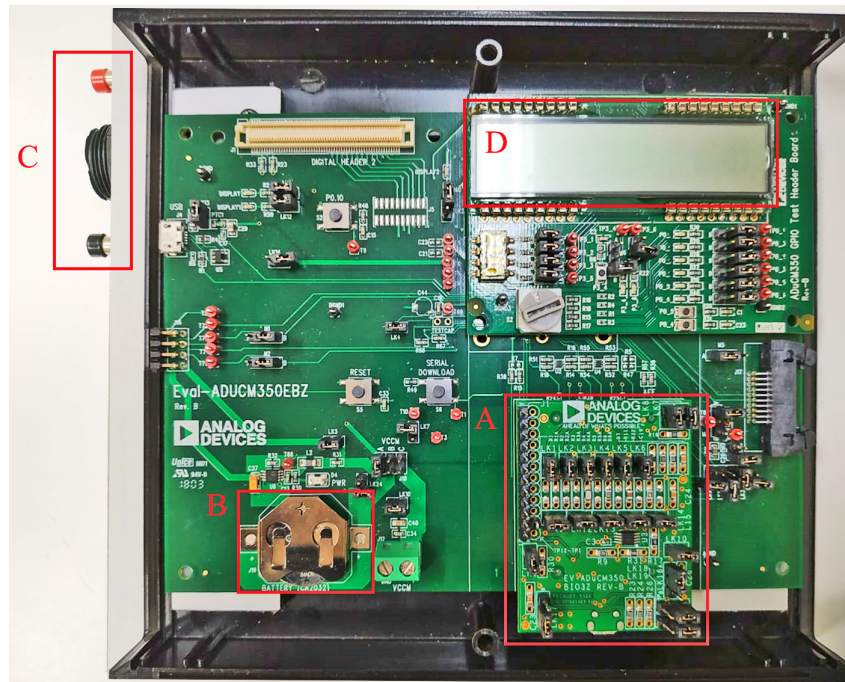


Fig. 2.7 Insulin Meter Prototype board: motherboard ADuCM350 Vers.A with (A) daughter-board BIO3Z for 4-wire bioimpedance measurement, (B) battery, (C) ON and Reset buttons, and (D) display [3].

contact problems. The electrodes represent the electrochemical interface needed to connect the biological medium with the measuring equipment, both for voltage detection and the injection of current. For bioimpedance measurements on the human body, described in this work, the electrodes FIAB PG500 are used, where the electrode-skin contact consists of a metal flexible electrode, and adhesive and conductive solid gel Ag-AgCl electrode, with an electrolyte based on  $\text{Cl}^-$ .

In this case, a quadruple electrodes configuration is adopted, where two stimulation electrodes inject the current, while two detection electrodes acquire the associated voltage drop produced by the current circulation. When the biological medium is the human body, strict international safety standards must be respected in order to avoid any possible hazard or harmful effect. In particular, the standard IEC 60601-1 [118] for the safety of electromedical equipment with the patient's active part indicates the limits of leakage currents under normal and faulty conditions. The injected current must be monitored to avoid exceeding the established limits, which are divided into two main ranges, depending on whether the stimulus frequency  $f_e$  is

## Impedance measurements in diabetology

lower or higher than 1 kHz. When the frequency is lower than 1 kHz, the maximum RMS current allowed by the standard is 10  $\mu\text{A}$ .

$$f \leq 1 \text{ kHz}, \quad I_{MAX} = 10 \mu\text{A} \quad (2.1)$$

$$f > 1 \text{ kHz}, \quad I_{MAX} = \frac{f_e}{1000\text{Hz}} * 10 \mu\text{A} \quad (2.2)$$

The insulin meter remains always below the thresholds imposed by the standard due to additional suitable resistors and capacitors located on the daughterboard in series with the unknown impedance, as shown in Fig. 2.8 in red. Indeed, the series of three resistors, of 3 k $\Omega$  equivalent value, keeps the current peak below 8  $\mu\text{A}$ ." [1]

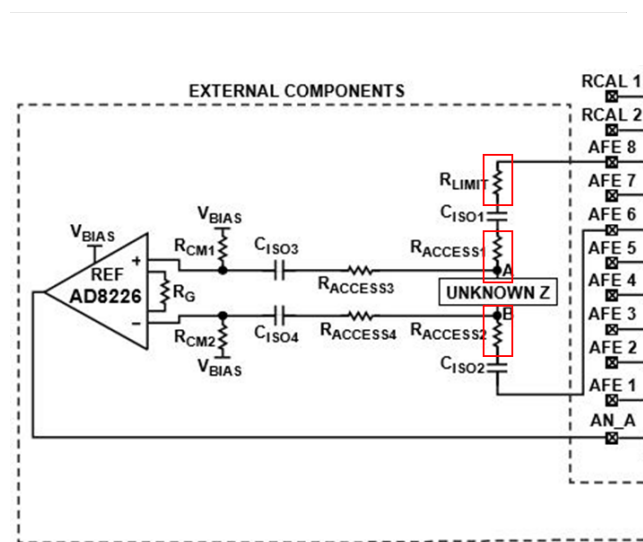


Fig. 2.8 Daughterboard schematic, in red the three resistors in series that limit the current (RCAL<sub>i</sub>, input for the calibration resistor, AN<sub>A</sub>, the auxiliary channels, and AFE<sub>i</sub>, inputs for the analog front-end) [4].

**Firmware and software** "Despite the Analog Device provides libraries for basic operation exploiting the BIO3Z board, such as 4-wires impedance measurements, a new firmware is to be developed for the transducer. A set of ten different programs is created to make the measurement faster and more user-friendly. The analog front-end is initialized only at the measurement start, allowing so to increase the throughput. Whereas, the data transmission is postponed at the measurement, because all the data are saved in the internal flash memory. In doing so, the acquisition time is reduced to 34%. Up to 7500 16-byte measurements can be saved on the transducer memory spaces of 120 kB. The collected data can be downloaded by connecting

## 2.4 Realization

the instrument to the PC via the COM port with the UART management protocol. During the debugging, to start or stop a measurement by hand, two easily-accessible ON and Reset buttons are available. Meanwhile, the display allows the user to view the current program and the current measurement number program (Fig. 2.7 D).

When the Insulin Meter is connected to the PC via the COM port, a user-friendly interface is available. The Insulin Meter is configured by means of the user interface illustrated in Fig. 2.9, developed by using different user controls (label, textbox, lists, combo box, etc.). The user can define the information on the measurement session to be performed. In particular, the user can collect the personal data of the patients enrolled in the study, such as age, sex, ethnicity, skin phototype, as well as environment and experimental settings (e.g., room temperature and humidity, the used drug, and the injection site). The interface allows to set the working frequency and amplitude and the number of measurements. Moreover, the data received by the device are properly processed and displayed. Finally, the database of collected data is available for further processing, research, visualization, and plotting." [1]

Time	Freq. (kHz)	R Ca Real	R Ca Im	LoadReal	LoadIm	Imp. Phase	Imp. Mag
08:59:08	1	90	291	-9199	-29547	-0,108534984589491	329,384240579941
08:59:09	1	90	291	-9199	-29547	-0,108534984589491	329,384240579941
08:59:11	1	90	291	-9199	-29547	-0,108534984589491	329,384240579941
08:59:12	1	90	291	-9199	-29547	-0,108534984589491	329,384240579941
08:59:14	1	90	291	-9199	-29547	-0,108534984589491	329,384240579941

Time	Freq. (kHz)	R Ca Real	R Ca Im	LoadReal	LoadIm	Imp. Phase	Imp. Mag
08:57:40	0.1	90	291	-9199	-29547	-0,107460380781674	326,123010574199
08:57:41	0.15	90	291	-9199	-29547	-0,107460380781674	326,123010574199
08:57:41	0.23	90	291	-9199	-29547	-0,107460380781674	326,123010574199
08:57:42	0.35	90	291	-9199	-29547	-0,107460380781674	326,123010574199
08:57:42	0.52	90	291	-9199	-29547	-0,107460380781674	326,123010574199

Fig. 2.9 Insulin Meter user interface [1] .

### 2.4.2 Calibration

"The primary goal of this section is to highlight the metrological characterization of the Insulin Meter, on reference passive electronic components.

The following subsections outline the procedures for calibration.

It is important to have reliable and highly accurate measurements. Therefore, it is fundamental that instruments used within any measuring system have to be calibrated. Thus, a key measurement concept is calibration, which is the comparison of an instrument or device against a more accurate instrument, certified reference materials, or other reference condition, to determine the metrological performance characteristics of an instrument. Calibration establishes the reliability of the instrument, besides it ensures that readings from the instrument are consistent with other measurements, and so, it allows to determine the accuracy of the instrument readings [119]."[1]

#### *Experimental setup*

"In the laboratory test, the Insulin Meter was compared directly with a more accurate instrument, the Agilent 4263B LCR Meter, used as reference. This latter is specifically designed for both component evaluation and fundamental impedance testing. Meanwhile, a Decade Resistor 1433-M and a Standard Capacitor Type 509-Fm, both of General Radio, realized an equivalent parallel circuit between a capacitor [0.5 nF] and a variable resistor [42-2500  $\Omega$ ]." [1]

#### *Calibration*

"The measurements were carried out in chambers where environment factors were controlled; in particular, the temperature was 23 °C and the relative humidity 50%. The impedance magnitude was measured for a set of frequency points chosen in the 100 Hz – 20 kHz frequency range. In particular, 32 measurements were carried out, for each resistor value, at the frequency of [100, 120, 10000, 10000, 20000 ]Hz, by generating for each point a sinusoidal waveform of amplitude 100 mV. The mean and the standard deviation of the impedance magnitude of the RC loop were assessed, at each selected resistor value. The resistor value varied in a linear sequential manner within [42, 2500] $\Omega$ ." [1]

#### *Results*

"Considering the nominal values calculated for the RC loop at 1 kHz, both the instruments, the Agilent 4263B LCR Meter and the Insulin Meter, present an impedance variation trend compatible with the nominal one. Fig.2.10 shows the impedance

## 2.5 Metrological characterization of the Insulin Meter

variation measured at 1 kHz by the instruments, at varying the resistor value of the RC loop." [1]

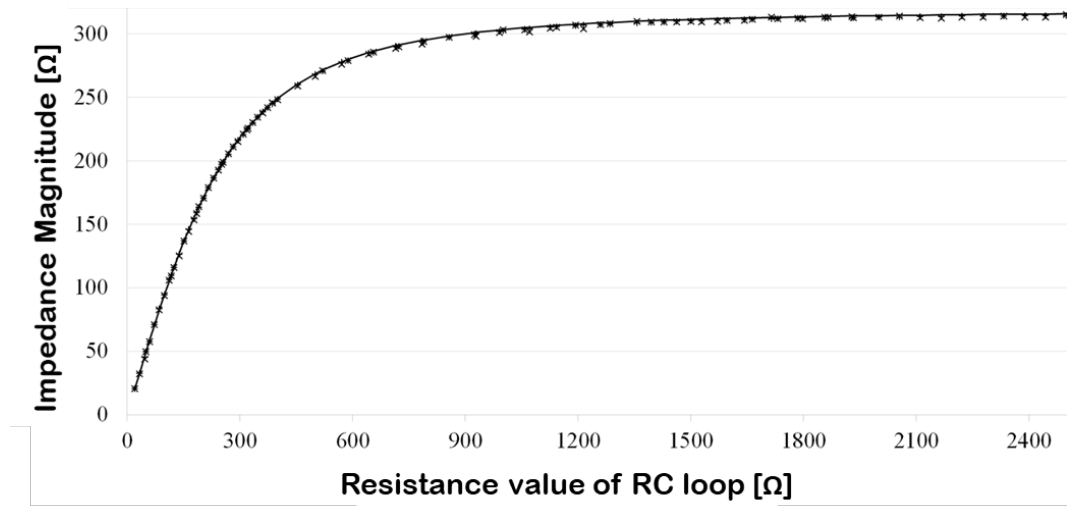


Fig. 2.10 Impedance magnitude at 1 kHz at varying the resistance value of the RC loop: theoretical trend (continuous line), Insulin Meter (×), and reference LCR Meter (+) [1].

## 2.5 Metrological characterization of the Insulin Meter

The Insulin Meter was characterized metrologically, firstly (i) in the laboratory, by means of a direct comparison against reference impedance, as shown in the previous section; then, (ii) in-vitro, on eggplants, and, finally, (iii) ex-vivo, on pigs, by means of insulin injection. The following sections intend to focus attention on the in-vitro and ex-vivo tests.

### 2.5.1 In-vitro metrological characterization of the Insulin Meter

"Experimentation is the best-known way to test the veracity of scientific theories and to provide clues to causal inference. The first experimental tests of the Insulin Meter, detailed below, are conducted in vitro.

In-vitro tests are procedures or experiments, performed outside a living organism, in a controlled environment. These conditions allow to carry out more detailed

## **Impedance measurements in diabetology**

---

analyses and to examine biological effects in a larger number of critical situations, than in animal or human trials. Therefore, also in this case, the experimental in-vitro campaign is conducted on eggplants, already shown as able to satisfyingly mimic the human tissues' behaviour our or [120, 121].

In the following subsections, the tests for drift, sensitivity, nonlinearity, repeatability, reproducibility, and accuracy are illustrated. The results of each metrological characteristic are compared for both a generic and a personalized model.

Specifically, the generic model is identified offline during the metrological qualification tests on all the samples, as it is common in traditional medicine. On the other hand, the personalized model is identified online on the specific subject tissue, in definite measurement conditions. The generic model highlights the performance of the Insulin Meter applicable to every generic individual, but without taking into account the specific condition of the subject. Conversely, the personalized model highlights the performance specific to a single subject and is still valid in every use condition. In addition, two different configurations of the Insulin Meter, namely two and four-wire measurements, are tested and compared. Finally, for these two setup configurations, the differences in the parameters of greatest interest are pointed out."[1]

### **Experimental setup**

"In the in-vitro tests, the impedance intrinsic uncertainty, arising from water evaporation during the measurements, is mitigated by peeling and drying the eggplants. In particular, they are dried for 2 h, in a controlled environment, at a temperature of 23° C, and a relative humidity of 50%. Each eggplant is cut in a rectangular block of 10 cm × 4 cm × 4 cm (Fig. 2.11). Measurements were performed on a total of 29 eggplants employing two different setups.



## 2.5 Metrological characterization of the Insulin Meter

---



Fig. 2.11 Example of insulin injection on eggplant.

Two different setups are used: in particular, on 9 eggplants, the electrodes are placed with an inter-electrode distance of 12 mm; on the remaining 20 eggplants, the inter-electrode distance is 5 mm. Therefore, for the sake of clarity, the two different setups (12 mm and 5 mm) will be discussed separately.

- *12-mm setup*: Four FIAB PG500 gel electrodes are placed on the prepared eggplants. The electrodes of 14 mm  $\times$  36 mm are obtained by cutting lengthwise in half the full electrode of 28 mm  $\times$  36 mm. A preliminary impedance measurement is carried out for each sample, by imposing a sinusoidal voltage amplitude of 20 mV, at a frequency of 1 kHz. This measurement, performed before the infiltration, allows to improve inter-species reproducibility. Then, the total amount of insulin (0.25 ml) is administered 8 mm below the surface, in 5 consecutive steps of 0.05 ml. The insulin, Lilly's Humalog, of fast type, consists of a solution with 100 UI/ml, where each UI indicates 0.0347 mg of human insulin. The insulin is administered using a commercial pen and a dedicated needle (PIC Insumed 31 G syringe) with 31G  $\times$  8 mm. G stands for Gauge, an internationally-used scale for sizing the thickness of a needle; in particular, the needle of 31 G has a diameter of 0.41 mm.
- *5-mm setup*: This setup provides different inter-electrode distances, injection depth, and amount of the injected insulin. The main purpose is to improve the instrument sensitivity, to emulate the actual condition of use, and to enhance as much as possible the benefit in diagnostic-therapeutic applications. Thus, two

## Impedance measurements in diabetology

---

electrodes FIAB PG500 ( $28 \times 36$ ) are cut lengthwise to obtain four electrodes of  $7 \text{ mm} \times 36 \text{ mm}$ . The fast insulin is injected by a 100 U/ml Insulin Pen at a 4 mm depth. A total amount of 10 IU dosage (i.e.,  $100 \mu\text{l}$  of solution) is injected in each single experiment, by five consecutive injections of 2 IU (i.e.,  $20 \mu\text{l}$  of insulin solution). The selected administered amount, as well as the used device, are close to the insulin injection technique and doses, commonly used in diabetes treatments.

For both the setups, 5 mm and 12 mm, impedance measurements are repeated to reduce the uncertainty. The following subsections deal with the analysis of the main parameters useful for metrological characterization." [1]

### Drift

"Drift refers to continuous or incremental change in indication over time, due to changes in the metrological properties of a measuring system or reference material [119]. In this context, drift arises from the evaporation of the water contained within the eggplant, which changes the impedance; as well as from the electrodes degradation, with the consequent electrolytic gel penetration into the eggplants. In particular, this latter has a significant impact on the impedance measurement [114].

The drift impact on the measured impedance is attenuated by the four-wires configuration. In Fig. 2.12, the trends of electrolyte gel penetration are illustrated for both the two-wires and the four-wires configuration. In the two-wires configuration, the progressive penetration of the electrolyte gel induces a decrease in contact impedance within 160 min. On the other hand, the four-wires configuration significantly reduces this effect, and the drift is reduced to 2.9%." [1]

### Sensitivity

"The sensitivity is defined as the ratio between the minimum variations in the response of a measuring system and the corresponding minimum appreciable variation in the measured quantity [119]. In this case, the Insulin Meter sensitivity is assessed as the slope of the linear model for the two different setups. For the 12-mm setup, the average value is equal to  $24.7 \text{ ml}^{-1}$ , meanwhile, for the 5-mm setup the average value is  $497.3 \text{ ml}^{-1}$ . Specifically, a variation of 1 ml of insulin generates a percentage

## 2.5 Metrological characterization of the Insulin Meter

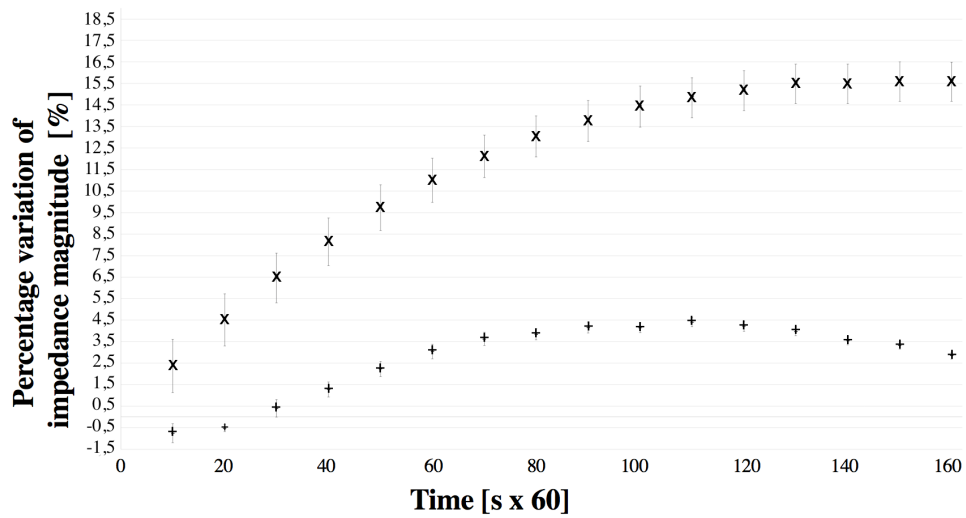


Fig. 2.12 In-vitro drift (average on 10 measurements) in four-wires (+) and in two-wires (x) configuration [1].

impedance variation of 497.3%, compared to the initial impedance measured before the injection.

The typical trend of the 5-mm setup on eggplants is shown in Fig. 2.13, in terms of the percentage change in impedance corresponding to the drug amount. While an example of a typical trend for the 12-mm setup is shown in Fig. 2.14." [1]

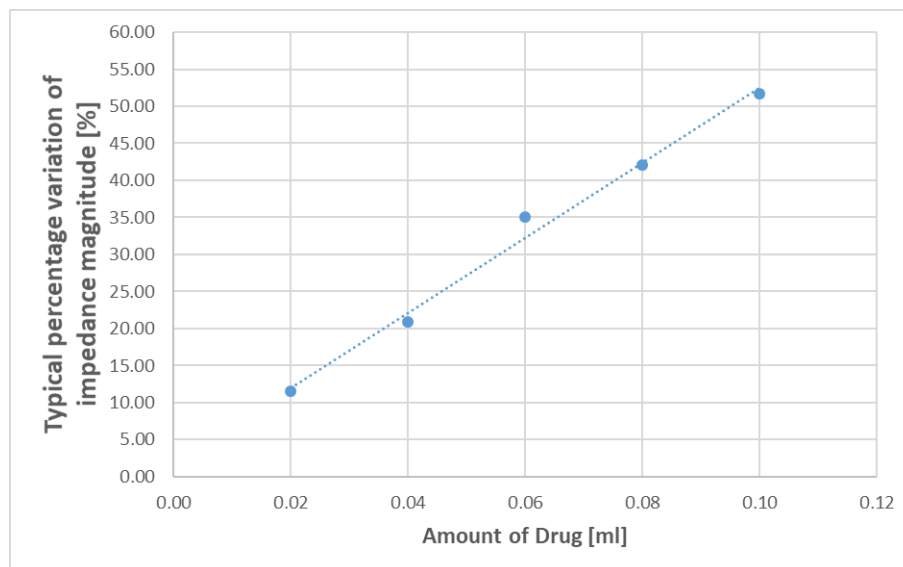


Fig. 2.13 Impedance percentage magnitude variation vs the amount of insulin for in-vitro experiments in 5-mm setup.

## Impedance measurements in diabetology

---

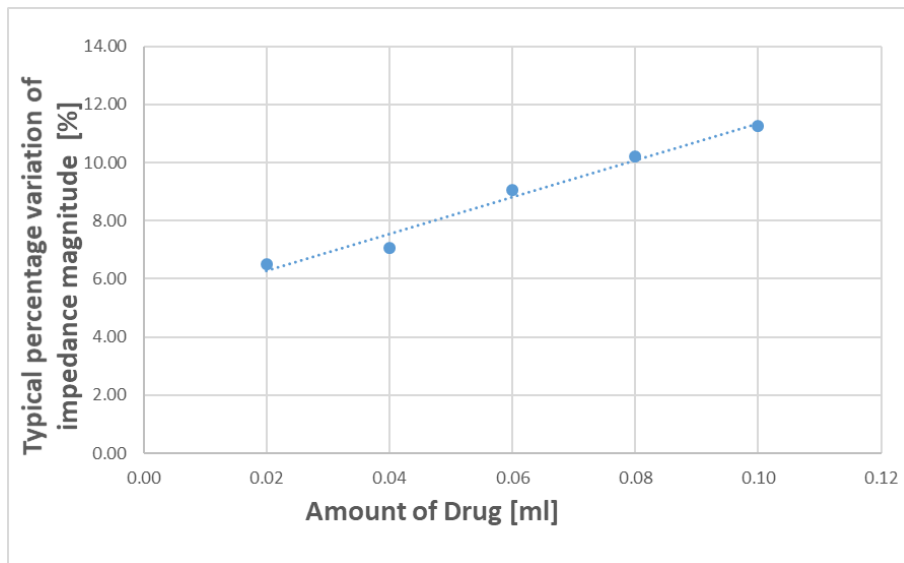


Fig. 2.14 Impedance percentage magnitude variation vs the amount of insulin for in-vitro experiments in 12-mm setup.

### Nonlinearity

"By means of one-way ANOVA, the nonlinearity is determined as the standard deviation of the residuals of the linear model. For the 5-mm setup, the typical percentage values (expressed as the average  $\pm 1-\sigma$  of the sample mean) are reported in Tab. 2.1, both for the personalized and generic model. In particular, the nonlinearity, exhibited by the personalized model, is always lower than the generic model." [1]

### Repeatability

"The repeatability condition of measurement represents a condition, out of a set of conditions that includes the same measurement procedure, same operators, same measuring system, same operating conditions, and same location, and replicate measurements on the same or similar objects over a short period of time. A condition of measurement is a repeatability condition only with respect to a specified set of repeatability conditions [119].

For both the setups, 12 mm and 5 mm, the  $1-\sigma$  repeatability is assessed as the percentage variation relative to the initial impedance value, at varying the amount

## 2.5 Metrological characterization of the Insulin Meter

Table 2.1 Nonlinearity of the Insulin Meter for the 5-mm setup

Eggplant sample	Generic %	Personalized %
# 1	9.7	4.6
# 2	5.3	5.1
# 3	4.6	4.6
# 4	5.2	1.6
# 5	9.9	9.8
# 6	1.6	1.6
# 7	3.2	1.4
# 8	4.8	3.4
# 9	6.8	4.4
# 10	6.1	5.1
# 11	3.7	2.0
# 12	3.9	2.2
# 13	4.5	3.9
# 14	5.0	4.8
# 15	2.5	2.5
# 16	4.6	3.3
# 17	2.8	2.5
# 18	11.5	9.9
# 19	4.8	2.3
# 20	9.5	6.0
<b>Mean</b>	$5.5 \pm 0.6$	$4.0 \pm 0.5$

of injected drug." [1]. The trends for the 5 mm setups are illustrated in Fig. 2.15, while the trend for the 12 mm setup is illustrated in Fig. 2.16, also, in this case, the relationship between impedance variation and insulin decrease is linear. In particular, in the 12 mm setup, an average percentage value of 0.31%, which considers the value of all the points shown in the figure is determined. Likewise, a value of 1.3% is achieved for the 5 mm setup, instead.

### Reproducibility

"Generally, the reproducibility refers to the closeness of the agreement between measurements of the same quantity carried out in different conditions [119]. In this case, for the 12-mm setup, the  $1-\sigma$  individual reproducibility of 0.1% is assessed for the personalized model; while, for the generic model, the value is 0.7%. Instead, the

## Impedance measurements in diabetology

---

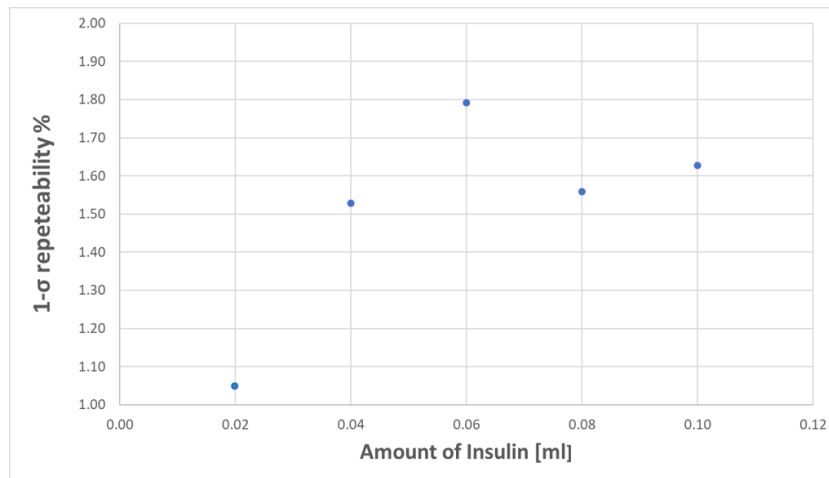


Fig. 2.15 Example of 1- $\sigma$  repeatability according to the amount of injected insulin in-vitro for the 5 mm.

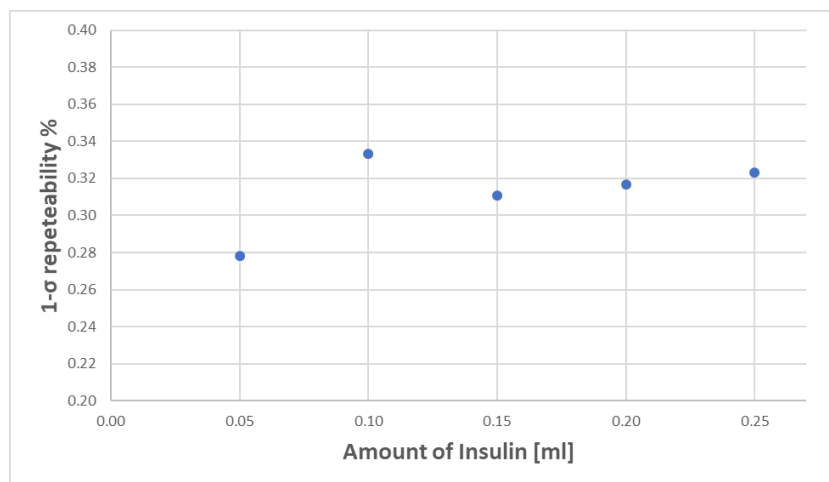


Fig. 2.16 Example of 1- $\sigma$  repeatability according to the amount of injected insulin in-vitro for the 12 mm.

optimal setup, namely 5 mm, presents a reproducibility of 2.4% for the personalized solution and 2.7% for the generic solution."[1]

### Accuracy

"Accuracy is defined as the closeness of the agreement between the measurement result and the reference value of a measurand [119]." [1]. In this case, it was assessed as the RMS of the deterministic error, that is, calculated as the distance between the measured point and the interpolation line purposely constructed. Figs. 2.17 show the

## 2.5 Metrological characterization of the Insulin Meter

accuracy results of the personalized (+) and the generic model (×), respectively, for both the 12-mm A) and 5-mm B) setups. Each point reports the accuracy variation according to the amount of injected insulin, and it is averaged on all the samples for the specific amount of insulin injected. For both setups, the personalized model a better accuracy can be accounted to the personalized models.

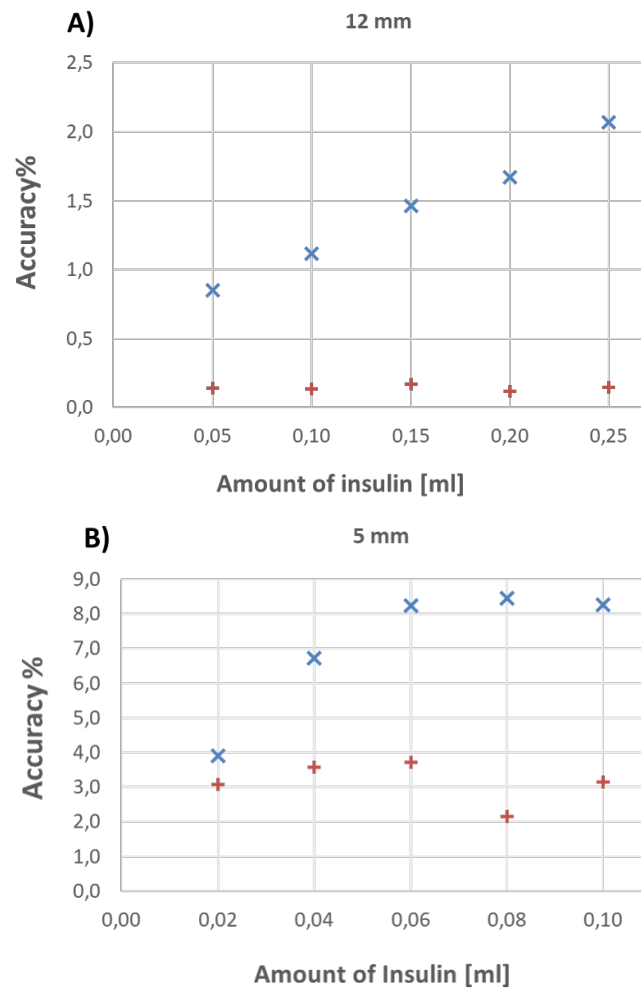


Fig. 2.17 Percentage accuracy of the personalized (+) and the generic (×) model vs the amount of insulin, in-vitro experiments for A) the 12-mm and B) the 5-mm setup.

### 2.5.2 Ex-vivo metrological characterization

"As already highlighted in the previous chapters, the similarity between pig and human tissues is confirmed by several studies [122]. In particular, the membrane permeability, as well as the epidermal thickness and the lipid part, are indicated to be very similar to the human one [123, 124]. Therefore, non-perfused abdominal muscles from several pigs are used to test the instrument, before starting the experiments on human volunteers.

Ex-vivo tests are carried out on 15 samples of pig tissues. Room temperature and relative humidity are 25° C, and 50%, respectively. All relevant guidelines and regulations are respected during the experiments. A local abattoir supplied the pig tissues samples, in compliance with the regulations on domestic animals intended for human consumption. No animals suffered or were killed as a result of the experiments.

Each pig muscle was cut to the dimensions of 7 cm x 7 cm x 4 cm. A total of 10 insulin units (IU) are injected at a depth of 4 mm via an insulin pen. The insulin administration is articulated in five steps of 2 IU corresponding to 20  $\mu$ l of insulin solution. The metrological characteristics are expressed analogously as for the eggplant experiment.

The typical relationship between the amount of insulin injected and the percentage variation of the impedance magnitude is reported in Fig. 2.18."[1]

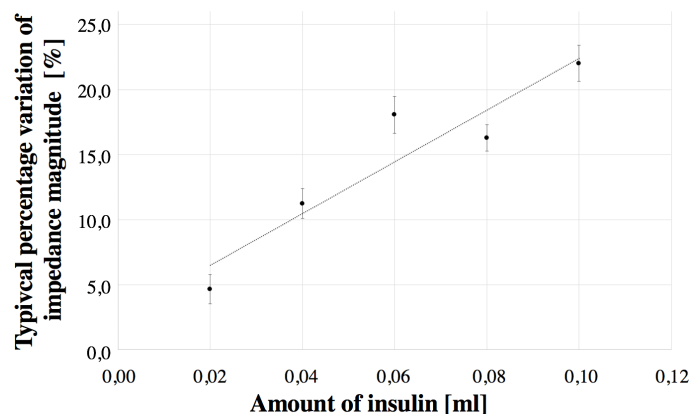


Fig. 2.18 Example of a typical impedance percentage magnitude variation according to the insulin in ex-vivo experiments [1].



## 2.5 Metrological characterization of the Insulin Meter

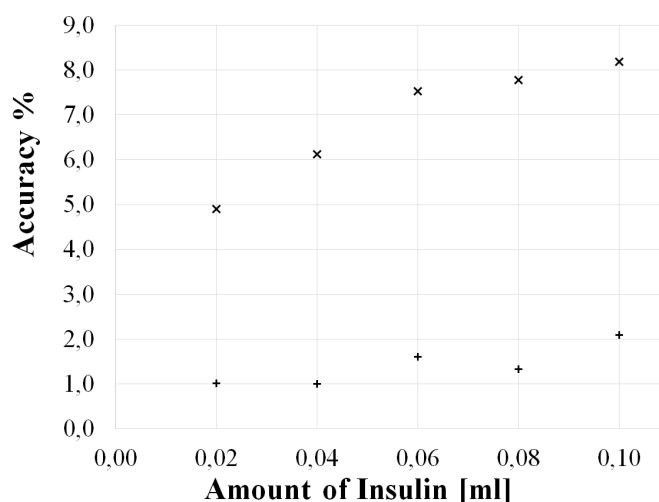


Fig. 2.19 Percentage accuracy of personalized (+) and generic (x) model vs amount of drug in ex-vivo experiments [1].

Table 2.2 Metrological parameters of pig abdominal non-perfused muscle and eggplants. [1]

	<b>Pig</b>	<b>Dried Eggplant</b>
<b>Sensitivity [ml<sup>-1</sup>]</b>	157.2	497.3
<b>nonlinearity [%]</b>	2.1	4.0
<b>1-<math>\sigma</math> repeatability [%]</b>	1.6	1.3
<b>Reproducibility [%]</b>	2.4	1.9
<b>Accuracy [%]</b>	1.4	3.2

"The sensitivity, the 1- $\sigma$  repeatability, the reproducibility, the nonlinearity, and the accuracy assessed both in the pig and in the eggplant tests are reported in Table 2.2, for the sake of the reader easiness. The same setup based on an electrode gap of 5 mm is considered for a more reliable results comparison. As reported in Figs. 2.17 B) and 2.19, the personalized model performs better than the generic model, in terms of 1- $\sigma$  repeatability 1- $\sigma$  repeatability and percentage accuracy." [1]

### 2.6 Conclusions

Impedance spectroscopy is a powerful, harmless, and painless, measurement method, considered a winning choice in many medical applications. Different biomedical applications of impedance spectroscopy were presented, however, this chapter focused on diabetology and paid particular attention to drug bioavailability assessment. In this chapter impedance spectroscopy is proposed as a non-invasive, low-cost, and effective method for the bioavailability assessment of insulin. The bioavailability, in the case of systemic drugs, is defined as the amount of an administered drug that reaches the systemic circulation. Since at present, there are no standardized methods for non-invasive measuring of the drug delivered in-vivo; the distinct non-invasiveness of impedance analysis would persuade people with diabetes to control more often, or even continuously, their glucose concentration.

An instrument, namely Insulin Meter, prototyped by using all off-the-shelf components and based on an on-chip transducer, able to analyze the electric impedance in the frequency domain and its variations over time, was used for monitoring the real-time insulin absorption. The instrument design was described, by focusing on the architecture and the operating characteristics. The calibration procedure, under controlled laboratory conditions and using reference passive electronic components, was reported. Significant results for clinical applications were outlined in terms of uncertainty, and they are compatible with the clinical targets of the Insulin Meter. The insulin bioavailability is assessed non-invasively and in real-time after administration in a specific injection site as therapy for people with diabetes. The Insulin Meter implements a personalized model identification by measuring step by step the impedance variation corresponding to the injection of a known amount of insulin. The personalized model of insulin appearance is peculiar for each subject. It is identified and validated during each insulin injection. Hence, inter- and intra-individual reproducibility is improved.

The Insulin Meter was characterized metrologically, in-vitro, on eggplants and ex-vivo, on pigs, by means of insulin injection. In all the tests, the subcutaneous injection was employed as a reference for insulin.

The experimental results show a better accuracy performance of the personalized model than a generic one. In particular, for the in-vitro experiments the highest value was reached for the 5-mm setup, where the average value is  $497.3 \text{ ml}^{-1}$ , while for the 12-mm setup, the average value is equal to  $24.7 \text{ ml}^{-1}$ . The nonlinearity assessed as the

## 2.7 Measurement method optimization by FEM modeling

---

standard deviation of the residuals of the linear model, was 4% for the personalized model of 5-mm setup. The 1- $\sigma$  repeatability, calculated as the percentage variation related to the initial impedance value, at varying the amount of injected insulin, has an average percentage value of 0.31% in the 12 mm setup, meanwhile, a value of 1.3% is achieved for the 5 mm setup. About the 1- $\sigma$  individual reproducibility, the optimal setup shows a reproducibility of 2.4% for the personalized model and 2.7% for the generic model.

These values are compatible with clinical applications; thus the device could be used to customize diabetes therapies.

## 2.7 Measurement method optimization by FEM modeling

In the previous section, a measuring method for assessing insulin absorption, based on bioimpedance spectroscopy, was validated. "The referred method was proposed to perform a customized insulin model identification, starting from a real-time evaluation of the impedance variation at the injection site. Indeed, the administration of note pharmacological doses, through an insulin pump, allows the identification of a specific personalized impedance model for each tissue's physiological condition. Then, the model was used during the absorption measurement to assess the bioavailable insulin. This method improves effectively both intra- and inter-subjects reproducibility. Nevertheless, experimental pieces of evidence showed that any pressure exerted during the procedure (e.g., injection and breathing), and the subsequent tissue deformation, affect the bioimpedance measurement, generating sensibility issues on the signal referable to the drug presence under the skin." [5]. Hence, a Finite Element Model (FEM) was implemented to model the electrical and mechanical behaviour our or of human tissues and, thus, to measure insulin transdermal delivery, manage intra-individual reproducibility uncertainty, and improve sensitivity.

The main uncertainty sources that affect the measurement method previously described are: the pressure exerted during the injection phase; and the tissue deformation due the breathing.

Subsequently, the mechanical source of electrical noise was modeled by FEM, during the application of different forces on the human abdomen, in order to improve the

## Impedance measurements in diabetology

---

accuracy of insulin absorption assessment. As well as the tissue's electrical behaviour our our was modeled. Finally, an experimental campaign was conducted to identify the condition which maximizes the stability of the setup (e.g. sample subject movement's test, the pressure exerted during the injection phase and/or breathing) and to experimentally identify a relationship between applied force, related to insulin injection, and impedance magnitude in the case of human tissue, and to validate the results obtained by simulations.

### 2.7.1 Insulin injection site

The injection site strongly affects the pharmacokinetic absorption profile of insulin. Most common injection sites include: the upper arm/deltoid, abdomen, outer thighs, and buttocks [125]. Every injection site has a different insulin absorption kinetic, due to the different vascularization and thus subcutaneous blood flow. Indeed, insulin absorption is faster in the abdomen region, and slower in the arm followed by the thighs and buttocks, as highlighted in Fig. 2.20.

Therefore, the choice of the injection site highly influences the metabolic response of different insulin preparations, and thus the choice of the optimal therapeutic regimen [126][127].

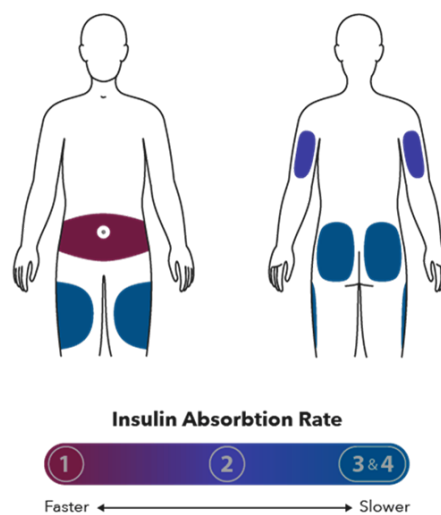


Fig. 2.20 Insulin absorption rate according to the different injection sites.

## 2.7 Measurement method optimization by FEM modeling

---

The favorite site for insulin injection is the abdomen, due to its easy access and faster insulin absorption. "Moreover, the choice of the favorite injection site is based on the following considerations: (i) the patient should rotate the injection site, in order to avoid the formation of lipodystrophic nodules; and (ii) insulin should be easily injected into the subcutaneous tissue. Insulin injection into the abdomen subcutaneous tissue is required since an intramuscular injection leads to a faster absorption than the desirable rate, higher frequencies of unexpected hypoglycemia, and glucose variability, which represent potential risks to the patient's health. On the other hand, intradermal injection provokes insulin leakage and pain [128]." [5].

In order to prevent the risks related to insulin administration therapy, is important to consider, not only the injection site but also the needle size and the exerted pressure force on the syringe, hence, the proper injection device.

The needle should be chosen according to the thickness of subcutaneous tissue, avoiding the muscles, dermis, or nerves. Different needles length are commercially available: 4 mm, 6 mm, or 8 mm. According to different studies, the needle must be pushed at 90° on the skin to decrease intramuscular risk injection [129]. In the case of a needle length of 8 mm, it is advisable to form a pinch before inserting the needle, to guarantee the right insulin absorption as shown in Fig. 2.21.

In addition, clinical knowledge of skin thickness and subcutaneous tissue is crucial for choosing the needle's appropriate length for subcutaneous injection.

However, human tissues thicknesses are not unique and may vary from subject to subject depending on age, race, sex, body mass index (BMI) as well as depending on the chosen injection site.

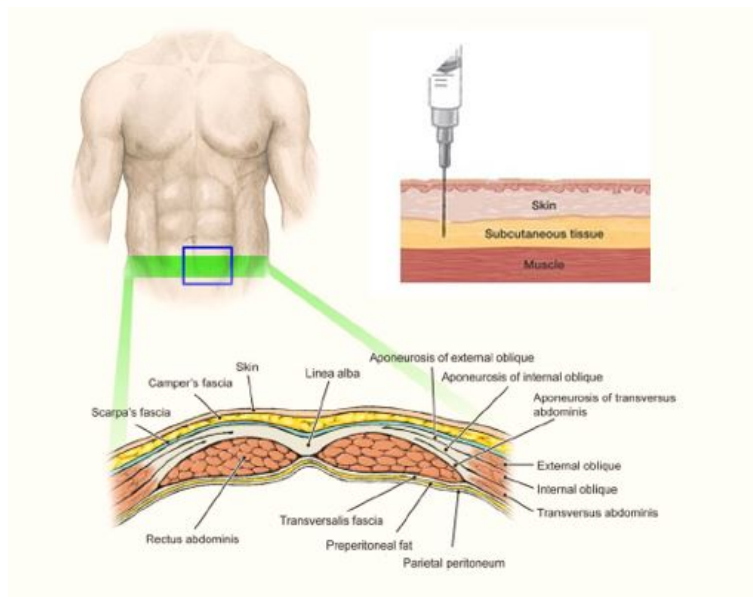


Fig. 2.21 Human abdomen stratification and insulin injection.

Healthcare providers, diabetes care, and education specialists highlight another important aspect of proper insulin injection technique: the injection force. Specifically, considering the insulin pen, the force applied at the hub pen needle and transferred by the skin to underlying tissue during the injection. This applied force has inter- and intra-subject variability; despite the clinical guidelines of the American Diabetes Association do not establish an optimal level of injection force or range of insulin injection forces, they recommend avoiding pushing the needle hub so deeply that it indents the skin because of the increased risk of an intramuscular injection. However, the force applied by the hub of an insulin pen to the skin in patients who self-administer insulin therapy was estimated [130]. About 80% of patients apply a force greater than the necessary force that guarantees a correct injection, in particular, the applied force range varies from 0.2 N to the considered limit force of 4.4 N. Proper insulin injection technique has been proven to be a crucial aspect of safe and effective insulin delivery and may improve clinical outcomes for people with diabetes. In this dissertation, the abdomen was selected as the injection site and modeled.

### 2.7.2 Tissues mechanical properties

Modeling human tissues is challenging owing to the intrinsic complexity of biological structures. To adequately model the abdomen and to characterize the biomechanical properties of tissues, their mechanical characteristics are essential. "Despite human tissues behave as viscoelastic and anisotropic materials whose characteristics change with age, gender and, location, a linear isotropic behaviour our can be adopted in a definite range of vibration analysis constant parameters [131]. The mechanical parameters used for the abdominal model are the tissues density, elastic modulus, namely Young's modulus [132], and the Poisson's ratio." [5]

"The proposed simplified abdomen model consists of 3 layers, namely skin (including epidermis and dermis), fat and muscle, whose thickness are reported in Tab. 2.3.

The average skin thickness is defined as the total epidermis and dermis thickness, it is chosen equal to  $2.29 \text{ mm} \pm 0.37 \text{ mm}$  considering both male and female abdomens, according to studies reported in [133]. These values were measured by ultrasound technique and collected on 156 Korean adults with diabetes, and they are consistent with those reported in scientific literature [134][133].

The subcutaneous fat tissue thickness depends on many parameters, such as Body Mass Index (BMI), age, and gender; therefore, the average value of  $10.15 \text{ mm} \pm 6.45 \text{ mm}$  was chosen, considering  $7.75 \text{ mm} \pm 5.03$  for men and  $13.07 \text{ mm} \pm 7.03 \text{ mm}$  for women. Such values are compatible with the values proposed in a study on American diabetic patients [135].

Finally, considering the injection site, the abdominal muscle selected is the Rectus Abdominis (RA) whose size was measured by ultrasound imaging on a total of 123 subjects, 55 men (mean age  $40.0 \pm 14.1$ ) and 68 women (mean age  $33.8 \pm 12.7$ ) in [136]. Men showed to have significantly larger muscles than women, nonetheless, a significant correlation between thickness of RA, weight, and BMI was seen in both genders. The RA thickness was  $1.25 \text{ cm} \pm 0.22 \text{ cm}$  and  $1.02 \text{ cm} \pm 0.16 \text{ cm}$  for men and women respectively.

As regards tissues density, abdomen skin density, fat, and muscle density we estimated to be  $1.10 \text{ g/cm}^3$  in [137],  $0.90 \text{ g/cm}^3$  in [138]  $1.06 \text{ g/cm}^3$  in [139], respectively.

Skin, fat, and muscle Young's modulus are 2.10 MPa, 3.25 kPa, and 110.00 kPa respectively. At last, the Poisson's ratio has been chosen equal to 0.30 for all the

## Impedance measurements in diabetology

tissues, according to [131]. All values are reported in Tab. 2.3." [5]

"These values are used to build a simplified finite element model to evaluate the

Table 2.3 Mechanical and Anatomical parameters.

	Skin	Fat	Muscle
<b>Young's Modulus [kPa]</b>	$2.10 \cdot 10^3$	3.25	110.00
<b>Poisson's Ratio</b>	0.30	0.30	0.30
<b>Density [g/cm<sup>3</sup>]</b>	1.10	0.90	1.06
<b>Thickness [mm]</b>	2.29	10.15	12.50

human abdomen's natural frequencies. A generic abdominal surface  $100 \text{ mm} \times 50 \text{ mm}^2$  centered in the navel was chosen for this analysis. The chosen surface size depends on the futures needed to evaluate macroscopic effects, such as the pressure exerted by the syringe or the injection of the drug, which are not appreciable on infinitesimal areas." [5]

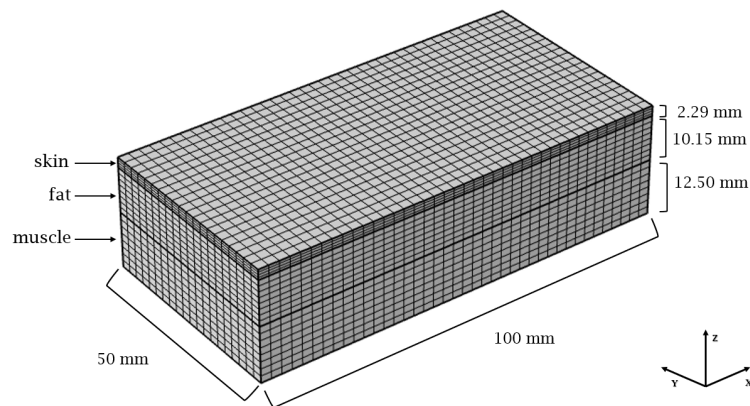


Fig. 2.22 The Finite Element Model of abdominal portion [5].

"The geometrical model is shown in Fig.2.22 with indications of the different layers. Equation 2.3 is solved in this volume with constraints fixed according to [140]. Symmetrical boundary conditions were chosen for all tissues lateral surfaces in order to prevent edge reflection effects. Due to the high difference in skin thickness w.r.t. fat and muscle, the former was treated as a shell and shell-solid connection that was added at the skin-fat interface model the tie constraint set as reported in [140]. Thanks to the geometry of the system, a mapped mesh was generated on the skin's external surface and then extruded along the depth direction, resulting in the hexahedral mesh shown in Fig. 2.22" [5].



### 2.7.3 Numerical modeling

"In a previous work [105], a Finite Element Model (FEM) was implemented to model the electrical behaviour of human tissues and, thus, to manage intra-individual reproducibility uncertainty. In particular, the skin, fat and muscle electrical characteristics for each subject were identified by a preliminary impedance spectroscopy measurement [105]. In this work, a FEM approach introduces a numerical mechanical analysis aiming to estimate tissues deformation contribution to bioimpedance measurements, in order to improve the accuracy in insulin absorption assessment." [5]

"In this regard, it would be necessary to set-up a multiphysics time-dependent study: a mechanical deformation dynamics, coupled with an electrical analysis, will allow to simulate the bioimpedance measurement at the impedance device's terminals. Tissue deformation dynamics is provided by the superposition of the injection/breathing pressure effect, and a number of vibrational modes, both affecting the bio-impedance measurement. When the characteristic time of the mechanical dynamic and the period of the sinusoidal electrical excitation of the tissues are comparable, the analysis complexity and the computational burden are very high. However, this can be significantly reduced when the electrical excitation frequency is much higher than the natural mechanical oscillation frequencies. In this case, it is possible to decouple the mechanical deformation dynamics and the electrical dynamics. This allows to study the electrical field and current density distribution into the tissues, assuming a sequence of quasi-AC regime states, where the deformation is negligible over the period of the excitation voltage. Therefore, the same procedure to simulate the bioimpedance measurement, as shown in [105], can be used.

Hence, this section is focused on a mechanical analysis aimed at evaluating the natural frequencies of the portion of the human body under test. The main aim is to provide indications about the minimum frequency applicable across the bioimpedance' terminals in order to meet the above-mentioned conditions." [5]

#### Theoretical background

"Numerical models and experiments are essential to study the behaviour of human tissues. Since the human tissues are non-homogeneous and characterized by a complex biological structure, many approaches, usually based on a multi-layered

## Impedance measurements in diabetology

---

structure modeling, were developed: for instance, in [141], Flynn developed a finite element model of the skin to study the formation of wrinkles around healing scars. From a mechanical point of view, it is usual to consider human tissues of the abdomen (skin, fat, and muscle) as viscoelastic materials, characterized by stress relaxation, creep, and hysteresis. Their rheological properties determine the stress-strain characteristic when subjected to different external loads. Since the elastic and viscous behaviour of human tissues depends upon their Young's modulus, Poisson's ratio, and density, they could also be used for diagnostic purposes, to retrieve information about disease and treatment progressions from their variations over time [142]. Many techniques have been developed over the years to determine the mechanical parameters: wave propagation methods were adopted to determine the thickness and mechanical properties of the skin; in vivo and in vitro indentation tests were conducted to define the characteristic stress-strain curve of human tissues, and imaging techniques were implemented to improve the accuracy in defining mechanical properties.

Mechanical parameters, once identified, are used in partial differential equations standing the indefinite equilibrium of the tissue, which calculate their stress condition. To calculate the natural vibrational frequencies of the human tissue under test, such equations are solved into the frequency domain with no external loads as stated in 2.3:

$$-\rho \omega^2 \mathbf{u} = \nabla \cdot \mathbf{S} \quad (2.3)$$

where  $\rho$  is the density,  $\omega$  the angular frequency,  $\mathbf{u}$  the displacement field, and  $\mathbf{S}$  the stress tensor.

Equation 2.3 needs to be solved with a proper set of boundary conditions, taking also into account the presence of the remaining part of the abdomen not modeled in our study. Panchal et al. developed a FEM model to estimate the natural frequencies of human skin of the forearm. Symmetry conditions, applied to the model, allow to exclude the edge effects of the section in the results, and to connect each layer to the underlying one by using tie constraints [140]."[5]

### Simulation results

"Natural frequencies of the multi-layer tissue were calculated by solving equation 2.3 with proper boundary conditions by means of finite element analysis. Results are

## 2.7 Measurement method optimization by FEM modeling

reported in Table 2.4. Graphical examples of the simulation results are shown in Fig. 2.23.

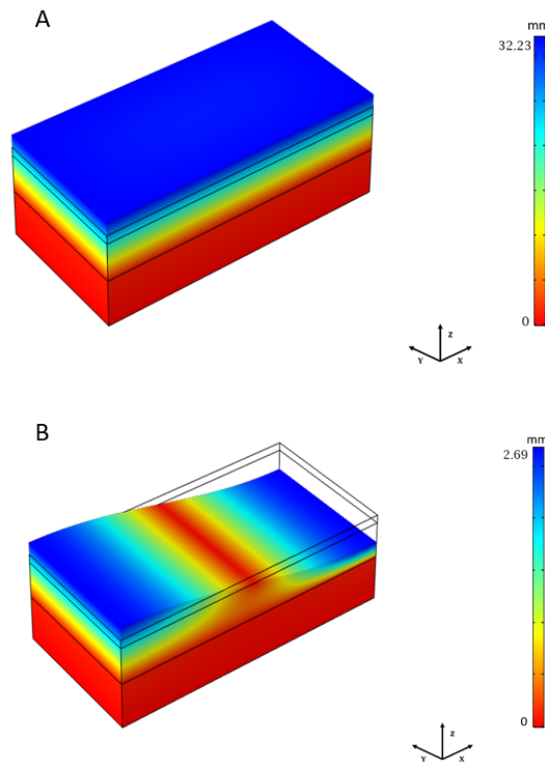


Fig. 2.23 Abdominal portion total displacement: A) at frequency= 19.76 Hz B) at frequency= 27.32 Hz [5].

Table 2.4 First Natural Frequencies of human abdomen tissues. [5]

Natural frequency [Hz]
19.76
27.32
56.87
57.59
58.72
59.79

Table 2.4 shows that the natural frequency of vibrating modes of the multilayered human abdomen falls into the range 19 Hz - 60 Hz. These results provide information regarding the excitation voltage to be applied at the impedance spectroscopy

## **Impedance measurements in diabetology**

---

terminals. Considering that the abdomen deformation generated by the exerted pressure of the insulin injector is slow enough (up to one second), the excitation voltage frequency should be higher than 1 kHz to decouple the electrical analysis, in the frequency domain, from the mechanical transient analysis."[5]

In conclusion in this section, "a feasibility study about the possibility to decouple the mechanical deformation and the electrical dynamics is presented to model the effect of the mechanical uncertainty sources (e.g., the pressure exerted during the injection phase and/or breathing) on the impedance measurement is described. The proposed simplified model is realized by referring to the average values of skin, fat, and muscle thickness and mechanical abdomen parameters, already present and validated in scientific literature. The calculated natural frequencies fall into the range 19 Hz-60 Hz, highlighting the possibility to decouple mechanical and electrical analyses when the excitation voltage is characterized by a frequency higher than 1 kHz. Future developments foresee the study of the deformation dynamics, the subsequent evolution over time of the bioimpedance measured at the bioimpedance terminals, and the experimental validation of the decoupled model."[5]

### **2.7.4 Tissues electrical properties**

The subject-specific finite element modeling allows the optimization of electrodes configuration and adhesion, as well as a better understanding of the human body behaviour our by evaluating the amount of drug actually absorbed.

FEM is a non-trivial task since it requires specific parameters and plenty of time to develop a proper model representation of the system under analysis, particularly if it is a human structure.

Under the best circumstance, it allows modeling soft tissue structures, performing numerical analysis of mechanic and fluid behaviour ours, as well as evaluating the biomechanical behaviour our and morphology of the human body's structures.

The input data requested to properly implement FEM include material properties, geometry, that is, the shape and size of the object of interest, and boundary conditions.

The generic model of the abdomen, useful to improve the sensitivity of the measurement method of insulin transdermal delivery assessment, and choose the best electrodes configuration considering the parameters that affect the most the

## 2.7 Measurement method optimization by FEM modeling

---

measurement. In this part, the electrical parameters used to build the model are described.

"The dielectric properties of biological materials represent a measure of their response to an applied electric field. The electric field and the biological tissues interact at all levels, from the cellular to the molecular level, and their interaction induces conduction and polarization currents within biological systems.

The structure and composition of biological tissues establish the nature and sort of their interaction with electromagnetic fields, and the resulting dielectric spectrum. However, tissues can be modeled as dielectric materials characterized by polarization mechanisms and dielectric losses.

When an external sinusoidal field excites the tissue, the electrical charge displacements generate polarization mechanisms. The dielectric losses arise from conduction currents inside the tissue together with the lossy effects caused by the material polarization. The physical parameter associated with this phenomenon is the electrical conductivity, whose continuous component accounts for the polarization of the bound charges, while the alternate components account for the energy losses due to bound charges and dipole relaxations.

Dielectric properties of biological tissues in the frequency domain are described by a complex and frequency-dependent dielectric function: the electrical permittivity, an intrinsic property of dielectric materials. In dealing with tissues, the dielectric properties are the frequency variations of the relative permittivity and the electrical conductivity, as reported over years by various investigators [12]. The main characteristics of the dielectric frequency properties of biological tissues consist of three main relaxation regions. Each of them is characterized by a specific polarization mechanism, namely  $\alpha$ ,  $\beta$  and  $\gamma$  regions, respectively at low, medium, and high frequency, and other minor dispersion, such as the often reported  $\delta$  dispersion.

Several models were used to describe tissue electrical biological behaviour our. However, the model built on the expressions provided by Cole-Cole is even nowadays one of the most widely employed. The Cole-Cole equation describes the relaxation phenomena in dielectrics and represents a modification of the Debye relaxation. The following expresses the effective dielectric permittivity [143]:

$$\dot{\epsilon}_{eff}(\omega) = \epsilon_{\infty} + \sum_n \frac{\Delta\epsilon_n}{1 + (j\omega\tau_n)^{1-\alpha_n}} + \frac{\sigma_{dc}}{j\omega\epsilon_0} \quad (2.4)$$

## Impedance measurements in diabetology

---

where:

- $\epsilon_\infty$  namely, the infinite permittivity, is the value of permittivity in the high-frequency range, where the dielectric can be considered as unrelaxed;
- $\epsilon_0$  is the permittivity of free space;
- $\Delta\epsilon_n$  is the magnitude of the dispersion described as difference between  $\epsilon_s$  known as static permittivity, and  $\epsilon_\infty$  in relation to the  $n - th$  relaxation phenomenon;
- $\tau_n$  is the relaxation time of the  $n - th$  relaxation phenomenon, that is the necessary time for dipoles to return into a relaxed state after the perturbation by an electromagnetic field;
- $\omega$  is the angular frequency;
- $\alpha_n$  is an empiric coefficient affecting the spectral frequency shape of the  $n - th$  relaxation phenomenon; in particular, its range is  $0 < \alpha_n < 1$  and the higher its value, the higher the flattening of the spectrum;
- and  $\sigma_{dc}$  is the static conductivity.

Several studies investigated the electrical characterization of human biological tissues, ranging from skin, fat, muscles, and bones. Tab. 2.5 summarizes some of the most extensive and detailed electrical characterization works of biological tissues [144–146]." [1]

The electric model was built by using the same geometry as the mechanical model. The electrical properties of tissues in this model such as permittivity and conductivity have been evaluated by the model proposed by Gabriel. Since the skin represents a very complex tissue composed of several layers, for the electrical model, it was schematized in only two layers, namely wet and dry. Where Dry Skin models the outermost part of the skin, i.e. stratum corneum and lucidum; Wet Skin models the stratum granulosum, spinosum, basale, and dermis. Then, Subcutaneous Fat Thickness (SFT) represents the hypodermis with subcutaneous adipose tissue;

## 2.7 Measurement method optimization by FEM modeling

Table 2.5 Different tissues parameters value of Cole-Cole equation according to Gabriel [12].

	<b>Dry Skin</b>	<b>Wet Skin</b>	<b>Fat</b>	<b>Muscle</b>
$\epsilon_{\infty}$	4.0	4.0	2.5	4.0
$\Delta\epsilon_1$	32.0	39.0	9.0	50.0
$\tau_1$ [ps]	7.23	7.96	7.96	7.23
$\alpha_1$	0.00	0.10	0.20	0.10
$\Delta\epsilon_2$	1100	280	35	7000
$\tau_2$ [ns]	32.48	79.58	15.92	353.68
$\alpha_2$	0.00	0.00	0.10	0.10
$\Delta\epsilon_3$		$3.0 \cdot 10^4$	$3.3 \cdot 10^4$	$1.2 \cdot 10^6$
$\tau_3$ [ $\mu$ s]		1.59	159.15	318.31
$\alpha_3$		0.16	0.05	0.10
$\Delta\epsilon_4$		$3.0 \cdot 10^4$	$1.0 \cdot 10^7$	$2.5 \cdot 10^7$
$\tau_4$ [ms]		1.592	15.915	2.274
$\alpha_4$		0.20	0.01	0.00
$\sigma_{dc}$ [S/m]	0.0002	0.0004	0.0350	0.2000

By exploiting the electrical model, different configurations of electrodic distances were tested, by changing the distance between different electrodes, in order to find the one that can maximize the sensitivity of the impedance measurements during the insulin injection.

The sensitivity analysis shows that the most significant parameter is the Voltmetric electrode distance from the center. So once the most relevant parameter was found, and it is shown in Fig. 2.25, the setup was fixed while the parameter changes as shown in Fig. 2.24, where the sensitivity is assessed as the normalized difference between the impedance measured without and with the drug in the tissue.

## Impedance measurements in diabetology

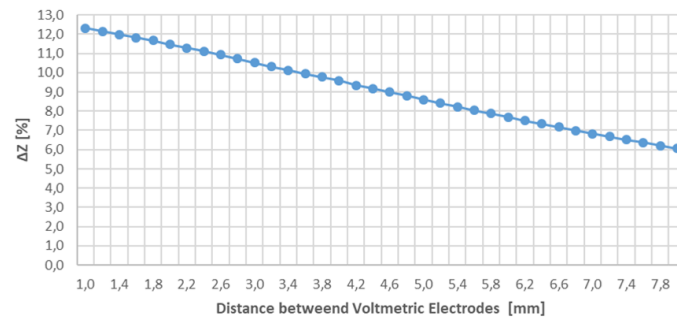


Fig. 2.24  $\Delta Z$  [%] vs distance between Voltmetric electrodes.

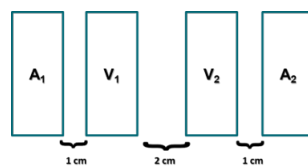


Fig. 2.25 Optimal electrodes configuration.

## 2.8 Experimental activity

An experimental campaign was carried out to evaluate the impact of any mechanical stress acting on the human abdomen on the impedance measurement. Twelve volunteers were involved in the experimental campaign, 6 men and 6 women. The volunteers were free of pathologies, have a normal weight, aged between 25 and 60 years, belonged to the same ethnic group, with high education level, and other physical parameters are shown in Tab. 2.6.

Table 2.6 Means characteristics of volunteers enrolled in the study.

<b>Sample population's means characteristics</b>	
<b>Age</b>	$35.33 \pm 14.43$
<b>Weight [kg]</b>	$72.58 \pm 14.33$
<b>Height [m]</b>	$1.71 \pm 0.07$

They signed the informed consent before the experiments and the procedures were implemented in accordance with the appropriate directive and guidelines.



## 2.8 Experimental activity

The data acquisitions were recorded at Università degli Studi di Napoli Federico II, in a room where was constantly monitored the temperature and the humidity. The experimental setup, shown in Fig. 2.26 includes: (i) 4-wire bio-impedance spectroscopy (Insulin Meter), (ii) electrodes, (iii) a camera placed on a support that records the experimental activity in real-time (iv) a laptop with a specifically GUI that processes and stores data in real-time (v) a compression dynamometer customized ad hoc for the force application on the selected abdomen region (vi) medical examination table for positioning the volunteers.

The camera recorded the abdominal deformations (due to breathing or pressure). These data are recorded simultaneously with the impedance measurements by a laptop, that processes them and show them in real-time) the time-trace of the impedance magnitude on the monitor. These videos are fundamental to relating the impedance magnitude variation and the deformations of the tissue. A dynamometer is used to apply the desired force on the abdomen investigated zone. The dynamometer was equipped with a 3D printed support, able to mimic a standard insulin pen. Finally, the volunteers lay on the examination table in the supine position, to undergo the measurement without the risk of creating errors due to the movement and/or loss of partial adhesion of the electrodes.

The four pre-gelled electrodes were placed on the abdomen 6 cm far away from the navel (on the left of Fig. 2.27 ); the inter-distance of the voltmetric electrodes was 2 cm, whilst the distance between the voltmetric and the amperometric electrodes was 1 cm.

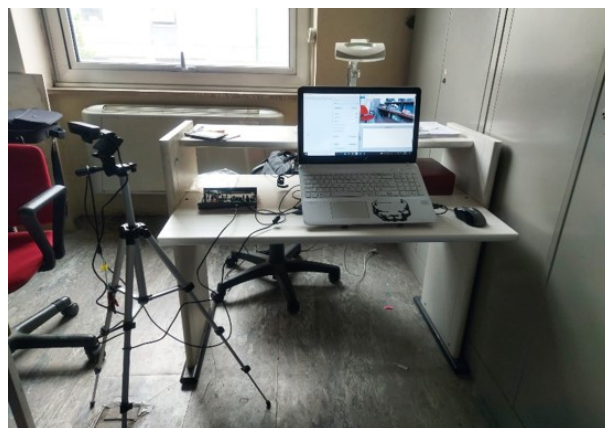


Fig. 2.26 Experimental set up including: Analog AduCM350, dynamometer, electrodes FIAB PG 500, tripod, and camera.

## Impedance measurements in diabetology

---

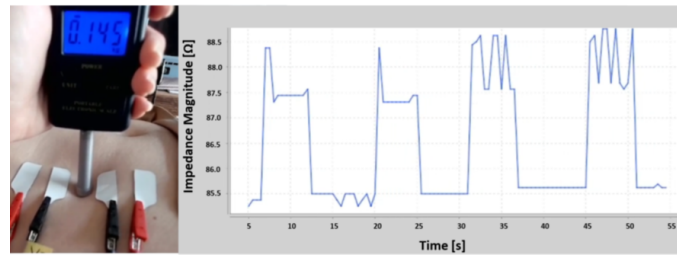


Fig. 2.27 Picture of volunteer's abdomen on the left; Impedance magnitude time-trace at 10 kHz. Impedance variation due to four cycles of compression and relaxation of the tissue, on the right [6].

The experimental procedure includes different phases. Impedance measurements were recorded by using the previously described Insulin Meter, at 100 mV sinusoidal voltage amplitude and 10 kHz frequency. In the first part, the volunteers were asked to simulate natural breathing, forced breathing, and apnea. During this part, the volunteers had to breathe in a natural and relaxed way in order to assess the impedance values during the rest of the investigation area. Then, the volunteers were required to inhale and exhale in a forced way, to record the corresponding impedance variation. Finally, they were asked to perform 5 s of apnea, to characterize impedance behaviour our also in this circumstance.

Once this first phase is completed, the second experimental phase starts. During this part, different forces were applied to the tissue by the compression dynamometer, in order to assess the tissue response and the corresponding impedance variation. The pressure values were chosen on the basis of the typical pressure applied during the insulin injection, in particular, 5 applied forces in the range [0.40 N -1.96 N]. Each force was applied for 10 s, and after a rest of 10 s the next force was applied meanwhile the corresponding impedance variation was recorded.

The volunteers were required to lie down in a supine position and remain as quiet and motionless as possible during data acquisition. Such behaviour ours are fundamental for the success of the measurement, in fact, volunteers' states of agitation and/or nervousness could lead to irregular breathing phases that negatively affect or distort the measurement [147], as well as abdominal movements different from normal breathing could cause a displacement or disconnection of the electrodes that would cause an alteration in the measured value.

### 2.8.1 Data processing

An example of recorded normal and forced breathing is shown in Fig. 2.28. "During strong breathing, the impedance value increased during the inspiration phase while it decreased during the expiration phase, as shown in Fig. 2.28. Regarding normal breathing, the impedance variation was not appreciable. Indeed, the standard deviation was evaluated for both tasks to understand the instability of the setup. During normal breathing, a standard deviation of 0.20  $\Omega$  was obtained. During forced breathing, the standard deviation was greater than 0.64  $\Omega$ ."

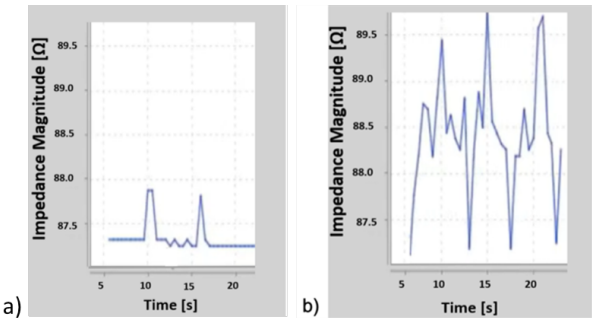


Fig. 2.28 Impact of breathing intensity on impedance measurements. Normal breathing a, strong breathing b) [6].

While considering the second phase of the experimental procedure, data analysis was conducted by evaluating the average force applied on the tissue, by considering the mean value of dynamometer reads during the application of a single target force. While the mean impedance values were normalized with respect to the value before the force application. The results are shown in Fig. 2.29.

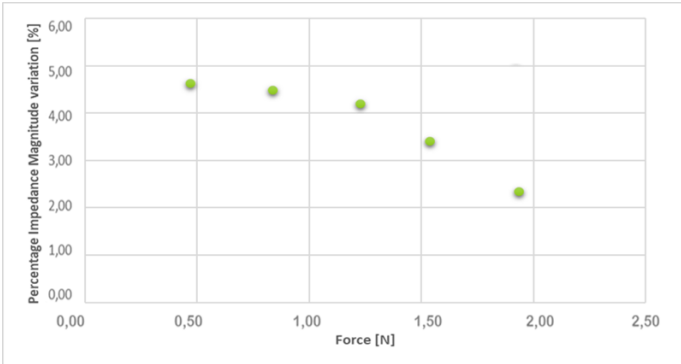


Fig. 2.29 Average percentage impedance magnitude variation during force application.

## Impedance measurements in diabetology

---

Experimental results show a progressive decrease in the relative impedance magnitude variation according to an increasing external force which is comparable to the typical mechanical action of insulin injection.

The plot (Fig. 2.30) shows in light blue measured impedance values when the force was applied in consecutive increasing force values. While the green points represent the impedance values measured when consecutive decreasing force values were applied. The impedance average variation values, depending on the average values of force applied, as shown in Fig. 2.30, where each point represent the average impedance variation percentage evaluated for all the subject according to the specific applied force.

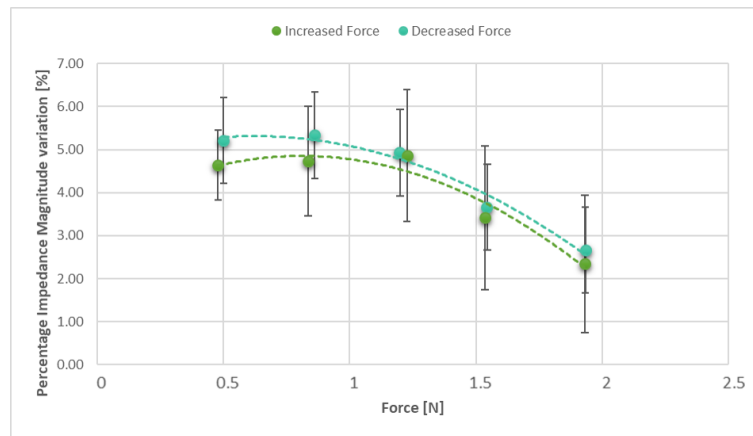


Fig. 2.30 Impedance variation in function of the applied increasing and decreasing force.

Once the experimental data were obtained and processed and the software simulation of the abdomen model was completed; the obtained results were compared. By comparing then the results obtained from the experimental campaign, and the results obtained from the FEM simulations, it results that according to the selected applied forces, the obtained impedance values have a similar trend which demonstrates good modeling of the simulated tissue.

### 2.8.2 Conclusions

In conclusion, in the first part of this section, a model of the abdominal tissue through finite element model (FEM) software was built to study its mechanical behaviour or during the application of a force comparable to the insulin injection forces.

Then, the results are transposed to the electrical domain to simulate the electrical behaviour or of the model.

The second step was to verify the results with those obtained from an experimental activity conducted on 12 volunteers. The experimental campaign was carried out by using a suitable experimental setup that emulates the choices made during software modeling.

The objective of the experimental campaign was to evaluate the impedance variation during the application of different forces on the abdomen by means of a dynamometer.

The comparison of the results shows a good correspondence between the simulated model and the experimental data. The results obtained therefore confirm the validity of the method and can greatly improve the algorithm of the artificial pancreas. The latter allows to better personalize the insulin therapy by calculating the correct dose of insulin to be injected, and taking into account that the absorption curve may change according to the applied injection force.

Further studies may consider not only the impedance magnitude but also the impedance phase and conceive a more complex and stable experimental setup that can be used for everyday applications.

Another future development is the creation of a more complex model able to simulate all the layers of abdomen tissue.

Finally, validating the method, it may be possible to equip the insulin pens with a force sensor that estimates the force applied on the tissue during the injection and transmit the information in real-time to the artificial pancreas, allowing thus optimal bolus calculation.

# Chapter 3

## Impedance measurements in dentistry

Some of the work described in this chapter has been previously published in [1], [9], [10], and [11]

### 3.1 Human teeth structure: anatomy and composition

Teeth are very resistant mineralized structures of different shapes and sizes; they are the hardest tissues of the human body. They are essential to chew food and they play a main role in speaking, beside that, they are also important for aesthetic reasons.

In humans, the permanent teeth are preceded by a temporary or deciduous or milk dentition, so-called since they will be entirely replaced by the teeth of the permanent series, and by a mixed dentition (simultaneous presence of deciduous and permanent). Chronologically, the deciduous teeth begin with the eruption of the first deciduous tooth, i.e. the lower central deciduous incisors, around 5 months of age, and continue until the last milk tooth falls out, usually around 12-14 years of age. The deciduous teeth are generally smaller than their permanent homologous, despite the similar shape their enamel is whiter.

In the adult oral cavity, there are 2 dental arches, one upper and one lower. Each of the two arches can then be divided into two hemiarches, or right and left quadrants, divided by the median sagittal plane.

There are several ways to indicate teeth' position within dental arches, one of the most popular approaches is to number sequentially the teeth starting from the midline,

### 3.1 Human teeth structure: anatomy and composition

dividing the upper and lower dental arches at the midline (Fig. 3.1) according to international code guidelines from the FDI.

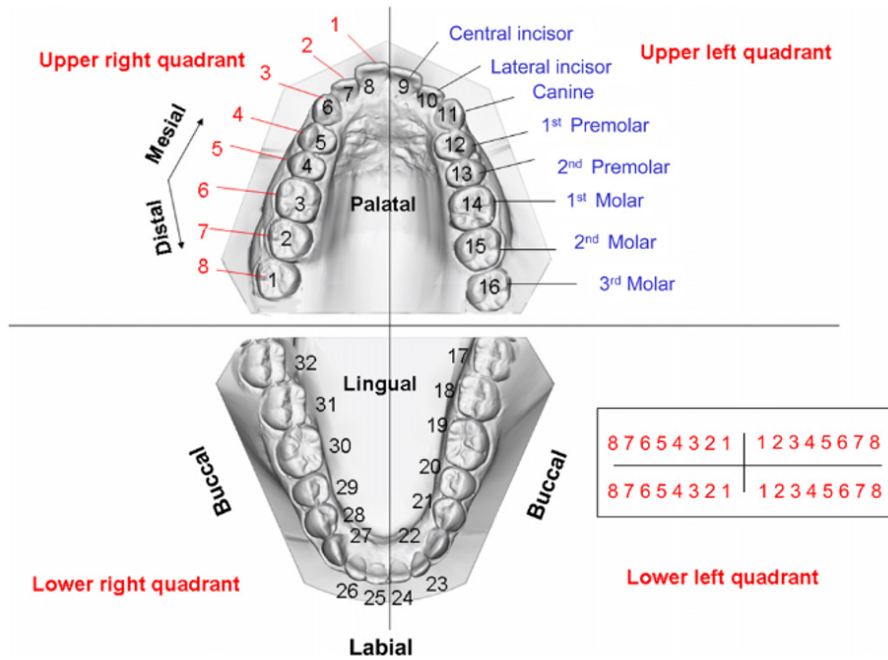


Fig. 3.1 Maxillary and mandibular adult arches representation. The two arches are divided into 2 sub-arches or four quadrants (red), divided by the median sagittal plane. Teeth are numbered sequentially starting from the right maxillary third molar (number 1 black) or according to the quadrant, from mesial to distal in each quarter (red numbers). Teeth orientation are: labial, buccal, lingual, and palatal [7].

While for describing tooth surfaces and their orientation are used the following words:

- Vestibular: external surface, facing the vestibule;
- Palatine or lingual: internal surface facing the palate, for the upper teeth, or the tongue for the lower teeth;
- Occlusal: the upper face of the tooth essential for chewing;
- Incisal: the upper face of the anterior teeth that have none occlusal surface
- Interproximal surfaces:

## Impedance measurements in dentistry

---

- Mesial: facing the midline (going towards the center) toward the mid-sagittal plane along the dental arch;
- Distal: facing an opposite direction of the sagittal plane (away from center) along the dental arch.

There are four types of teeth, divided by shape, function, and position in the dental arch: incisors, canines, premolars, and molars (Fig. 3.2). In each quadrant, under normal conditions, with all the permanent teeth erupted, there are 8 teeth. Each dental class has a specific function:

- Incisors: breaking up food and articulating sounds;
- Canines: guide in lateral movements and tearing of food;
- Premolars and molars: grinding of food.

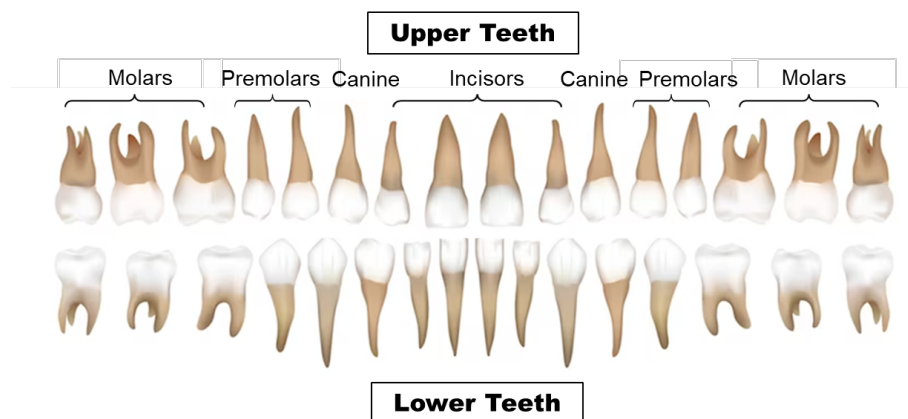


Fig. 3.2 Teeth present in the dental arch of adults: the incisors (4), the canines (2), the premolars (4), and the molars (6). With 16 teeth in the maxilla, the bony upper part of the jaw, and 16 teeth in the mandible, the bony lower part of the jaw.

### 3.1.1 Tooth anatomy

The tooth can be classified from a histological and structural point of view. Starting from a structural point, we find: crown, neck, and root (Fig. 3.3).

The crown is the outermost surface of the tooth structure above the cementum-enamel



### 3.1 Human teeth structure: anatomy and composition

---

junction and its shape changes according to the different teeth. The clinical crown is the tooth structure above the gumline, visible in the mouth, on the other hand, the anatomic crown might not be visible, since covered by the gum tissue. However, both anatomic and clinical crowns have the same structure [148].

The neck is the part between the crown and the root of the tooth, surrounded by the gumline. It represents the preferred location by bacteria to accumulate plaque and tartar. In a healthy dentition, the gum covers the neck, but due to some pathologies or wrong brushing technique, which damage the gum, the tooth neck can be exposed. The root is the non-visible part of the tooth that extends into the bone and holds the tooth in place. The root changes according to the different kinds of teeth, e.g. the incisors have a single root, the molars instead have double or triple roots [148]. From a histological point of view, the tooth anatomy includes enamel, dentin pulp, and cementum.

Enamel is the tissue that covers the entire crown. It is a calcified, avascular, very hard tissue, with a poor content of protein and water. The enamel is characterized by extreme hardness (about 8 on the Mohs scale), it is the hardest tissue of the human body but is very fragile. Fragility is evident when the below dentin is missing and the enamel can easily fracture. One of the main characteristics of the enamel is the high solubility in acids, which affect the enamel not uniformly, indeed the areas with the higher inorganic content are more susceptible to acids attack.

The enamel primarily contains hydroxyapatite (crystalline calcium phosphate); its structure is characterized by many elongated units, arranged in a parallel manner, in overlapping rows. These units, namely enamel prism, run from the border with the underlying dentin to the surface. The enamel colour is generally translucent and opalescent and reveals the colour of the underlying dentin; ultimately, the colour of the tooth depends on the thickness of the enamel and the dentin colour. According to the different light directions, the colour may vary from white to ivory, with slight shades of yellow, when dentin is present or can appear blue-white when there is none. In case of enamel defects, as in hypomineralization, or alterations of the enamel structure, the colour can become dull yellow to dark red-brown [149].

Dentin is the main supporting structure of teeth and is the second hardest tissue in the body after enamel. It is positioned under the enamel and surrounds both the dental pulp and reaches the root. Dentin is a calcified tissue of mesenchymal origin, it is yellowish in color. Dentin is mainly composed of hydroxyapatite but less mineralized than enamel, in fact, it is characterized by 70% mineral and acellular,

## Impedance measurements in dentistry

---

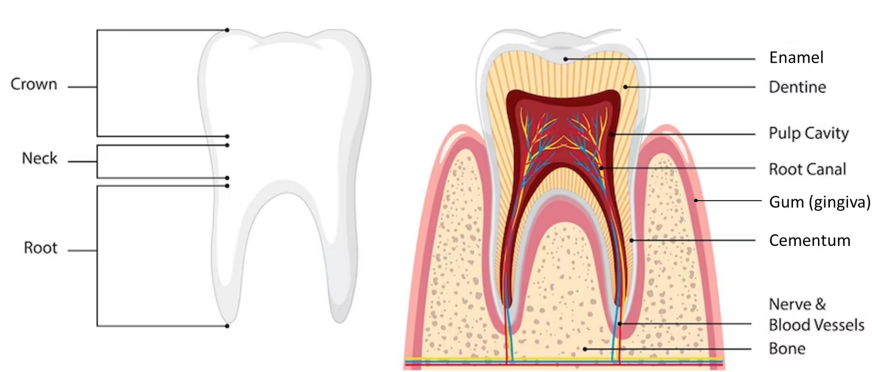


Fig. 3.3 Normal tooth anatomy and a cross-section view.

such as hydroxyapatite crystals, and 30% organic components, such as water, and collagen, generated by odontoblasts, which are the cells present in the pulp. The dentin is crossed by dentinal tubules, which start from the dental pulp and run almost perpendicularly to the external surface. When the dentin is exposed, i.e. when the tooth loses its external enamel coating, the tubules can transmit pain to the pulp.

Cementum is a mineralized tissue covering the entire root surface; it ensures the anchoring of the periodontal ligament to the root surface. It is a calcified avascular tissue, which does not undergo dynamic remodeling over the years. It is markedly different from enamel and dentin due to its embryological origin, structure, function, and physico-chemical properties [150].

The pulp is the only soft tissue of the tooth, consisting of an organic component for 30% and water for 70%. Embryologically, the pulp derives, like the dentin, from the dental papilla. It is a highly vascularized and innervated connective tissue located within the pulp chamber. At the pulp center extracellular matrix is composed of collagenous fibers, vessels, and nerves. At the end of the pulp canal in the root, the pulp is connected with the periodontal ligaments, and thus to nerves and vessels [151].

### 3.1.2 Tooth composition

Enamel, dentin, and cementum are characterized by both organic and inorganic components, most of their mechanical properties are the results of their internal microstructure. Indeed, the enamel is the hardest tissue and more highly resistant to force of human body, this property is fundamental to fulfill physiological functions,

### 3.1 Human teeth structure: anatomy and composition

---

namely to biting and chew food, and protect the inner pulp, where the nerves reside. As mentioned above, cementum, and dentin are specialized connective tissues, whose organic component about 90% is collagen type I. On the other hand, enamel has little or no collagen, and its organic matrix is made up of noncollagenous protein. Regarding inorganic content, enamel has about 90% prismatic crystals, while dentin is about 70% and cementum is 45%. During odontogenesis, the tooth develops its ultimate structure, and the dentin has the ability to regenerate its tissue, while the enamel cannot regenerate itself [152].

The properties of each tissue depend on the ratio of inorganic-to-organic contents which vary from tissue to tissue. For instance, dentin has a higher organic amount, and thus, it is less hard and more resilient than enamel. The inorganic component of teeth tissues consists of biological apatite,  $Ca_{10}(PO_4)_6(OH)_2$ . The unit cell of hydroxyapatite (HA) has a hexagonal structure; repetitions of the unit cells produce crystals of various sizes. Enamel crystals are bigger and extremely oriented than dentin, the high orientation of crystals ensures a better resistance and coverage of all the pores present on the tooth surface; for the enamel, the crystals are known to be between 40 nm and 120 nm wide, 25 nm thick, and 60 nm – 100 nm long. While in dentin, the crystals are about 20 nm in width, 2 nm - 5 nm in thickness, and 40 nm - 60 nm in length [153]. An example of demineralized enamel with residual hydroxyapatite crystallizes is shown in Fig. 3.4.

From a crystallographic point of view, in hydroxyapatite structure some common substituents can be encountered, such as the incorporation of the fluoride ion into the crystal lattice, the replacement of the  $Ca^{2+}$  cation with  $Mg^{2+}$ ,  $K^+$  or  $Na^+$ . The  $OH^-$  hydroxyl site can be replaced with  $F^-$  or  $Cl^-$  atoms, and again the  $PO_4^{3-}$  site can be replaced with carbonate anion  $CO_3^{2-}$ .

These possible substitutions, as well as the concentration of those elements, significantly change the chemical and physical characteristics of the HA, and the resistance of the HA against acid attacks, leading, for example, in the case of carbonate hydroxyapatite to an increase in solubility in an acid environment; instead, a reduction in solubility may occur in case of fluorapatite [154].

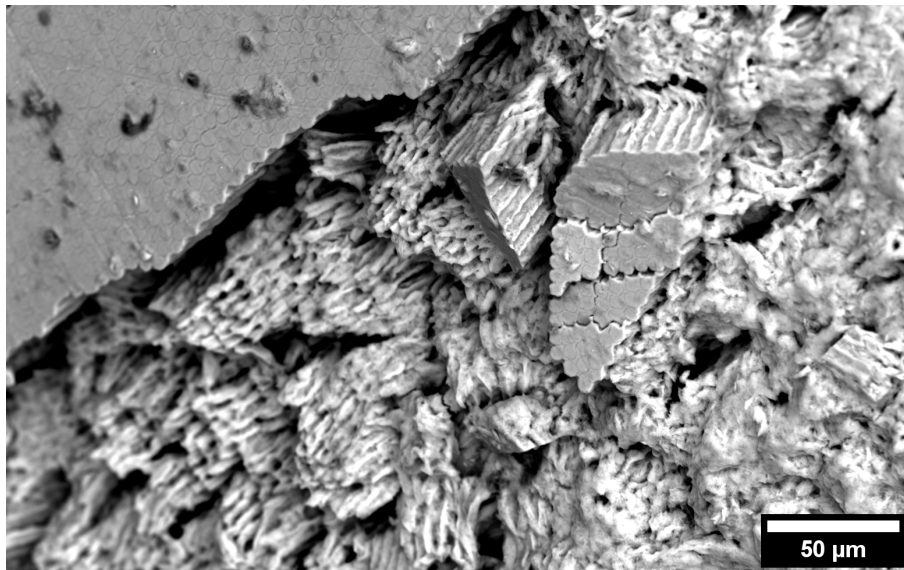


Fig. 3.4 SEM image of the organized enamel rods (prism) after dental enamel demineralization, residual hydroxyapatite crystallites show a rod-like morphology in the lesion on the enamel surface.

### 3.2 Tooth demineralization

Demineralization refers to the process of removing mineral ions from HA crystals of hard tissues such as enamel, dentin and cementum, the principal components of teeth. The demineralization process is reversible; as partially demineralized HA crystals can return to their original size by restoring lost mineral ions again to the HA crystals through remineralization treatment. Demineralization is a pathological process that affects people of all ages, it involves both deciduous and permanent dentition, and its prevalence increases with age, indeed the crystallinity of dental HA decreased with age. The processes of demineralization and remineralization take place constantly during the day in the oral cavity [152].

Demineralization and remineralization are multifactorial dynamic processes that are not only dependent on a pathological element but on various factors, defined as risk factors. They are divided into 4 main groups: Biological, Chemical, behavioural, and Health; as shown in the table below (Tab. 3.1). Some of these factors are intrinsic, mainly related to individual characteristics such as gender, genetics, and disease states, the latter can sometimes be treated with medications or drugs that can be considered modifying factors since they can change the biochemical characteristics of the elements present in the oral cavity. On the other side, extrinsic factors are

### 3.2 Tooth demineralization

Table 3.1 Risk factors associated with tooth demineralization.

Biological	Chemical	Behavioral	Health
Saliva flow	Oral pH	Eating habits	Current health and Socioeconomic status
Saliva composition	Acid type in oral cavity	Oral hygiene	Medication and drugs
Tooth anatomy	Chelation potential	Brushing frequency	Pathologies and medication

the influence from outside; they include eating and drinking habits, and medication. Other modifying factors that can affect oral health are behavioral patterns such as regular tooth brushing, and cultural and socioeconomic status.

The main consequences of demineralization are erosion and carious lesions [155]. As previously described, human teeth mainly consist of the phosphate-based mineral HA in the enamel and collagen in the dentin, constantly exposed to the oral microbiota, drink, and food. The enamel layer of the dental crown protects all the tooth from localized demineralization, due to the organic acids produced by plaque microorganisms, which destroys the mineral content from the surface of HA crystals. The microbial attack from bacteria existing in the oral cave and dietary acid consumed through drink or food are the two main causes of teeth' chemical demineralization. During the demineralization by acid attack, the chemical dissolution of the inorganic and organic dental matrix occurs. The water content in enamel and dentin allows acid diffusion within the tooth and the mineral loss out of the tooth.

The HA mineral crystal dissolution occurs when the pH level of the dental plaque is lower than 5.5. Indeed, the chemical equilibrium between the enamel HA ( $Ca_{10}(PO_4)_6(OH)_2$ ) and the dissolved HA in the plaque biofilm is reached in an environment with a pH of 7.4. When acids of nonbacterial origin or mechanical damage cause the loss of hard tissues, dental erosion occurs.

Dental erosion is the result of two chiefly chemical methods: direct acid attack or chelation. The tooth becomes more sensitive to mechanical wear and softer as the HA is solubilized due to the acid exposure. During the acid attack, a process of chemical dissolution of both components of the inorganic and organic matrix (such as lipids and proteins, mainly present as a very thin coating of the single crystals of HA) begins. This chemical dissolution process is mainly determined by the water content present in the material. In fact, the concentration of water in the enamel and

## Impedance measurements in dentistry

---

dentin, the latter having a water content greater, about 20% compared to the enamel which has about 12%, is sufficient to allow the diffusion of the acid inside of the tooth due to the leakage of minerals, such as  $Ca$  and  $PO_4$ , out of it.

In addition, dentin has not only a higher concentration of water, compared to enamel, but it also has a component of type I collagen, phosphoprotein, and proteoglycans. Moreover, the dentin has a higher concentration of HA Carbonate (6% vs 3% of the enamel) and a smaller size of the HA crystals which, overall, lead to greater sensitivity to acid attack.

### 3.2.1 Dental caries

Dental caries is a dynamic multifactorial disease process that involves mineralized dental structures during repeated cycles of demineralization and remineralization throughout the day in the presence of fermentable carbohydrates, saliva, and cariogenic oral flora [156]. Dental caries starts when the crystalline mineral structure of the tooth is demineralized by organic acids produced either from biofilm or dietary that lower the pH. Saliva is crucial to maintain the mineral homeostasis of tooth surfaces by buffering the oral environment at a neutral pH and providing the minerals necessary for remineralization. The presence of dental plaque, namely the oral microbiota biofilm that grows on the tooth surface, is the first requirement for caries formation. However, its occurrence does not imply the disease. Actually, a complex interaction of factors with dental plaque, including tooth surface, saliva, and free dietary sugar, lead to the carious lesion.

Despite the large number of acids produced by dental plaque, the lactic acid, the main final product of sugar metabolism, is the principal acid participating in dental demineralization and subsequent caries formation. However, the demineralization process can be stopped when the pH of dental plaque returns to neutrality thanks to swallowing sugar and the buffering action of saliva [157].

The metabolic activity of cariogenic microorganisms, present in dental plaque biofilm, demineralizes the tooth; the tooth enamel surface became more porous and softer due to the mineral loss and the expansion of intercrystalline space, leading thus to the formation of carious lesions.

Despite the surface layer appears smooth and unaffected by the attack, demineralization, thus, enamel caries may occur at a subsurface level. This subsurface lesion

### 3.2 Tooth demineralization

is commonly known as “white spot lesion” which represents an opaque white area that differs from healthy enamel, the lesion can become brown due to the absorption of pigments into enamel pores. However, this earliest visible symptom of demineralization can be detected during an oral checkup by an expert dentist.

This caries stage is clinically important since the process can be stopped by applying preventive measures and changing risk factors. This preliminary stage of the carious process can be classified according to the International Caries Detection and Assessment System (ICDAS) score as 1 or 2 (First visual change in enamel).

The "ICDAS is a standardized visual detection system, with a clinical scoring system used in dental education, clinical practice, research, and epidemiology for detection and assessment of caries activity"[9]. According to the severity of the carious lesion, the ICDAS detection codes range from 0 to 6 as shown in Fig. 3.5.

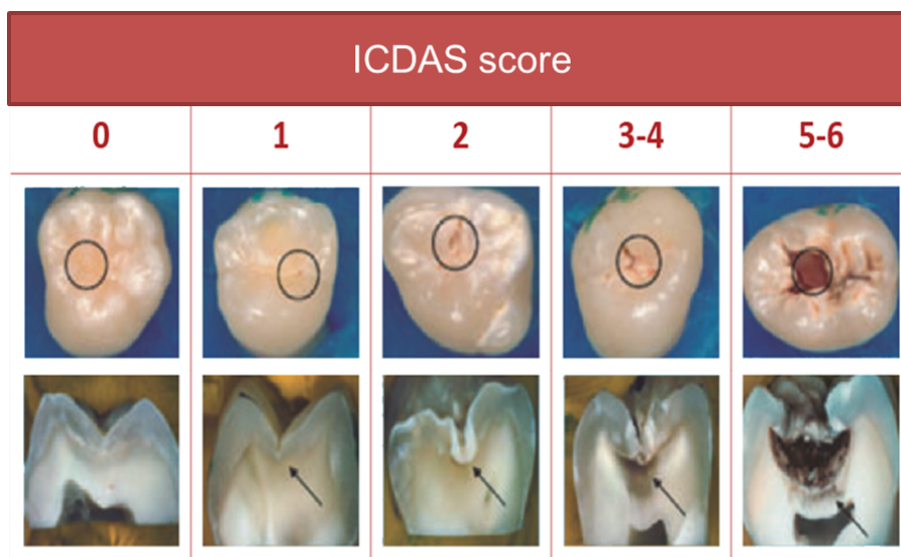


Fig. 3.5 ICDAS clinical visual codes, based on evidence of the histological severity of carious lesions at different caries stage [8].

ICDAS classification of the carious lesions activity at different caries stages is made by different predictors, such as the colour of the lesion, if the lesion is cavitated or non-cavitated, if it is matte or shiny, and its location, the tactile feeling when the dental explorer cross the lesion and when located along gingiva, if the latter bleeds during the dentist examination [158]. This caries stage is clinically important since the process can be stopped and remain inactive lesions by applying preventive measures and changing dietary practices and fluoride availability. In

## **Impedance measurements in dentistry**

---

some cases, the carious lesion can progress to a more extensive stage of destruction; when the porosity increases it can create microcavitation in the enamel (ICDAS code 3, i.e., localized enamel breakdown, without clinical visual signs of dentinal involvement). It can happen that the demineralization continues and the crown may collapse producing a visible cavitation (ICDAS code 5 or 6, distinct or extensive cavity with visible dentin). When the severity and extent of caries are irreversible, restorative treatments are required, also to satisfy patients' functional or aesthetic needs or limit the symptoms. Occasionally caries process continues and it may compromise the dental pulp, required thus a root canal treatment, or tooth extraction.

Considering the burden of dental caries in the world in terms of the number of people affected, cost, pain, facial and systemic issues or infection, and loss of time from work and school; it is imperative that the new approach for early caries detection and caries lesion management become minimally-invasive and able to be tailored and cost-effective in order to prevent disease progression and improve aesthetics, strength, function, and patients compliance. As a matter of fact, non-cavitated lesions at their initial stage can be remineralized using opportune technologies avoiding thus invasive treatments.

### **3.3 Carious lesion detection: Experimental procedure**

"The limited availability of human teeth and the impossibility to perform in-vivo experiments is the main reason for the development of in-vitro studies. In the last decades, scientific literature widely exploited in-vitro demineralization tests to investigate essential processes related to mineral loss and carious advancements [159]. The possibility to use human teeth enables experimental systems to mimic the natural caries process. Nevertheless, the dynamic process of dental carious is not easily replicable since the enamel surface is continuously subject to cycles of demineralization and remineralization in the oral environment [73].

Moreover, this kind of approach cannot take into account all the environmental factors that affect the enamel demineralization and carious lesion process, and despite the use of human teeth being advisable for the study, they present a high inter- and intra-variability, due to several factors, including teeth age and dietary habits.



### 3.3 Carious lesion detection: Experimental procedure

---

However, the main benefits of models and in-vitro tests are the possibility to reproduce any kind of carious lesion, e.g, white spot lesion, secondary caries restorations, or caries around orthodontic brackets as well as root and dentin caries, in a shorter period of time compared to the natural caries process [160][161]." [11] The first part of this work focused on the possibility to employ impedance spectroscopy as a non-invasive method for caries detection. Hence, different human teeth were used for the experiments, both sound and with carious lesions promptly classified by expert dentists. Then, different probes were tested in order to improve measurement quality.

"All teeth were collected with informed consent in the Department of Cariology and Operative Dentistry, University of Turin (Italy). The ethical committee of the University of Turin approved the study protocol (DS\_00071\_2018)." [10]

"After extraction, the teeth, examined and classified by an expert dentist, were cleaned and soft tissue debris and bone fragments were removed. Then, the extracted teeth were stored in hermetically sealed vials containing 0.5% w/v sodium hypochlorite (NaClO), with the aim to avoid dehydration. All measurements were performed promptly after taking out the specimens from the hypochlorite solution and externally drying them with tissue paper. A dedicated 3D-printed PLA support, fixed into the measuring cell, was used as a teeth sample-holder, to guarantee the proper measurements execution without damaging the tooth." [10]

An example of the schematic representation of the measurement procedure is shown in Fig. 3.6. In the measuring cell, approximately two-thirds to three-quarters of the tooth were soaked in Ringer's solution or in physiological saline solution (0.9% w/v sodium chloride - NaCl - solution). Both solutions avoid drying wet samples and offer good sample visibility during the measurements.

Impedance measurements were carried out in-vitro, using the Ivium-n-Stat potentiostat (Ivium Technologies BV, Netherlands), connected to a laptop, with a two-electrode setup, using different probes as working electrode:

- a Ni-Cr wire working electrode with a diameter of 0.5 mm, placed in contact with the coronal access cavity on the surface of the tooth;
- Ni-Cr wire embedded with a hydrogel hemisphere of agar with a diameter of 5 mm, placed in contact with the coronal access cavity on the surface of the tooth;

## Impedance measurements in dentistry

---

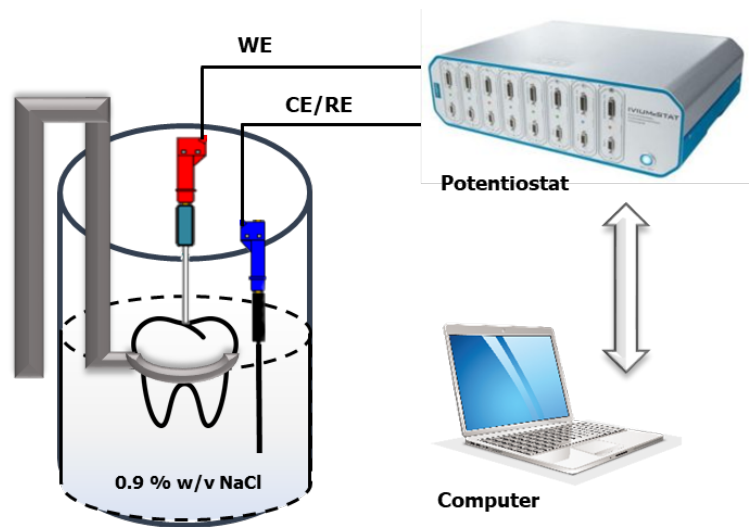


Fig. 3.6 Impedance measurements experimental setup: the measuring cell includes the examined tooth, placed in 3D-printed PLA support, partially immersed in the solution, mainly physiological saline solution; the working electrode on the tooth surface while the counter electrode is in the solution; both electrodes connected to a computer-controlled Potentiostat [9].

- a Ni-Cr counter electrode, with a diameter of 0.5 mm, dipped in the physiological saline solution or Ringer's solution.

"Hydrogels are widely used in impedance measurements in different scientific fields since they represent a simple and affordable way to prepare reliable, easy to handle, and personalized electrodes [162] [163]."[10]

"The agar hydrogel was used to improve the electric contact with the tooth surface and to make the measurement setup more stable. The hydrogel probe was realized by mixing 10 g of dehydrated agar powder (Sigma-Aldrich) in 100 cm<sup>3</sup> of distilled water. Then, the solution was brought to the boil while stirring, until the powder was fully dissolved. Finally, the solution was placed in a special mold and allowed to cool until the solidification". [10]

During the experiments, in order to prevent the drying of wet samples and offer good sample visibility during the measurement, saline solution, and Ringer's solution, were used, due to their ability to simulate the inner environment of a living body. In particular, Ringer's solution "is a fluid isotonic with both the blood and artificial saliva, and it simulates very well the oral environment and the aggressiveness of body fluids. Therefore, it is an optimal choice in many in-vitro tests and in the characterization of the interaction between biomaterials and physiological environments

### 3.3 Carious lesion detection: Experimental procedure

---

[164] [165]. A great benefit of immersion of soaking the samples in artificial body fluids is the possibility to easily and quickly perform experiments without involving animals in the initial stages of research." [10].

#### 3.3.1 Impedance Measurements and Data Acquisition

Following the previously described setup, human third molars and decayed canines, extracted within one year, were used for this investigation. The selected teeth had complete root formation present with no dental fillings or sealants on their surface. After visual assessment of tooth surfaces, several impedance measurements were collected both on sound and decayed teeth on different sites of teeth surface, using the Ivium-n-Stat potentiostat (Ivium Technologies BV, Netherlands) with different probes, firstly a Ni-Cr working electrode, then, a Ni-Cr working electrode embedded with a hydrogel hemisphere. Then, data collected with the different methods were processed using the Iviumsoft software.

All impedance measurements were carried out in the frequency range from  $10^{-1}$  Hz to  $10^4$  Hz, using a sinusoidal stimulus of 10 mV, collecting 5 points per frequency decade.

Thereupon, all the teeth samples were analyzed, and successive impedance measurements were carried out on the tooth surfaces in different points of sound and decayed teeth, even in the area corresponding to a carious lesion. Finally, the frequency response of impedance magnitude and phase were recorded on the different teeth, and investigation site, and subsequently processed.

Among the different ways to represent impedance measurement, some of the most common are the Bode diagram and the Nyquist diagram. In this dissertation, the Bode diagram will be discussed. Bode plots are graphical representations of the frequency responses, where the magnitude and phase functions are reported on separate graphs using a logarithmic frequency scale along the X-axis.

In order to prove that a change in dental tissue electrical characteristics occurs in presence of a carious lesion, a first set of measurements was performed on a decayed tooth using two simple Ni-Cr wires.

The first sample was a third molar with a cavitated lesion on the enamel surface, Fig. 3.7 on the right. In particular, the measurements were collected on a sound part of

## Impedance measurements in dentistry

the tooth enamel (D1 and D2 in Fig. 3.7) and in correspondence of a carious lesion (D3 in Fig. 3.7).

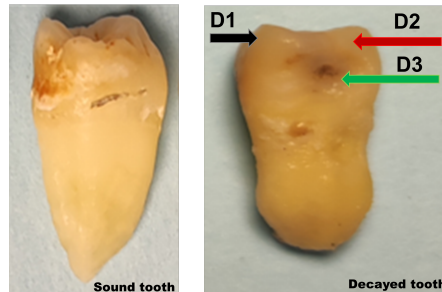


Fig. 3.7 Extracted sound tooth on the left; on the right extracted decayed tooth with a carious lesion in correspondence of green arrow D3, while D1 and D2 are sound enamel areas.

All impedance spectra collected on the tooth show a resistive behaviour at high frequencies and a capacitive-like behaviour at low frequencies. Change from resistive to capacitive-like behaviour takes place at different frequencies depending if the measurement is performed on the healthy area of the tooth (black and red line) or on a damaged (carious) area (green line) as shown in Fig. 3.8.

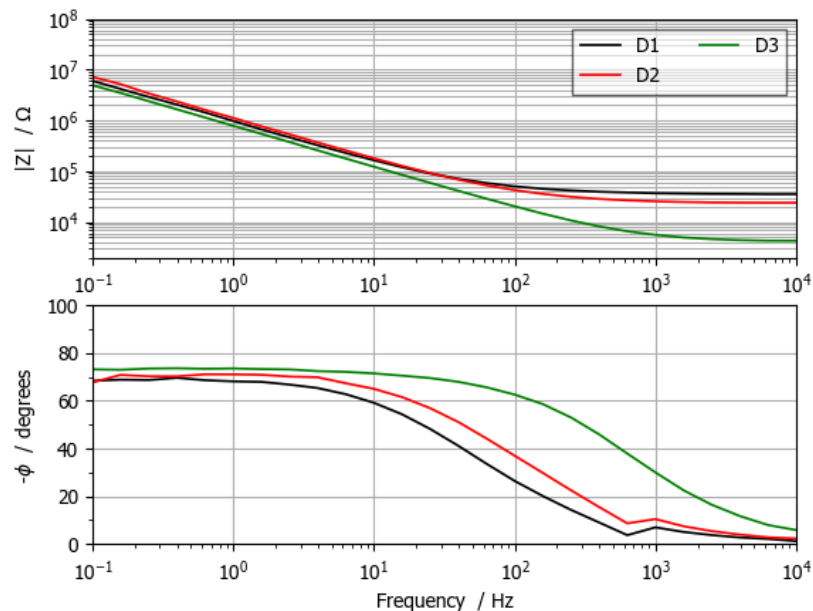


Fig. 3.8 Impedance spectra, represented as Bode diagrams, of a carious tooth. Black and red lines, respectively D1 and D2, are the spectra collected on an intact area of the tooth. The green line, i.e. D3, spectrum collected in correspondence of a carious lesion [9].

### 3.3 Carious lesion detection: Experimental procedure

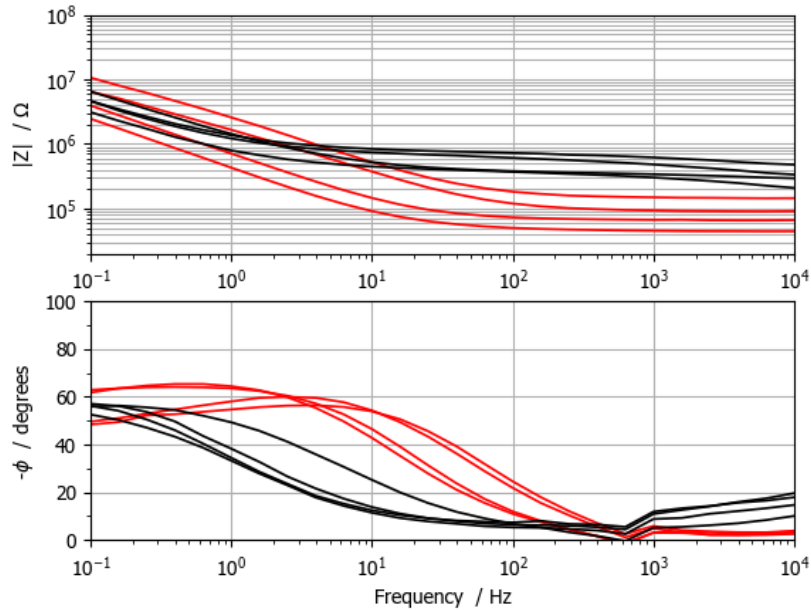


Fig. 3.9 Red lines: different measurements performed on multiple points of the same decayed tooth. Black lines: different measurements performed on multiple points of the same sound tooth [9].

This behaviour has been confirmed also when the measurements were carried out on different points of a decayed tooth and a sound one, as shown in Fig. 3.9. In particular, red lines represent multiple measurements collected on different points of the enamel surface of the same decayed tooth while black lines are multiple measurements collected on different points of the same enamel surface of a healthy tooth. In particular, these impedance spectra show as many lines as measurements made at different points on the surface. Despite all the spectra have the same shape, a difference can be noted between the sound and carious spectra. Indeed, in the case of the decayed tooth, at high frequencies, the impedance magnitude has lower values than the healthy tooth. In addition, as far as concerned the healthy tooth, the impedance phase remains at  $0^\circ$  for a higher frequency range and tends to its maximum at about  $-60^\circ$  only below 1 Hz, while the decayed tooth reaches its phase maximum at about  $-65^\circ$  at very low frequency.

## Impedance measurements in dentistry

### Hydrogel probe

In order to evaluate the performance of different probes, impedance measurements were carried out using the same setup, with a two Ni-Cr wire configuration, but the working electrode, in contact with the tooth surface, embedded with a hydrogel hemisphere of agar with a diameter of 5 mm and the counter electrode dipped in Ringer's solution. Therefore, impedance measurements were collected on different sound and decayed teeth, an example of impedance spectra is shown in Fig. 3.10, where different lines correspond to different teeth, and also using the agar probe the experiments exhibit a significant difference between sound and carious teeth.

As far as carious teeth are concerned (red lines in Fig. 3.10), the phase reaches its maximum at about  $-70^\circ$  at very low frequency and then decreases to about  $-50^\circ$  in the middle part of the spectrum. On the other side, healthy teeth reach the phase maximum at about  $-40^\circ$  and then decrease reaching values close to  $0^\circ$ . Also in this case, it can be seen lower values are measured for the impedance magnitude in decayed teeth than in sound ones. Moreover, phase values remain close to  $0^\circ$  for a longer part of the spectrum compared with measurements presented in Fig. 3.9.

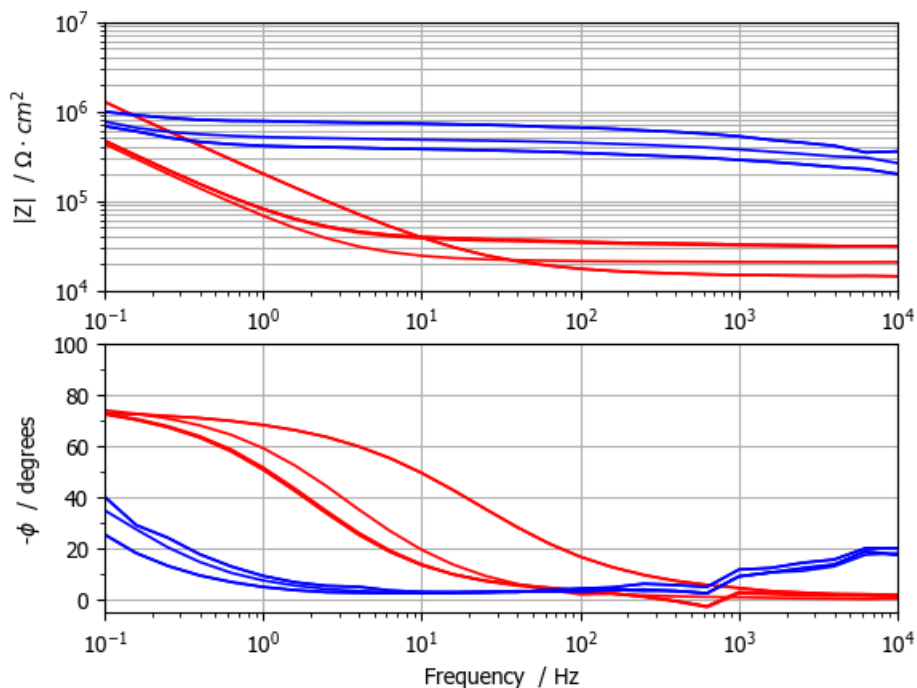


Fig. 3.10 Measurements collected using the agar probe. Red lines: measurements collected on different points of multiple decayed teeth. Blue lines: measurements collected on different points of multiple sound teeth [10].

### 3.3 Carious lesion detection: Experimental procedure

However, both using only Ni-Cr wire and the agar probe, the experiments show a significant difference between healthy and teeth with carious lesions. Nevertheless, the hydrogel probe was a too brittle material, so was not possible to perform multiple measurements without destroying the probe.

#### Frequency classification

All the examined teeth spectra without caries show a longer resistive behaviour compared to decayed teeth. Actually, the behaviour change, from resistive to capacitive-like, occurs at different frequencies depending on whether the impedance measurements are performed on sound or decayed teeth. For this reason, the frequency at which the phase reaches  $-45^\circ$  was used as a threshold value to classify sound and carious teeth.

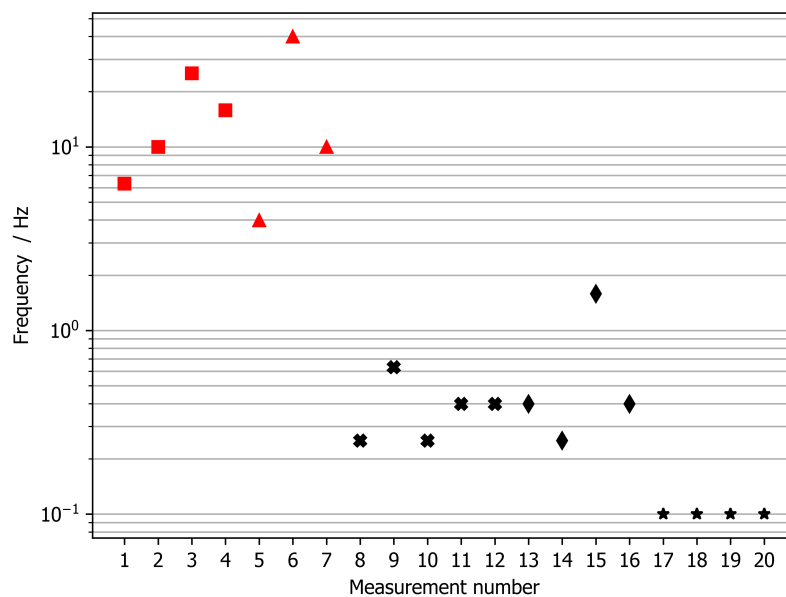


Fig. 3.11 Frequency at which the impedance phase reaches  $-45^\circ$  both for sound teeth (black icons) and carious teeth (red icons). Different markers correspond to different teeth [9].

Fig. 3.11 reports the frequency value at which the phase reaches  $-45^\circ$  for different carious (red markers) and sound teeth (black markers). As can be noticed in Fig. 3.11, this parameter is able to discriminate samples in two different clusters. Carious teeth, represented by red markings, group in the upper part of the graph, as

## Impedance measurements in dentistry

---

they reach the  $-45^\circ$  value for the phase at higher frequencies. Conversely, sound teeth are in the lower part of the plot, since they are characterized by a resistive behaviour in a wider frequency range and some samples (e.g., the ones represented by stars in Fig. 3.11), do not even reach a phase value of  $-45^\circ$ , and for these samples, the minimum measured frequency is shown.

The measured impedance values are not normalized, since in the case of in-vivo applications it is not always possible to measure the area of the analyzed samples. To overcome this intrinsic limitation of the measurement, the discrimination of healthy teeth from decayed teeth is done by analyzing the phase trend instead of the impedance modulus. In fact, the phase is not dependent on the surface of the sample, but only on its dielectric properties.

Consequently, impedance spectroscopy can be exploited to detect a variation in dental tissue electrical characteristics when a carious lesion occurs, hence to monitor sound teeth and carious lesions considering a shift from the resistive behaviour to the capacitive-like which happens at different frequencies if the measurement is collected on the sound tooth or on the decayed tooth.

### 3.3.2 Equivalent Electrical Circuit

The interest in modeling complex biomedical phenomena has increased considerably in recent decades. One of the application areas is modeling the electrical impedance of biological tissues, also known as tissue bioimpedance. Above all, equivalent circuit networks with different topologies can emulate the electrical impedance characteristics of dental tissues [166]. A broad range of electrical equivalent models have been adopted for a wide range of dental applications, such as a model with a single CPE in parallel with a series connection of CPE, and a resistor was used to accurately measure a tooth root canal length by means of the apex locators, an electronic device that uses electrical impedance measurements [167]. The constant phase element (CPE) is a capacitive impedance often used during electrochemical EIS analysis instead of a pure capacitor since it reflects the real electrical behaviour of the solid/liquid interface [168].

Other studies are searching for equivalent electrical circuit parameters that fit EIS data for their correlation with dental caries. These models often incorporate CPEs, used to describe the impedance characteristics of dental tissue. Specifically, a model



### 3.3 Carious lesion detection: Experimental procedure

with a single CPE, two resistors, and two capacitors provide measurements of tooth enamel [169]; while to represent dentin measurements a four-element circuit with three-series resistors in parallel with a CPE is used in [170].

An active area of EIS is focused on the determination of the most appropriate circuit models for different applications. One of the main goals is to adopt a model that has the least number of parameters but can properly emulate the structure of the studied tissue by fitting impedance elements and that model parameters have a chemical and physical interpretation inside the system.

Another in-vitro study [171] proposes an electrical circuit composed of a resistor  $R_s$  in series with parallel resistor  $R_p$  and a constant phase element (CPE), to evaluate the diagnostic performance of impedance spectroscopy technique in detecting questionable occlusal carious lesions. A fractional electrical model was proposed to predict the current response to a step voltage excitation in the time domain.

To further analyze the results of the impedance measurements previously obtained, the spectra were modeled using a suitable equivalent electric circuit.

"The proposed equivalent circuit, reported in Fig. 3.12, consists of a resistor connected to a constant phase element (CPE) in parallel with a second resistor. Indeed, the first resistor is composed of two contributions: the former ( $R_s$  in Fig. 3.12) related to solution resistance and the latter (named  $R_1$ ) related to the interface resistance between the Ni-Cr wire and the tooth. In the second part of the circuit,  $Q_1$  is the double layer capacitance (modeled as a CPE) and  $R_2$  is the charge transfer resistance, which is correlated to the porous structure of the tooth due to the caries formation and electrical parameters associated to the enamel and dentin structure [172][166]. The measured impedance spectra were fitted using the IviumSoft software (release 4.982)." [9] Results from equivalent electrical circuit modeling are reported in Tab.

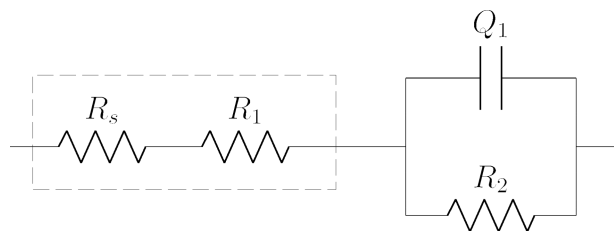


Fig. 3.12 Equivalent electrical circuit that models impedance spectra collected on sound and demineralized teeth [9].

3.2, which shows measurements performed on a decayed tooth in the carious lesion, namely D3, and on different points of the tooth crown, D1 and D2. It can be

## Impedance measurements in dentistry

---

observed that a variation in  $R_1$  is present, as this parameter has a lower value in correspondence of the carious lesion. Moreover, the CPE was considered instead of an inductor, in order to take into account the surface inhomogeneity, thus an increase in  $Q_1$  parameter is present when the carious lesion is analyzed. It is worth noticing that no significant variations are present in the  $R_2$  values, because the impedance measurements did not explore very low frequency otherwise the measurement time would last too long.

Table 3.2 Equivalent electrical circuit parameters computed for a tooth with carious lesion, where D3 is the area with carious lesion (results coming from the spectra reported in Fig. 3.8)

	$R_s$	$R_1$	$Q_1$	$N_1$	$R_2$
	Value [ $\Omega$ ]	Value [ $\Omega$ ]	Value [ $s^N/\Omega$ ]	Value	Value [ $\Omega$ ]
D3	10	$4.03 \cdot 10^3$	$2.87 \cdot 10^{-7}$	$8.11 \cdot 10^{-1}$	$4.71 \cdot 10^7$
D1	10	$3.59 \cdot 10^4$	$2.40 \cdot 10^{-7}$	$8.00 \cdot 10^{-1}$	$8.64 \cdot 10^7$
D2	10	$2.42 \cdot 10^4$	$2.02 \cdot 10^{-7}$	$8.09 \cdot 10^{-1}$	$1.03 \cdot 10^7$

Those results proved that devices based on electrical current measurement can be employed for the early stage enamel demineralization detection due to the porosity changes of this layer.

### 3.4 Demineralization: Experimental procedure

The problem of demineralization focuses the interest of many dentists and scientists since if the phenomenon continues over time, or is not treated, it can lead to the formation of carious lesions. Therefore, demineralization process are simulated and studied in controlled environment. For this study, fifty human undamaged front incisors, extracted due to parodontic reasons, were collected. All the teeth were collected with informed consent in the Department of Cariology and Operative Dentistry, University of Turin (Italy). The ethical committee of the University of Turin approved the study protocol (DS 00071 2018).

All the teeth were carefully selected to obtain samples lacking any defects like cemento-enamel defects or dental caries that could affect the results of the study.

### 3.4 Demineralization: Experimental procedure

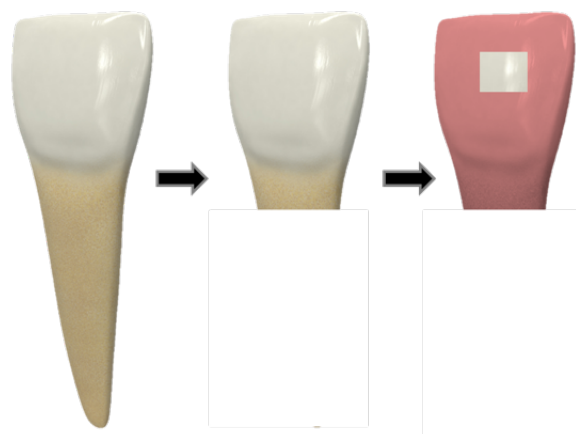


Fig. 3.13 Lower central incisor cut and covered with the protective coating but a selected window.

Moreover, the selected teeth had complete root formation present with no dental fillings or sealants on their surface, or evident cracks. After extraction, the teeth were cleaned, disinfected and soft tissue debris and bone fragments were removed. Then, they were stored in hermetically sealed vials containing 0.5% w/v sodium hypochlorite (NaClO) solution at 4 °C, in order to avoid dehydration. In order to limit inter- and intra-variability, due to several factors, including teeth age, and the extraction from different patients, only frontal incisors were used for this study. Each tooth was sectioned, and the anatomical root was cut with a low-speed diamond saw under constant water irrigation. All samples were cleaned and dried with an airflow, and then a selected window of 3 mm x 3 mm on the enamel surface was isolated, while the rest of the tooth surface was covered with a protective organic coating. Since the tooth surface is not homogeneous, a great difference in the number, distribution, and shape of dental tubes can be experienced according to the area of interested on the tooth, a limited area was selected. Moreover, the selected window was placed in correspondence of the central section of the third medium of coronal vestibular face, in order to have a surface as flat as possible that facilitate further SEM and Raman analysis. An example of lower central incisors cut and then covered with the protective coating is shown in Fig. 3.13.

Each sample was immersed in a specially prepared demineralization solution and incubated at 38 °C for 96 h without stirring. After the demineralization period, all the teeth were flushed with distilled water and stored in sealed vials containing distilled water and stored at room temperature.

## Impedance measurements in dentistry

---

The demineralization protocol was validated in the previous study [173]. The demineralizing solution was prepared following the procedure described below with the following components:

- distilled water;
- 0.05 mol/L of acetic acid ( $CH_3COOH$ );
- 1.28 mmol/L of calcium chloride ( $CaCl_2$ );
- 0.74 mmol/L of potassium dihydrogen phosphate ( $KH_2PO_4$ );
- sodium hydroxide (NaOH) or hydrochloric acid (HCl) to regulate pH.

Once the solution was prepared, it was buffered with sodium hydroxide or hydrochloric acid till to reach the required 5 pH.

All the measurements: impedance, SEM, and Raman, were performed before demineralization and immediately after taking out the samples from the solution in order to monitor any change in tooth structure.

### 3.4.1 Raman Spectroscopy

To diagnose, but above all to classify demineralizing lesions clinically, indices based on the visual examination of the surfaces of the teeth are used. The index score is assigned based on the extension, severity, and location of the lesion. Instrumental investigations are not generally used to diagnose demineralization, rather visual analysis is the standard procedure. However, anamnesis and physical examination may have limitations due both to the operator and to the difficulty of identifying a demineralization process at its beginning stage. Thus, in order to evaluate the state of demineralization, especially in the experimental field, instrumental diagnostic techniques are used, the latter allows the dental tissues to be characterized more objectively. Among these, Raman spectroscopy and the scanning electron microscope (SEM) are employed in this dissertation section.

Raman spectroscopy is a spectroscopic technique able to deliver information on the structure and chemical composition of materials under test within a very short time and with high resolution. This method is used to detect vibrational, rotational,

### 3.4 Demineralization: Experimental procedure

---

and other states in a molecular system. Raman spectroscopy is a simple, non-destructive technique where samples are analyzed directly without any or minimal surface pretreatment, which produces reproducible results.

Raman spectroscopy has gained popularity in biomedical research thanks to its versatility, minimal invasiveness, non-destructiveness, poor sensitivity to the state or shape of the examined specimen or material, but at the same time a high sensitivity to chemical, morphological, and structural change in specimen or material under test, capability to work on tissues both dry and in solution making it suitable to the physiological condition and to the in-vivo potential application by means of fiber-optics. This powerful and fast technique provides chemical composition and structural arrangement of different molecules and the morphology and crystal orientation of minerals, thus, it is particularly suitable to acquire accurate spectroscopic information on inorganic tissues, i.e. teeth, mainly composed of phosphate and carbonate, by studying the vibration modes and their characteristic energy associated to the presence of minerals [174]. Raman spectroscopy can also be applied in-vivo, for real-time measurements on different types of samples in different areas and on very small sizes, less than 1  $\mu\text{m}$ .

Every chemical element, compound, or sample has its own specific Raman spectrum, which is the result of the excitation and vibrational mode of a particular molecule; complex or mixed samples have a resulting spectrum made by a superposition of the Raman signals from each of their components. By analyzing the band of every component is possible to perform a quantitative analysis of relative biochemical composition and morphological structure [175]. Usually, Raman spectroscopic measurement involves a laser beam focused on the analyzed sample and the recording of the energy profile associated to the scattered light.

#### **Raman spectroscopy in dentistry**

Different important spectral parameters can be extracted by the Raman spectrum and they can be used to characterize the sample, considering molecular structure, the biochemical composition, as well as the structural arrangement and orientation.

Raman spectroscopy is an accurate and suitable tool for oral hard and soft tissue assessment, differentiation, and classification. Among the various applications of this technique in the biomedical field, it is widely used in dentistry, for example, to evaluate bleaching agents' performance by assessing the alteration in phosphate

## Impedance measurements in dentistry

---

concentrations of surface enamel, to evaluate the demineralizing effect from pharmaceutical products, low pH foods, and drinks with erosive potential [176] [177] [178], to calculate the degree of conversion of polymeric materials, such as resins and cements used in restorative dentistry [179]. Indeed, the degree of conversion of polymeric materials is calculated on the basis of the variation in the intensity of specific vibrational modes. In particular, the technique makes it possible to monitor the change in the peaks relating to the C=C double bonds which are converted into C-C single bonds with the [180] polymerization process.

In a similar way, the technique can be used to monitor the vibrational modes linked to hydroxyapatite,  $Ca_{10}(PO_4)_6(OH)_2$ , which is one of the main components of dental enamel and whose demineralization it is linked to the carious process. The width of this vibrational band in the Raman spectrum can also be directly related to the level of crystallinity degree of this mineral phase, and to the number of defects, impurities, and contaminants, present in the hydroxyapatite crystals [181]. Monitoring this mineral phase becomes important if the morphology and structure of a tooth are taken into consideration since it allows not only study the demineralization of the tooth surface, but also to capture the differences between dental caries and sound tooth tissues, and between oral cancer lesions and healthy tissue.

Moreover, Raman peak intensity gives information about the polarizability factor of the chemical bond and material relative concentration and distribution. In order for a vibrational mode to be Raman active, the polarizability must change during the vibration. For instance, in dental enamel or dentin, the amplitude of the phosphate peak is directly connected to the mineral content [174]. As a matter of fact, the Raman spectrum acquired on the tooth, which can be observed in Fig. 3.14, has an intense peak at  $960\text{ cm}^{-1}$ , which is characteristic of the group phosphate  $PO_4^{3-}$ , and whose intensity decreases with increasing demineralization.

Other useful parameters to evaluate the demineralization state of the enamel surface are the Crystallinity, and the gradient in mineral content (GMC), also known as carbonate-to-phosphate ratio (C/P).

Crystallinity (C) is calculated as the inverse of the full width at half maximum (FWHM) of the band centered at  $960\text{ cm}^{-1}$ . It is correlated to the order degree within the minerals, a particular component of HA, because a structural change may occur during ion substitution due to demineralization. Therefore, a wide band indicates a low mineral crystallinity and vice versa.

The carbonate-to-phosphate ratio (C/P) represents the amount of carbonate incorpo-

### 3.4 Demineralization: Experimental procedure

ration in the HA lattice. Two main kind of substitution may arise. *Type – A* when the carbonate replaces the hydroxide; and the *type – B* when  $PCO_3^{2-}$  ions (impurity) occupy the  $PO_4^{3-}$  sites of the HA crystal lattice. During the demineralization process, a progressive increase of C/P happens, due to the substitution of  $CO_3^{2-}$  for  $PO_4^{3-}$  in HA (*type – B* substitution) [182][183]. Indeed carbonated HA has a lower hardness, is less stable, and it is more acid-soluble than non-carbonated HA [184].

Therefore, the C/P is assessed as the ratio between the intensities of the bands centered at  $1070\text{ cm}^{-1}$  and  $960\text{ cm}^{-1}$  which are respectively associated with the carbonate and phosphate groups in HA. In this dissertation, the aforementioned parameter will be calculated.

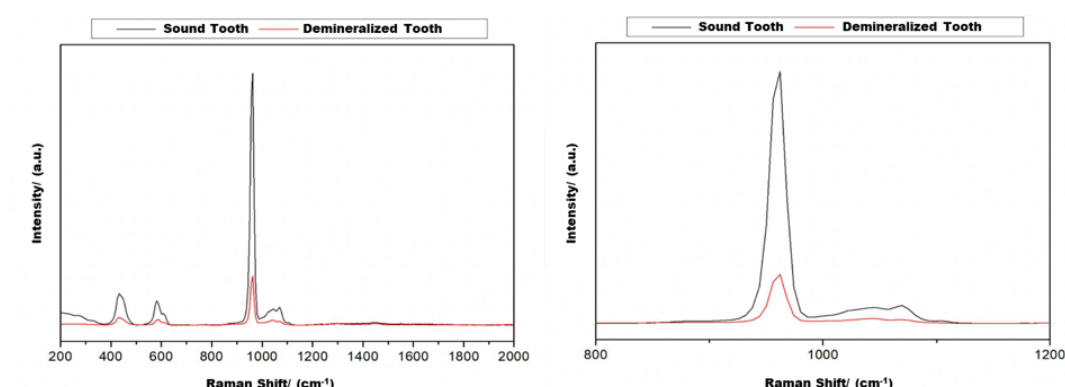


Fig. 3.14 Representative Raman spectra collected on one healthy and one demineralized tooth. On the left the spectra in the range  $200\text{ cm}^{-1}$ - $2000\text{ cm}^{-1}$ , while on the right an enlarged section is shown, in the range  $800\text{ cm}^{-1}$ - $1200\text{ cm}^{-1}$ .

#### Experimental setup

Raman spectroscopy measurements were performed by means of a portable modular spectrometer manufactured by BWTEK, performing the analyses directly on the tooth surface. The instrument, shown in Fig. 3.15, is equipped with a monochromatic laser ( $\lambda$ :  $1064\text{ nm}$ ) and a spectrometer BTC284N (measurement range: from  $100\text{ cm}^{-1}$  to  $2500\text{ cm}^{-1}$ , resolution equal to  $10.56\text{ cm}^{-1}$ ) coupled with a CCD sensor. The analysis was carried out by connecting the instrument to a compact microscope (BAC151) which allows one to observe the area under analysis and to focus the beam on the surface.

A typical Raman spectrum acquired on an enamel surface is shown in Fig. 3.16, with an indication of the peaks considered for the following data elaboration.

## Impedance measurements in dentistry

In particular, the bands  $965\text{ cm}^{-1}$  and  $1075\text{ cm}^{-1}$ , corresponding to phosphate and carbonate ions respectively, where the most significant differences between demineralized and sound teeth are manifested.

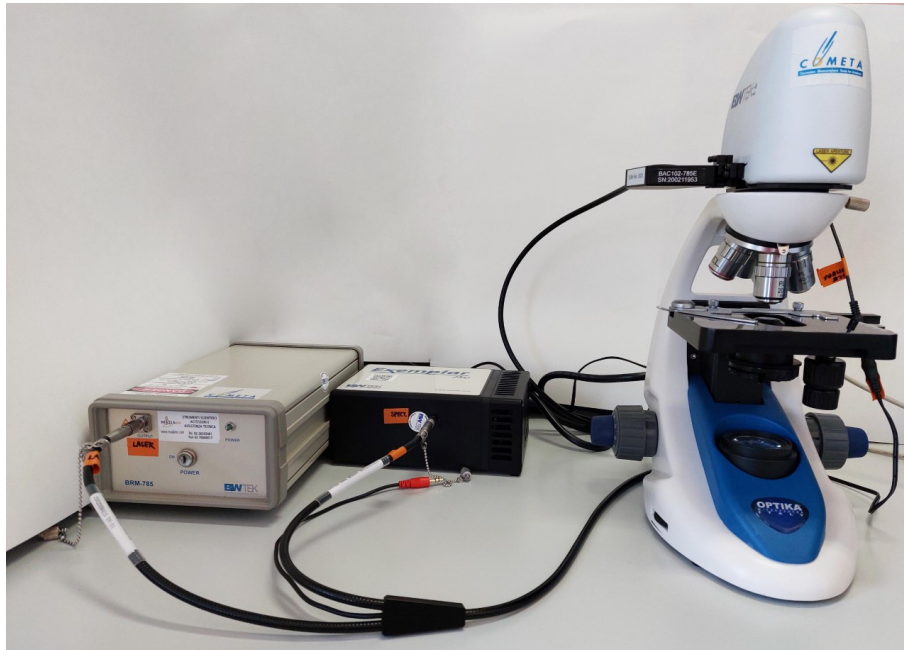


Fig. 3.15 Portable modular spectrometer by BWTEK used to perform Raman analysis.

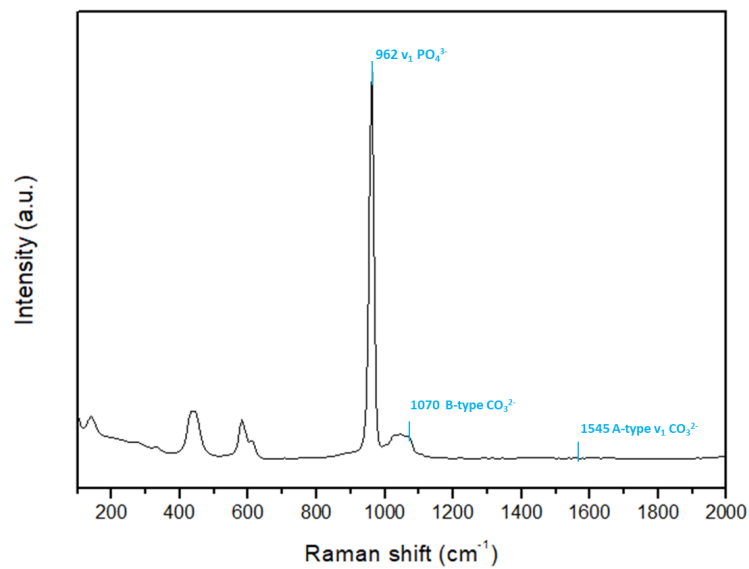


Fig. 3.16 Raman spectra of enamel, with the corresponding vibrational modes ( $\nu$ : stretching vibration) of the peaks considered for data elaboration.



### 3.4 Demineralization: Experimental procedure

---

Since the main goal was to evaluate the intensity of the band at  $\sim 960\text{ cm}^{-1}$  and  $\sim 1075\text{ cm}^{-1}$ , the spectral range between  $400\text{ cm}^{-1}$  and  $1800\text{ cm}^{-1}$  was investigated.

The following parameters were employed: laser power of 225 mW, integration time of 40 s, 12 repetitions for each area, microscopic objective of 80 $\times$  (analysed area of about 20  $\mu\text{m}$ ). For each sample, 3 measurements on three different points of the enamel surface were collected, before and after the demineralization procedure. Raman spectra can be seriously affected by noise and interference. Moreover, they can have a limited resolution. It is therefore mandatory to process the spectra before using it for detecting elements and compounds. With this aim, python software was developed to process the Raman spectra effectively in a batch mode. Provided to have a set of Raman spectra in the input folder the script is able to produce in the output folder the fitted spectra together with the fitting parameters. The script operates in three sequential steps. The user first defines the interval of interest and the spectra are trimmed at this interval. In the second step, the software processes the spectra removing the baseline (noise and interference). The software can detect the baseline using several algorithms, but the most effective is the Asymmetric Least Squares Smoothing [185]. A standard normal variate (SVN) transformation was applied. This method allows to normalize the spectra by subtracting from the spectra its mean value and dividing it by its standard deviation. [186].

After the baseline was removed the user can define the number and the position of the peaks and the required shape (either Gaussian or Lorentzian) of interest. At this point, the software, starting from the defined peaks processes the spectra by performing a non-linear fitting based on an incremental least-square optimization algorithm so that the error between the sum of all fitted base peaks and the original spectrum is the minimum possible. At the end of the fitting, the software returns the fitted spectra as the sum of the fitted peaks and the parameters of each peak (such as center, amplitude, width, etc., according to the fitting shape). The software is also able to calculate specific parameters which can be useful to better analyze the data. An example of spectrum processing is shown in Fig. 3.17.

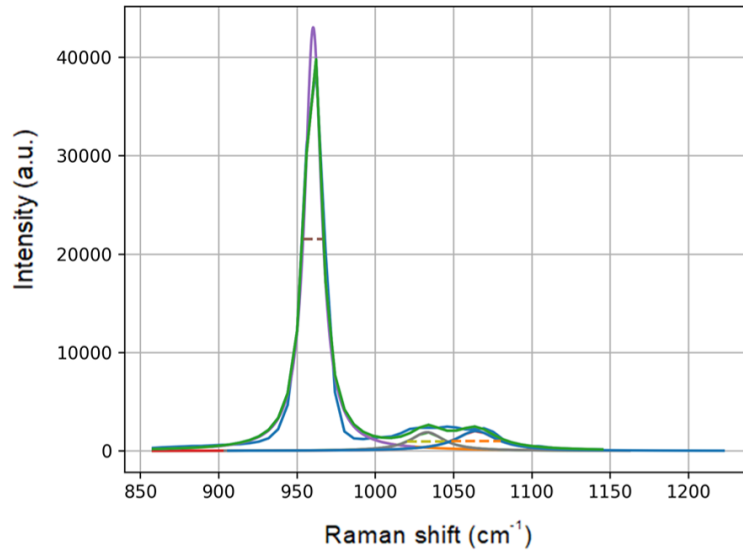


Fig. 3.17 Example of a spectrum processing with a Lorentzian fitting.

In particular, for each spectrum, different parameters, related to the demineralization phenomenon, were assessed, such as the intensity and the area, by integrating the area under the most significant bands, the full width at half maximum of a single band (FWHM). For each sample, three different spectra before and after the demineralization procedure, on three different points of the enamel surface, were collected. In this dissertation, the analyzed parameters are: Phosphate peak intensity  $I_{960}$ ; crystallinity, which is inversely proportional to FWHM<sub>960</sub>; and Gradient in Mineral Content (GMC), also known as carbonate-to-phosphate ratio (C/P), calculated as the intensity ratio:  $I_{1070} / I_{960}$  [183]. For each sample, the average value and the corresponding standard deviation were assessed, before and post demineralization.

### Results

The intensity of  $PO_4^{3-}$  band ( $\sim 960 \text{ cm}^{-1}$ ), calculated as the height of the corresponding peak, represents the mineral content of the HA crystal lattice, and its decrease is mainly attributed to demineralization-induced alterations of enamel. Indeed, the histogram in Fig. 3.18 shows a decrease of the intensity peak at  $960 \text{ cm}^{-1}$  for the teeth that experienced the demineralization (red bars).

### 3.4 Demineralization: Experimental procedure

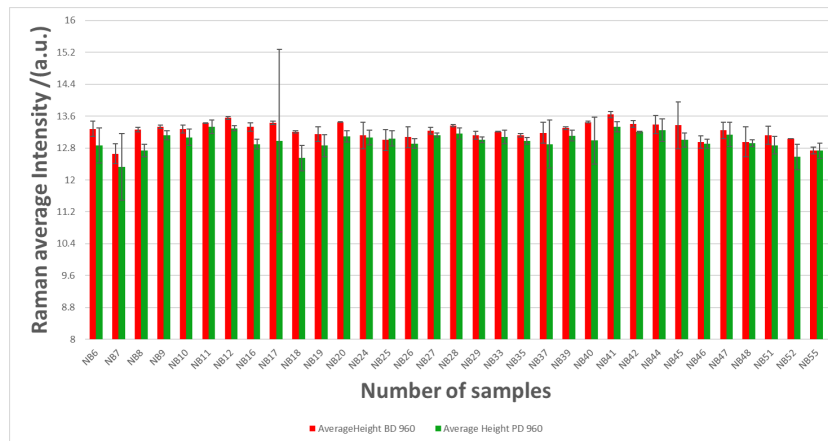


Fig. 3.18 Average intensity peak at  $960\text{ cm}^{-1}$  of different samples before (red) and post demineralization (red).

The distribution of different parameters evaluated before and after demineralization is shown in Fig. 3.19 box plot. The results from data acquired before demineralization are reported in red, while the ones post-demineralization are shown in green. The minimum and the maximum values are represented by a horizontal line, the median is shown by the line that divides the box into two parts, and the mean value is the square in the middle of the box. The upper line of the box is the upper quartile, it indicates that 75% of the data fall below the upper quartile. On the other hand, the lower quartile, that is the bottom line of the box, represents the 25% of data that fall below the lower quartile. Finally,  $\times$  represents the 99% and 1% percentile. In this case, the box plot is comparatively short, this suggests that overall teeth of the same group a high level of agreement with each other.

## Impedance measurements in dentistry

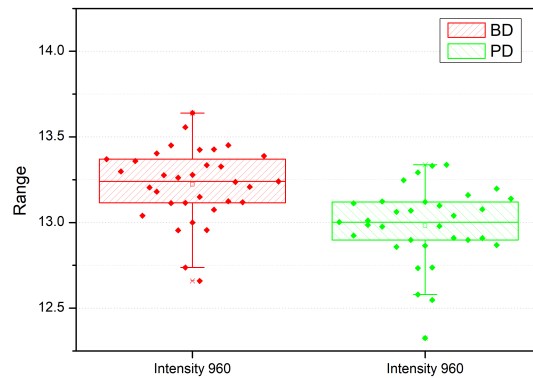


Fig. 3.19 Box plot of average intensity peak at  $960\text{ cm}^{-1}$  of different samples before (green) and after demineralization (red).

Similarly as for the peak at  $960\text{ cm}^{-1}$ , a significant change in values of the full width at half maximum (FWHM) and the area can be observed in the samples after demineralization. In particular a decrease of those parameters can be observed in Fig. 3.20, since lowering the peak causes an increase in the area under examination that is less narrow.

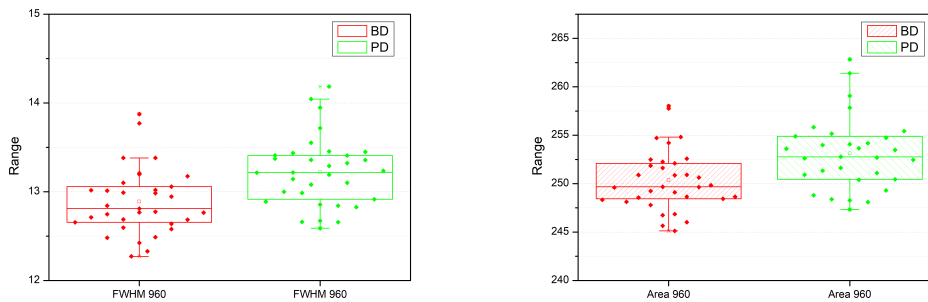


Fig. 3.20 On the left: Box plot of Average FWHM at  $960\text{ cm}^{-1}$ ; on the right: Box plot of Average Area at  $960\text{ cm}^{-1}$ , for both red are teeth before the demineralization, while green teeth post demineralization. The horizontal lines are the minimum and the maximum values, the median is the line that divides the box into two parts, and the square in the middle of the box is the mean value. The upper line of the box is the upper quartile, it indicates that 75% of the data fall below the upper quartile. The bottom line of the box is the lower quartile, it represents the 25% of data that fall below the lower quartile.  $\times$  represents the 99% and 1% percentile.

### 3.4 Demineralization: Experimental procedure

The results of these analyses show that the demineralized enamel had more stoichiometric imperfections in the mineral crystal lattice than the sound enamel. Indeed, a higher degree of mineralization with higher crystallinity and lattice perfection in the sound enamel tissue can be observed. Thus the sound teeth, namely before the demineralization (red blocks), present the highest values compared to the demineralized ones (green blocks) of Fig. 3.21. The corresponding box plot is shown in Fig.3.22

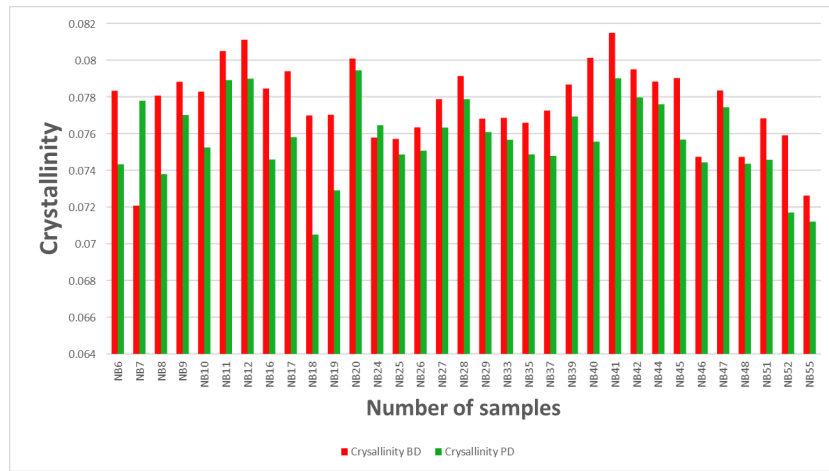


Fig. 3.21 Average crystallinity before (red) and post demineralization (green) of different samples.

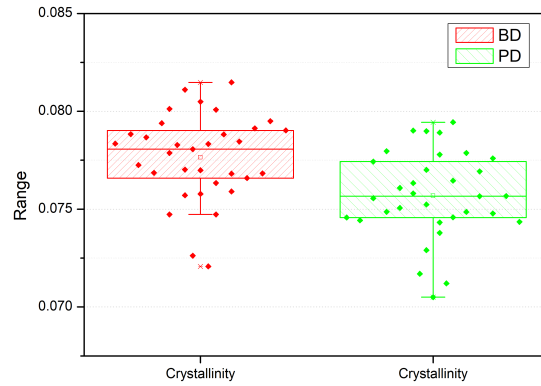


Fig. 3.22 Box plot of Average intensity Crystallinity of different samples before (green) and after demineralization (red). The horizontal lines are the minimum and the maximum values, the median is the line that divides the box into two parts, and the square in the middle of the box is the mean value. The upper line of the box is the upper quartile, it indicates that 75% of the data fall below the upper quartile. The bottom line of the box is the lower quartile, it represents the 25% of data that fall below the lower quartile.  $\times$  represents the 99% and 1% percentile.

Moreover, the Demineralization Degree (DD) was assessed, and the results shown in Fig. 3.23 The DD was calculated as follows:

$$DD\% = \left(1 - \frac{I_{960_{PD}}}{I_{960_{BD}}}\right) * 100 \quad (3.1)$$

where  $I_{960_{BD}}$  and  $I_{960_{PD}}$  are the intensity of the vibration modes at  $960\text{cm}^{-1}$  before and post demineralization respectively. Fig. 3.23 show that the DD is not the same for all the samples, indeed as confirmed also by SEM images, some teeth were more demineralized than others.

Moreover, it is possible to graphically observe the decrease of crystallinity in relation to the demineralization, as shown in Fig. 3.24.

### 3.4 Demineralization: Experimental procedure

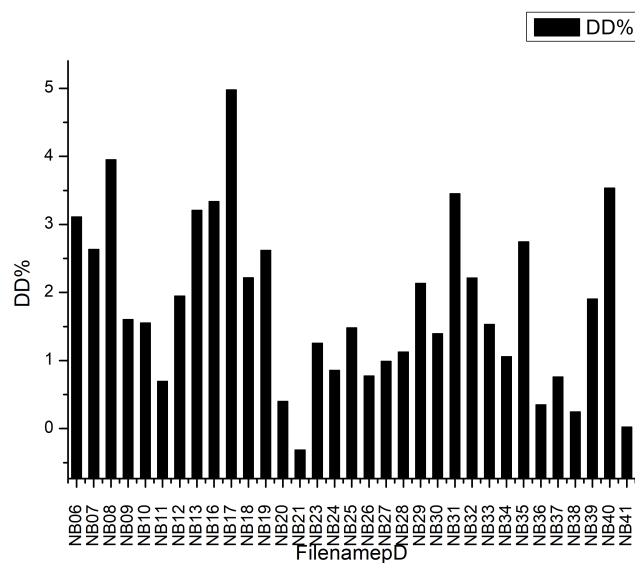


Fig. 3.23 Demineralization Degree.

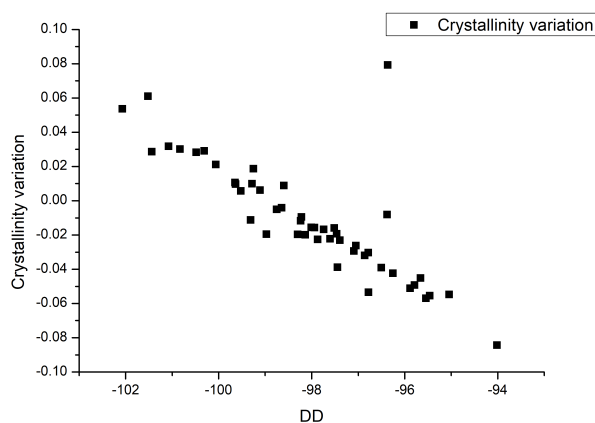


Fig. 3.24 Crystallinity variation according to the Demineralization Degree.

The crystallinity was evaluated also directly in relation to the Intensity of the peak at  $960\text{cm}^{-1}$ . The result, before (red dots) and after demineralization (green dots) is shown in Fig. 3.25.

## Impedance measurements in dentistry

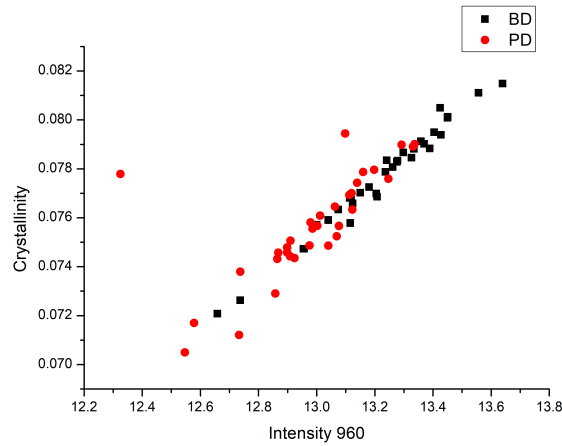


Fig. 3.25 Crystallinity variation according to the intensity peak at  $960\text{cm}^{-1}$ .

On the other hand, the carbonate-to-phosphate ratio (C/P), assessed as the ratio between the intensities of the bands centered at  $1070\text{cm}^{-1}$  and  $960\text{cm}^{-1}$ , did not show a trend that could be correlate to the demineralization.

It is possible to observe that for the measured samples the C/P value (Fig. 3.26) does not increase in all samples. This may be a consequence of different causes; firstly, the demineralization is not uniformly distributed on the surface of the enamel analyzed and the analysis area is only  $20\ \mu\text{m}$ , furthermore the measured point may experience a different type of substitution, i.e. Type-A. Then, it is worth reminding that, human teeth have high inter-subject variability, teeth can demineralize in different ways due to numerous physiological factors that are difficult to account for.

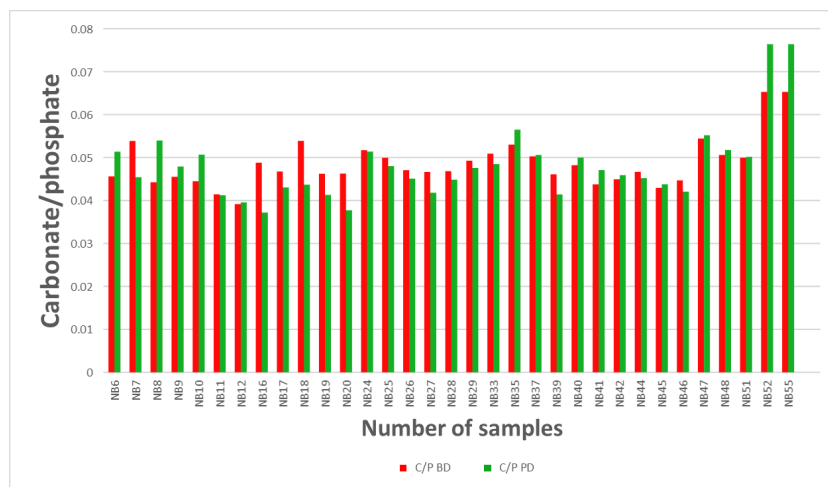


Fig. 3.26 Carbonate Phosphate ratio Before (red) and Post demineralization (green).



### 3.4 Demineralization: Experimental procedure

---

However, the results presented below confirm that Raman spectroscopy coupled to impedance spectroscopy allows to correlate the current response with information of a chemical type, thus obtaining a complete picture of the state of health of the tooth.

#### 3.4.2 Scanning Electron Microscopy (SEM)

Scanning electron microscope (SEM) is one of the most used methods for imaging the morphology and microstructure of solid materials at high magnifications. The SEM is a kind of electron microscope that produces images of a sample by scanning it with a focused electron beam with a low energy electron beam. The SEM method consists of electrons accelerated to energy levels of typically 0.1-30 keV by the electron gun located on the top of the column. A high-vacuum chamber allows electrons to move without being scattered or absorbed by the air. Finally, the electrons reflected from the sample are collected by the detector. The resulting image is the representation of the interaction of electrons and the sample elements.

By and large, the observed sample should have a conductive surface in order to be analyzed by SEM. Therefore, to observe non-conductive samples they need to be covered with a thin layer of conductive material such as gold or silver. Moreover, is a subjective and qualitative method that is generally considered a destructive analysis because once the sample is coated with gold, it cannot be used for further analyses.

However, when the vacuum conditions are not extreme, is possible to observe a sample with a low conductivity without a metallization pretreatment [161]. Within this framework, SEM finds application in teeth study since no gold and/or silver coating pretreatments are required. Thus, it is employed to study enamel morphology, and its changes after erosion or different treatments, e.g. bleaching, demineralization, and remineralization [187].

This method is rather simple to perform, although is highly operator dependent; indeed qualified and skilled technicians are needed. In addition, when SEM is used the vacuum condition and dehydration of biological samples may negatively affect the teeth samples.

In this study for the morphological characterization of the demineralized teeth, the Phenom™ XL G2 Desktop SEM (Thermo Fisher Scientific) was used. Teeth were introduced into the microscope without previous metallization or any surface of

## Impedance measurements in dentistry

---

dehydration treatment, under controlled humidity and room temperature. The samples were carefully cleaned in order to eliminate any spare material on the surface/the impurities on the surface of the specimen, which could alter SEM observation.

SEM images were acquired in low vacuum conditions with an acceleration voltage of 15 kV working at a distance of about 8.5 mm, two times: before the demineralization process and after the 96 h demineralization process. An example is shown in Fig. 3.27, on the left a healthy enamel with a smooth surface with some pits, impurities, and scratches. On the right of Fig. 3.27 the enamel surface, after the demineralization procedure, presents the loss of enamel prism core but retained periphery and hexagonal structures, with an alveolar appearance typical of exposed HA crystals.

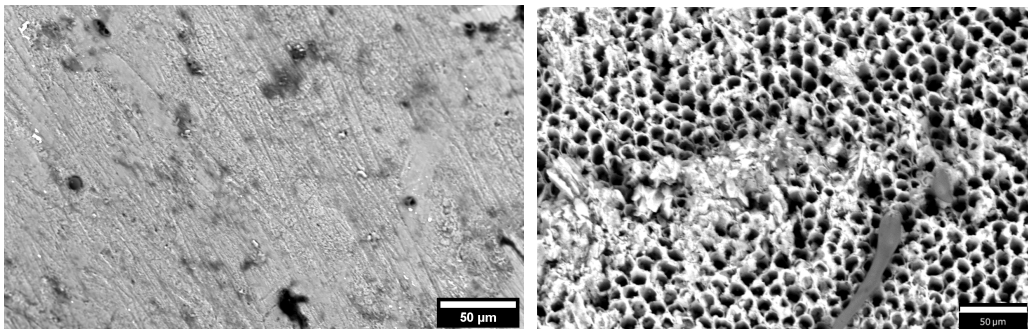


Fig. 3.27 Scanning electron microscope (SEM) images of healthy enamel on the left and demineralized enamel surface on the right.

### 3.4.3 Impedance Measurements and Data Acquisition

The main aim of this section is to prove that, in presence of a demineralized area, a change of the electrical characteristic of dental tissue occurs, allowing thus to discriminate between healthy teeth and demineralized ones.

For this purpose, two sets of measurements were collected on fifty teeth: the first one on the teeth before the demineralization procedure, the second on the same teeth but after 96 h of immersion in demineralization solution.

"In order to ensure an appropriate measurement procedure without any tooth damage, a 3D-printed PLA holder was specifically designed in order to fix the tooth sample inside the measurement cell." [11]. The measurement setup was the same shown in Fig. 3.6.

"The sample was soaked in a physiological saline solution (0.9% w/v sodium chloride, NaCl, solution) to avoid dehydration and guarantee good sample visibility during

### 3.4 Demineralization: Experimental procedure

the measurement. The impedance measurements were performed using an Ivium-n-Stat potentiostat (Ivium Technologies BV, Netherlands), with a two-electrode configuration that includes two platinum electrodes with a diameter of  $0.1\text{mm}$ . The working electrode was positioned on the selected polish-free section of the central dental crown, while the counter electrode was dipped into the physiological saline solution. Impedance measurements were acquired using a sinusoidal stimulus of  $10\text{ mV}$ , in the frequency range from  $10^{-1}\text{ Hz}$  to  $10^4\text{ Hz}$ , collecting 5 points per frequency decade." [11]

Different impedance measurements on different points were collected on the selected enamel area. The frequency response, of all the teeth, of impedance magnitude and phase were recorded, processed with Ivium software and then compared by mean of Python scripts.

Some examples of three teeth, with impedance measurements collected before and after demineralization, are shown in Fig. 3.28, Fig. 3.29, and Fig.3.30.

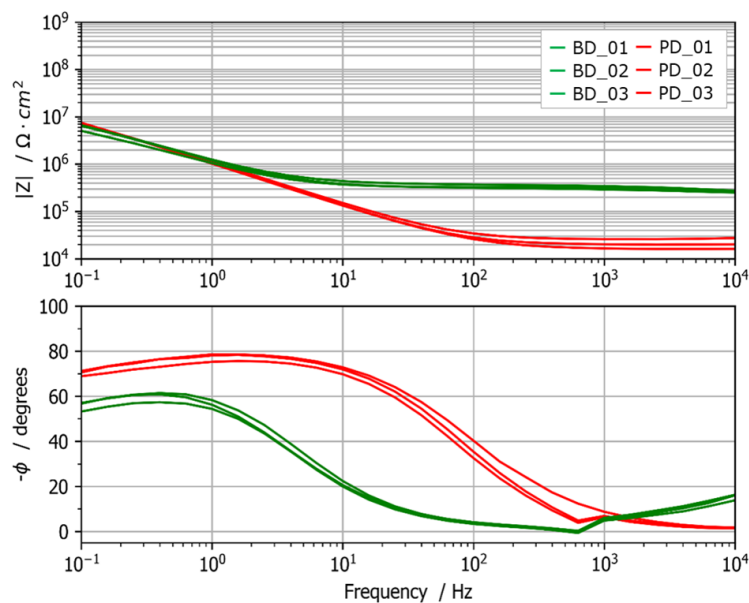


Fig. 3.28 Impedance spectra collected on a demineralized tooth. Spectra were collected on three different areas on the tooth surface, before and after demineralization. A phase shift of about one decade due to demineralization is clearly visible.

Different points on the same tooth correspond to different lines. As a matter of fact, all spectra show resistive behaviour at high frequencies which becomes a

## Impedance measurements in dentistry

capacitive-like approaching lower frequencies. The capacitive behaviour, at low frequencies, is related to double-layer capacitance established at the interface between the tooth surface and the electrode probe. While, at higher frequencies, the resistive behaviour is due to the solution resistance and, in a certain extent, to the tooth interface.

An example of impedance spectra collected on a tooth that experienced the demineralization is shown in Fig. 3.28, while spectra that, despite being subject to the same demineralization treatment, didn't show any change on the enamel surface are shown in Fig. 3.29.

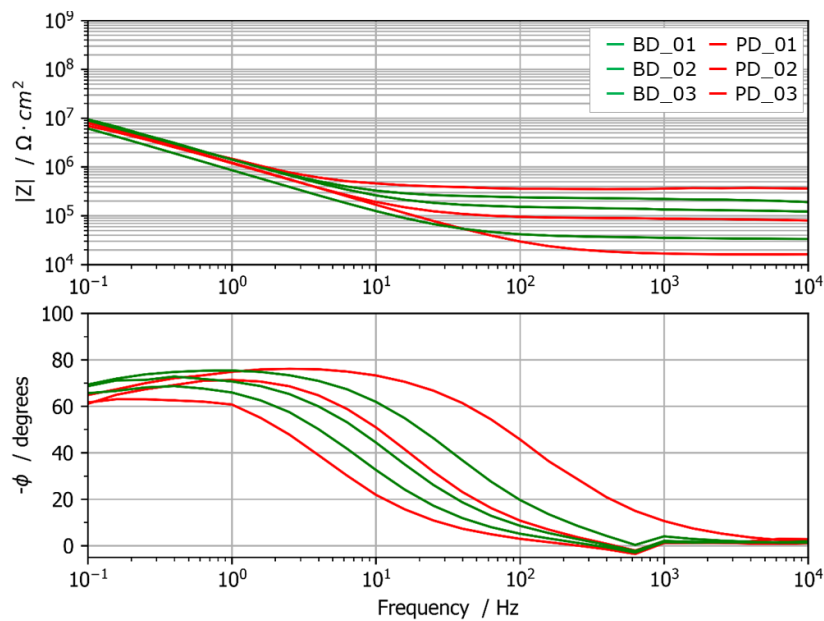


Fig. 3.29 Impedance spectra collected on a non-demineralized tooth. Spectra were collected on three different areas on the tooth surface, before and after the demineralization treatment. No significant phase shift is visible in the spectra: the measurement area did not exhibit any demineralization.

It can be observed that teeth spectra before and after demineralization have the same shape, however the demineralized tooth shows, at high frequencies, impedance magnitude values lower than the before-demineralization tooth. Moreover, for the tooth before the demineralization (green lines Fig. 3.28), the impedance phase remains at  $0^\circ$  for a wider frequency range and reaches  $-60^\circ$  only below 1 Hz, while post demineralization (red lines Fig. 3.28), the impedance phase reaches its maximum at

### 3.4 Demineralization: Experimental procedure

about  $-70^\circ$ . In addition, a noticeable phase shift due to the surface demineralization, on the other hand no significant change is visible in another tooth shown in Fig. 3.30.

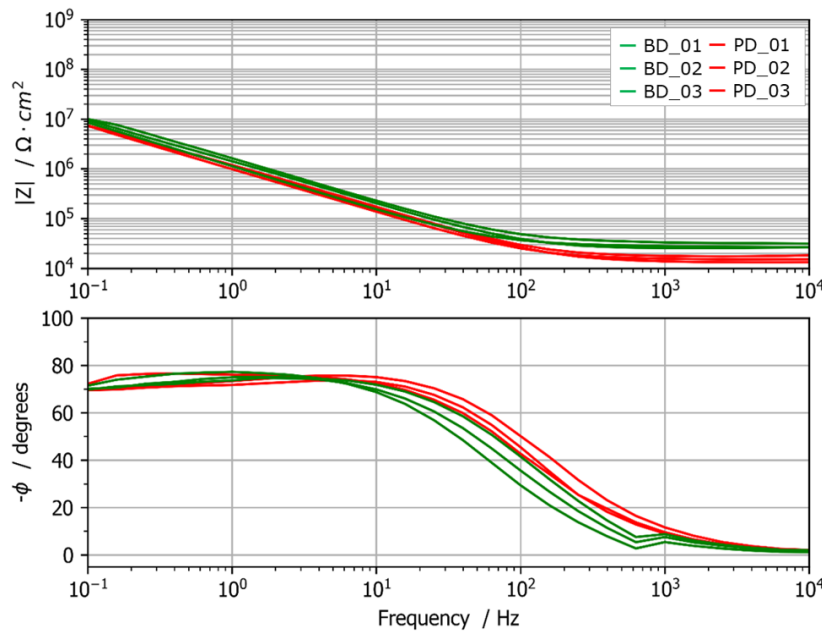


Fig. 3.30 Impedance spectra collected on a non-demineralized tooth. Spectra were collected on three different areas on the tooth surface, before and after the demineralization treatment. In this case, no significant phase shift is visible in the spectra.

Actually, not all the examined samples exhibit the same behaviour, this can be ascribed to the high inter- and intra-variability of human teeth.

Indeed, some anomalous behaviour of impedance spectra, as well as Raman spectra, may depend on several factors: tooth history and state, surface defects, age, ethnicity and healthy of the donor, and so on.

Therefore, in order to correlate the impedance spectra with the tooth surface morphology, the samples were analyzed by SEM. For example in Fig. 3.29 is not possible to clearly discriminate by the impedance spectra the tooth before or after demineralization, thus, the sample was observed by SEM.

SEM images, captured at low magnification (780 x) using an acceleration voltage of 15 kV working at a distance of about 6.6 mm, in the supposed delimited demineralized area are shown in Fig 3.31. This picture shows that the enamel surface is characterized by both demineralized and intact areas, hence the demineralization process did not affect the whole surface. Moreover, a visible crack is present.

This structure can be correlated to the different trends of impedance measurements

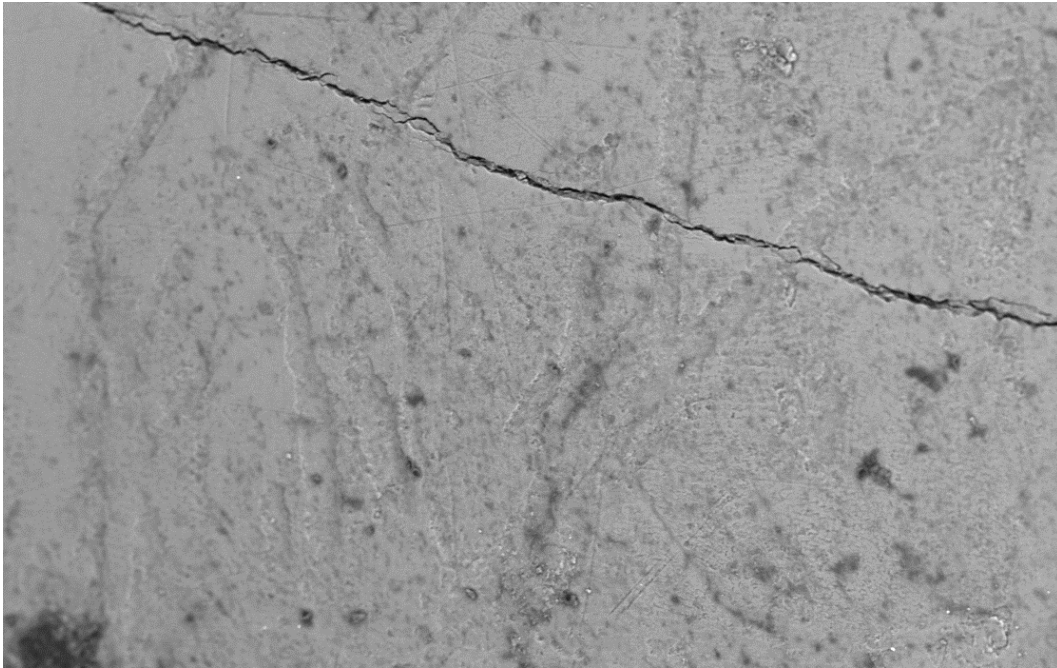


Fig. 3.31 Scanning electron microscope (SEM) image of tooth enamel surface post demineralization treatment unevenly demineralized

shown before that change according to the different positions of the probe on the tooth surface.

Another example of SEM image, where the demineralization affects almost the entire surface, is presented in Fig 3.32, obtained with magnification equal to 2200x. Indeed, the corresponding impedance measurements as concern the demineralized tooth are characterized by overlapping curves: this may be attributed to different measurements collected in areas equally affected by demineralization. By and large, curves with very similar shapes may be related to impedance measurements acquired in areas with similar properties.

In summary, by coupling impedance spectroscopy with SEM, and Raman spectroscopy it is possible to correlate the current response with morphological, and chemical information, obtaining a comprehensive picture of the state of health of the tooth.

For this purpose, impedance spectroscopy measurements are used to distinguish healthy teeth from demineralized ones. Particularly, the Bode diagrams represent a valid means to graphically discriminate between demineralized and sound teeth, however, in order to overcome some in-vivo limits, also another approach has been

### 3.4 Demineralization: Experimental procedure

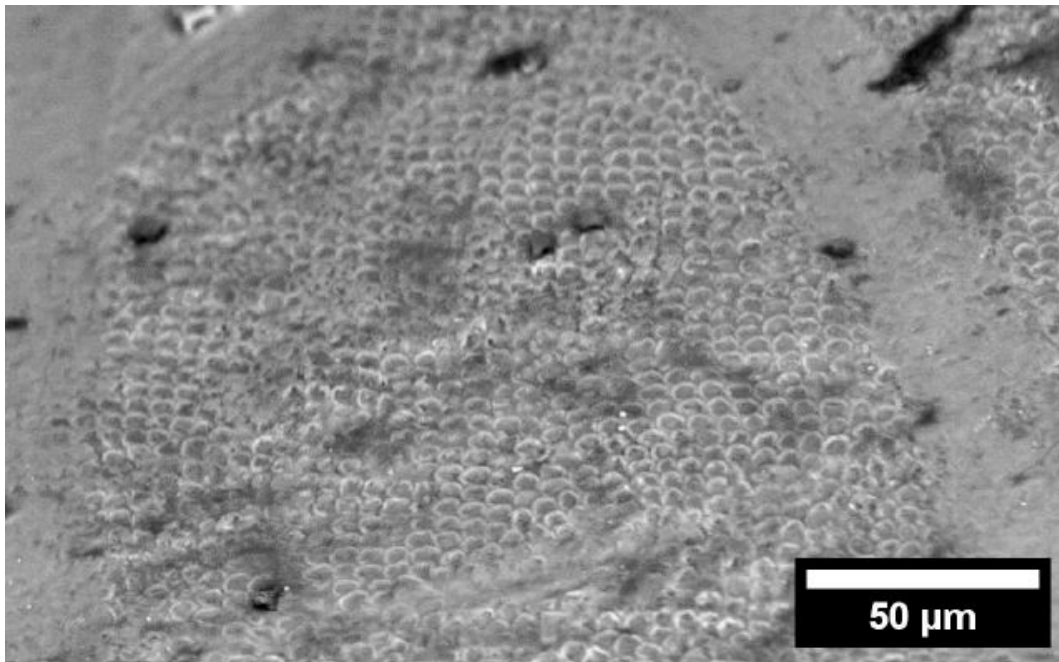


Fig. 3.32 SEM image of tooth enamel surface post demineralization treatment.

used, which involves the use of impedance phase. The measured impedance values are not normalized for the sample area, this approach was chosen because, although it would be possible to measure the area of the samples analyzed in these in-vitro measurements, this would be impossible in standard in-vivo applications. Therefore, to overcome this intrinsic limit of the measurement, to discriminate healthy teeth from demineralized teeth only the phase trend was analyzed instead of the impedance modulus. In fact, this latter is not dependent on the surface of the sample, but only on its dielectric properties.

Moreover, as previously discussed, the impedance phase trend presents a different behaviour between demineralized and sound teeth. Indeed, this value remains close to  $0^\circ$  in a larger frequency range for sound teeth. In particular, the frequency value at which the phase reaches  $-45^\circ$  to discriminate between demineralized and no-demineralized teeth, was selected. The result is shown in Fig. 3.33 . In case the phase value equal to  $-45^\circ$  is not reached during the measurement, the lowest frequency analyzed has been reported.

The result of these measurements shows how this parameter appears to be effective for discriminating healthy teeth, namely before the demineralization treatment, and demineralized ones. As can be seen, this parameter is able to discriminate samples in two different clusters. Demineralized teeth, represented by red symbols, group

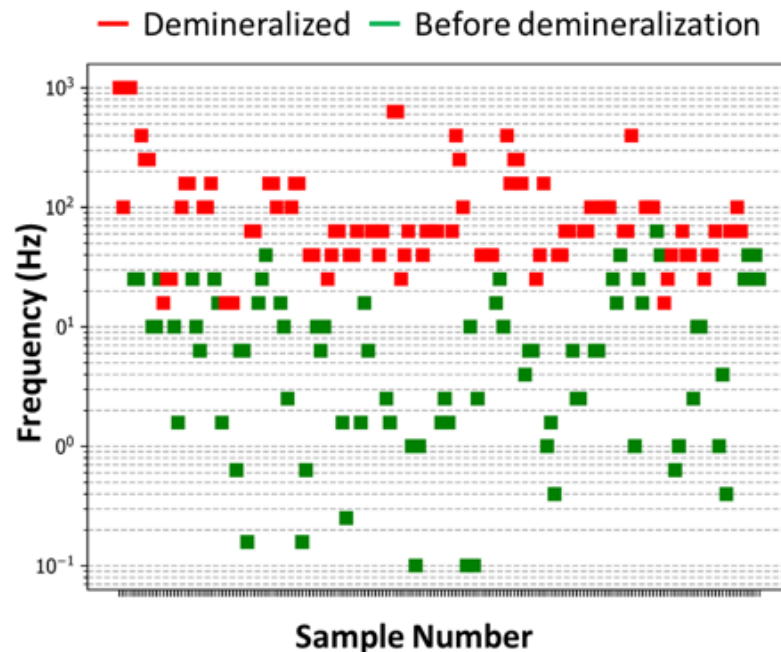


Fig. 3.33 Frequency at which the impedance phase reaches  $-45^\circ$  both for demineralized teeth (in red) and for before demineralization (in green)

in the upper part of the graph, as they reach the  $-45^\circ$  value for the phase at higher frequencies. Conversely, no-demineralized (before the demineralization treatment) teeth are in the lower part of the plot, as in this case the phase value remains close to  $0^\circ$  for a longer frequency range. In addition, it can be noticed that the frequency at which the phase value  $-45^\circ$  is reached, is higher than 10 Hz for teeth undergoing demineralization treatment, while it is lower than 10 Hz for teeth measured before the demineralization treatment.

In this plot not all measurements are reported, indeed measurements related to teeth not affected by the demineralization treatment, validated by SEM, (outliers) are eliminated. In conclusion, a significant difference between teeth before and after demineralization teeth can be observed according to the frequency at which the phase reaches  $-45^\circ$  can be considered a threshold value that allows to discriminate samples in two different clusters and classify sound and demineralized.

The result of these measurements shows how this parameter seems to be effective in discriminating between healthy and demineralized teeth. However additional analysis and considerations are needed, since for in-vivo application is not possible



### 3.4 Demineralization: Experimental procedure

to know the previous status of the analyzed tooth, and thus compare the before and after status, like in this study; so further classification algorithms will be conceived. This early evidence seems to be a promising starting point for developing a painless and non-invasive methodology to identify demineralized teeth as well as decayed ones. Furthermore, also thanks to the development of ad-hoc instrumentation, it will be possible to carry out in-vivo measurements, in order to validate this new methodology on real cases.

#### 3.4.4 Equivalent Electrical Circuit

The results of impedance spectra were modeled by an appropriate electrical equivalent circuit, allowing thus to discriminate the contribution of each element present in the sample and of the employed setup.

The electric circuit previously described will be used also to model spectra of both demineralized and sound teeth, but in this case, the contribute related to the solution resistance and the one related to the interface resistance between the tooth and the platinum wire are represented by only one resistor, namely  $R_0$ . The latter, in series with a constant phase element  $CPE_1$  in parallel with a second resistor  $R_1$ , as shown in Fig. 3.34. The parallel takes into account the porous structure of the tooth due to demineralization and the electrical parameters related to the structure of enamel and dentin.

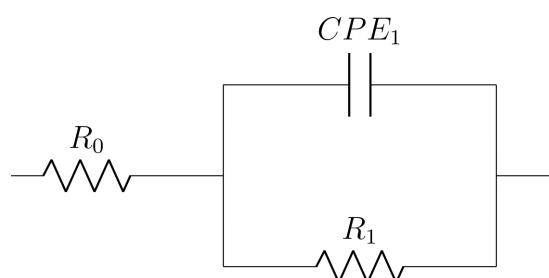


Fig. 3.34 Equivalent electric circuit used to model the impedance spectra acquired on the teeth.

For this study a set of 50 teeth was analyzed, impedance spectra were collected before and after demineralization and the equivalent electrical circuit was developed for each measure.

## Impedance measurements in dentistry

The electrical parameters considered, and their percentage variation, are:  $R_1$ , the load transfer resistance,  $Q_1$ , the double-layer capacitance, and  $R_0$  the contact resistance.

In this section some representative samples are analyzed, for each of them the electrical parameter are reported, then the percentage variation of the electrical parameters before and after the demineralization procedure are calculated.

The percentage variation was calculated as follows:

$$\text{PercentageVariation} = \left( \frac{x_f - x_i}{x_i} \cdot 100 \right) \% \quad (3.2)$$

Where  $x_i$  is the value related to the tooth before the demineralization, while  $x_f$  is the value of the parameters associated with the tooth after demineralization.

The Ivium software was used to model the impedance measurements and assess the circuit parameters.

Fig. 3.35 shows the equivalent circuit fit of the tooth before the demineralization. On the left of Fig. 3.35 the Bode diagram, where the blue dots are the experimental data, while the continuous line represents the model, it shows a good fitting; nevertheless, some points at high frequency were excluded in order to find the best fitting set of circuit parameters. Also for the Nyquist diagram, on the left of Fig. 3.35 a slight difference between measured data and the model can be observed for the highest impedance values.

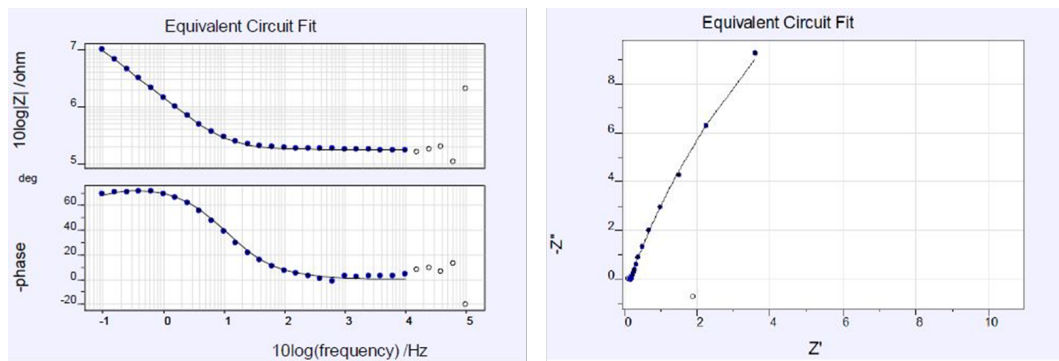


Fig. 3.35 Bode diagrams, on the left, and Nyquist diagram, on the right, of a tooth before demineralization modeled through Ivium software, blue dots are experimental data, while the continuous line represents the model.

### 3.4 Demineralization: Experimental procedure

The same elaboration was done also on a demineralized tooth and the results are shown in Fig. 3.36 in terms of the Bode and Nyquist diagram.

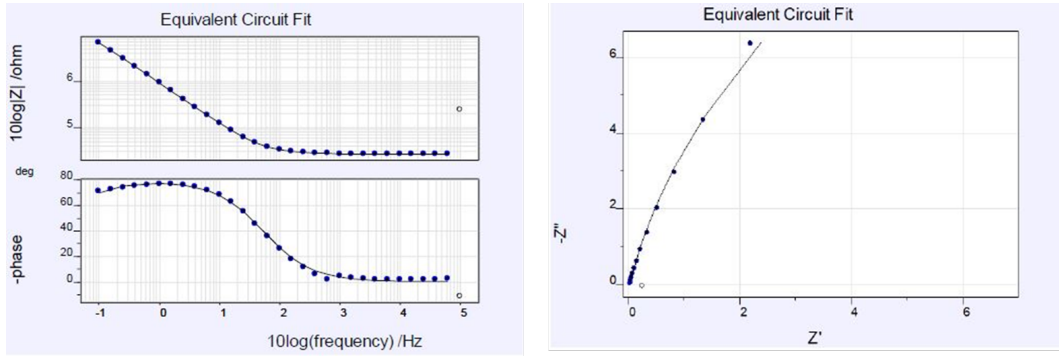


Fig. 3.36 Bode diagrams, on the left, and Nyquist diagram, on the right, of a demineralization tooth modeled through Iviu software, blue dots are experimental data, while the continuous line represents the model

The examples of some previously analyzed spectra are reported below. Equivalent electrical circuit parameters referred to the sample, whose impedance spectra are shown in Fig. 3.28 are reported in Table 3.3

Table 3.3 Equivalent electrical circuit parameters computed for a tooth before and after demineralization (results coming from the spectra reported in Fig. 3.28)

	$R_0$ [ $\Omega$ ]	$R_1$ [ $\Omega$ ]	$Q_1$ [ $s^N/\Omega$ ]	$N_1$
<b>Before Demineralization</b>	$3.17 \cdot 10^5$	$1.41 \cdot 10^7$	$2.46 \cdot 10^{-7}$	$8.22 \cdot 10^{-1}$
<b>Post Demineralization</b>	$2.64 \cdot 10^4$	$3.44 \cdot 10^7$	$1.80 \cdot 10^{-7}$	$8.88 \cdot 10^{-1}$

In this case, the parameter that changes the most is  $R_0$ , which has a lower value in the tooth after demineralization. The double-layer capacitance,  $Q_1$ , shows a minimal variation, a negligible increase for the demineralized tooth with values in the same order of magnitude. On the other side,  $R_1$  values changes but they are affected by a significant estimation error 6.90% for tooth before demineralization and 15.09% for tooth post demineralization). Percentual variations before and post demineralization are reported in Table 3.4.

## Impedance measurements in dentistry

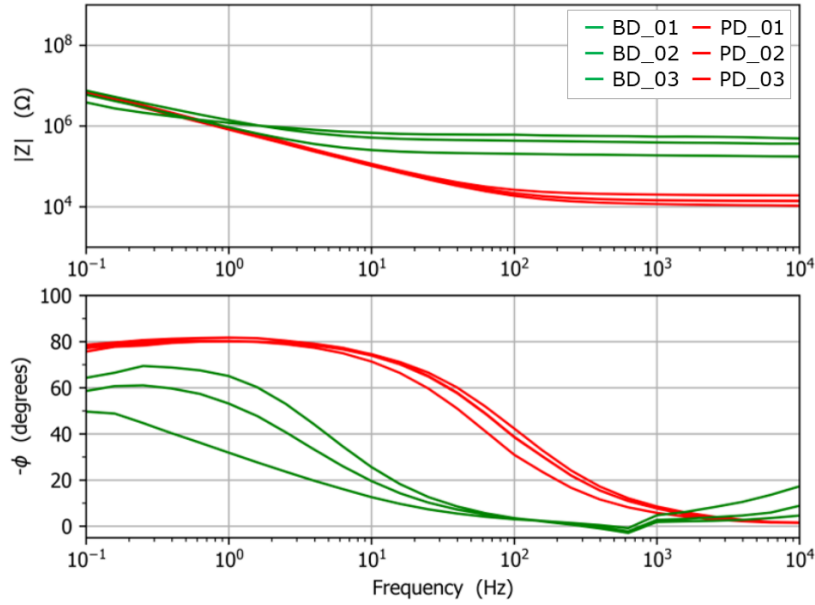


Fig. 3.37 Caption

Table 3.4 Percentage variation relative to the equivalent electrical circuit parameters reported in Table 3.3

	$R_0$ (%)	$R_1$ (%)	$Q_1$ (%)
<b>Percentage Variation</b>	-91.67	143.97	-25.61

Another example is shown in Fig. 3.37 and the corresponding equivalent electrical circuit parameters are reported in Table.

Even in this case, the most variable parameter is  $R_0$ ,  $Q_1$ , shows a limited variation and  $R_1$  values present a significant estimation error (29.99% for tooth before demineralization and 56.28% for demineralized tooth). Percentage variations before and after demineralization are reported in Table 3.6.

Table 3.5 Equivalent electrical circuit parameters computed for a tooth before and after demineralization (results coming from the spectra reported in Fig. 3.37).

	$R_0$ [ $\Omega$ ]	$R_1$ [ $\Omega$ ]	$Q_1$ [ $s^N/\Omega$ ]	$N_1$
<b>Before Demineralization</b>	$4.04 \cdot 10^5$	$4.13 \cdot 10^7$	$1.94 \cdot 10^{-7}$	$7.93 \cdot 10^{-1}$
<b>Post Demineralization</b>	$1.06 \cdot 10^4$	$8.20 \cdot 10^7$	$2.39 \cdot 10^{-7}$	$9.98 \cdot 10^{-1}$

### 3.4 Demineralization: Experimental procedure

Table 3.6 Percentage variation relative to the equivalent electrical circuit parameters reported in Table 3.5.

	$R_0$ (%)	$R_1$ (%)	$Q_1$ (%)
<b>Percentage Variation</b>	-97.38	98.54	23.19

In conclusion, all the examined teeth, both before and after demineralization, present circuit parameters with the same order of magnitude:

- $R_0$  is about  $10^5 \Omega$  for teeth before demineralization and  $10^4 \Omega$  for demineralized ones;
- $R_1$  is about  $10^7 \Omega$  for all the samples;
- $Q_1$  is about  $10^{-7} s^N / \Omega$  for all teeth.

These orders of magnitude can be useful to design a proper measuring device.

#### 3.4.5 Classification Algorithm

"The detection of the dynamic process of carious lesions is decisive to properly manage the prognosis and any preventive intervention, and to assess the efficacy of the therapeutic procedure." "Regardless all the technological progress, the gold standards for the early detection of dental carious lesions, in clinical practice, remain the use of visual and visual–tactile tools, such as sharp explorers and dental radiographs [188]." [11] As widely previously discussed, "these clinical diagnostic methods are operator dependent and not risk-free; moreover, they are characterized by poor sensitivity and specificity for the early detection of carious lesions [189][190]." "Thus, to support dentists in caries lesion detection and diagnosis the usage of AI, especially deep learning, is growing with promising results [191]. However, the proposed studies are mainly based on images, such as bitewing radiography, cone-beam computed tomography, panoramic radiography [192], or less common clinical techniques like near-infrared light transillumination [193] or optical coherence tomography [194]. The accuracy of deep learning for classifying carious lesion varies greatly according to the used techniques, i.e. it ranges between 68.0% to 78.0% for near-infrared transillumination images, from 87.6% to 95.4% for bitewing radiographs, and it can reach 95.2% with optical coherence tomography images [195]."[11]

The main aim of this dissertation section is to develop a simple automatic approach for the assessment of the demineralization of teeth by performing impedance

## Impedance measurements in dentistry

---

measurements on the teeth' surface. "The proposed approach tries to take advantage of the change of phase due to the demineralization process. Thus, an automatic classifier was developed by employing a modified single neuron as shown in Fig. 3.38"[11] "In order to assess the best parameters for the classifiers, preliminary data analysis was carried out on the acquired spectra. It is clear that the phase shift due to tooth demineralization is the main parameter that should be taken into account.

A total of about 110 spectra were processed. In particular, about 70 spectra refer to demineralized teeth while the other 40 to non-demineralized ones. The first analysis was carried out by computing the average phase difference before and after demineralization for different values of frequency from about 1 Hz to 10 kHz. The results, shown in Fig. 3.39 (on top), highlight a remarkable phase change considering the measurement before and after treatment. Then, it was computed the average phase difference between the pre- and post-treatment samples with the aim of finding the best frequency value for assessing the demineralization of the teeth. The average phase difference is reported in Fig. 3.39 (at the bottom). It is evident how the higher the phase difference, the simpler and more effective it will be to discriminate between demineralized and non-demineralized teeth. Therefore, the best frequency for assessing demineralization was taken as 15 Hz."[11]

"Subsequently, a modified single neuron classifier was developed so that given as input the phase at 15 Hz it is able to provide at its output a value between 0% and 100%, where 0% corresponds to a totally non-demineralized tooth and 100% a totally demineralized one. Therefore, a threshold of 50% was employed to discriminate between the two possible situations. The classifier was designed to employ an inverted sigmoid decision function. The key parameters which allow the classifier to properly operate are the Input Bias, the weighting Factor  $W$ , and the Sigmoid Gain  $G$ . These parameters were set trying to minimize the error rate of the classifier

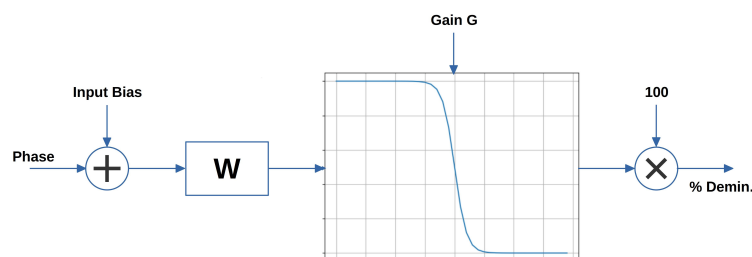


Fig. 3.38 The used classifier with an inverted sigmoid as decision function [11].

### 3.4 Demineralization: Experimental procedure

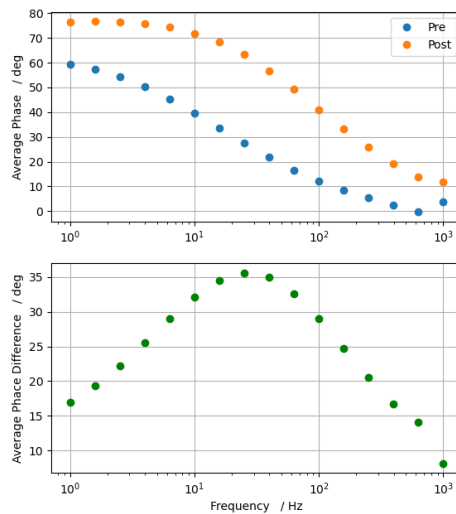


Fig. 3.39 "First plot shows the average phase of all samples, where blue dots represent measurements carried out before the demineralization, while orange dots post-demineralization. The bottom plot shows average phase difference before and after demineralization for each frequency. The frequency spans in the range 1 Hz to 1 kHz. The highest value of average phase difference is achieved at a frequency of about 15 Hz." [11]

according to the following considerations:

- 1) The bias was set at the average phase value of the demineralized teeth plus the demineralized phase standard deviation multiplied by 1.5, obtaining a value of 65.5°.
- 2) The sigmoid gain defines the smoothness of the decision function. In particular, setting a high gain gives a steep function, while a value lower than 1 provides a smoother sigmoid. The best results were obtained with a value of 2.
- 3) The weighting factor was set directly to 1 in order to avoid further changes in the input phase." [11]

"Then the available tooth measurements were processed by the classifier by using as input the single phase value at 15 Hz. The classification results are shown in Fig. 3.40. Here the demineralization state is reported as percentage of demineralization, being 100% the expected output for demineralized tooth and 0% the expected output for a non-demineralized one. About 100 teeth were processed by the classifier (about 75 demineralized and 25 non-demineralized, accordingly to the available spectra). As it is possible to see most of the teeth are correctly classified." [11]

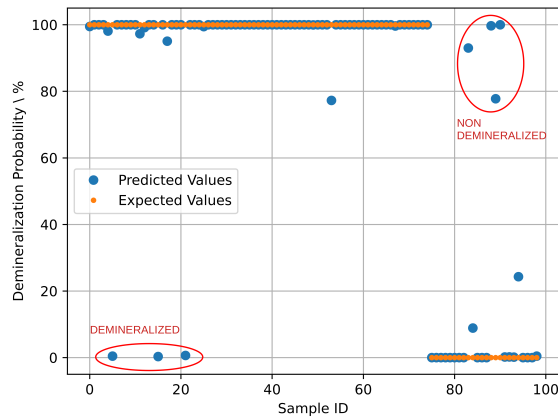


Fig. 3.40 Employed classifier results. Blue dots: the predicted values of the neural network on all the samples. Orange dots: the expected values. Classification errors are marked by red circles.[11]

"In total, the classifier failed on only 7 teeth over about 100 achieving an error rate of about 7%. In particular, 3 demineralized teeth were classified as non-demineralized, and 4 non-demineralized teeth were classified as demineralized."[11]

### 3.4.6 Performance evaluation of multiple classifiers

After the preliminary results shown before, different classifiers were tested on the same data set.

Classification is a supervised machine learning process that allows classifying a specific set of input data into classes based on one or more variables. In addition, the classification of structured and unstructured data allows to accurately predict whether the data will fall into predetermined categories. Some of the most common classification algorithms include: binary classification, multi-class classification, multi-label classification, and imbalanced classification [196].

In this dissertation binary classification will be used because binary is a kind of problem in classification in machine learning that presents only two possible outcomes. All data were assigned to two classes, and each of the data objects was assigned to only one specific class; because there are only two possible states for the teeth. Likewise in this case where the final aim is to discriminate between demineral-



### 3.4 Demineralization: Experimental procedure

---

ized and not-demineralized teeth.

Hereafter, some common machine learning classification algorithms will be employed to find the most suitable one for our study.

The used data set includes impedance measurements collected on the tooth before and after the demineralization. For all the samples the value of the impedance phase at 15 Hz was selected as the classification parameter. The dataset was built by associating the measurement ID code to each measure, to the known tooth state, namely demineralized associated with class1 and not-demineralized with class0. For each iteration they were randomly mixed, then 60% of the data set was used for training and the remaining 40% for testing the algorithms. For each classification algorithms, different performance parameters were calculated. Since the random data selection, each iteration trains and tests the different classifiers on different sets of data. Among all the iteration, the average accuracy and the standard deviation for each classifier were calculated. In this case, the accuracy represents the ratio of the number of correctly classified objects to the total number of objects evaluated. A k-fold cross-validation with k=5 was performed in order to obtain the accuracy of each classifier for each random iteration.

For each classifier (scikit-learn package [197]) different performance parameters were assessed. The performance of a classification algorithm gives useful information about how well the model works [198][199]. Among the most popular were calculated:

- Precision: the ratio of correctly predicted positive data to the total predicted positive data.  $\frac{T_p}{T_p+F_p}$  where  $T_p$  is the number of true positives and  $F_p$  the number of false positives;
- Recall: the ratio between the number of correct positive results and the total number of relevant samples (all samples that should have been identified as positive). It is also known as sensitivity:  $\frac{T_p}{T_p+F_n}$  where  $T_p$  is the number of true positives and  $F_n$  the number of false negatives;
- F-score: a weighted average of the precision and recall. When F-score reaches the value 0 the model is the worst possible, while it reaches its best value at 1. Its formula is:  $F - score = 2 * \frac{(precision*recall)}{(precision+recall)}$ ;

One of the implemented classifiers is the Nearest Neighbour which achieves consistently high performance, without a priori assumptions about the distributions of the

## Impedance measurements in dentistry

training examples. The sample is classified by calculating the distance to the nearest training case. In k-NN, the  $k$  value is the number of nearest neighbours. This value represents the deciding factor for the classifier since the  $k$ -value decides how many neighbours influence the classification. In this case  $k$  was selected as 3 which was the resulting best hyperparameter.

Fig. 3.41 shows the results of the implemented classifiers with a score of 82.2%, the accuracy ranged from a maximum of 8.3% to a minimum of 73.3 %; while Tab. 3.7 some classification parameters calculated on 20 iterations.

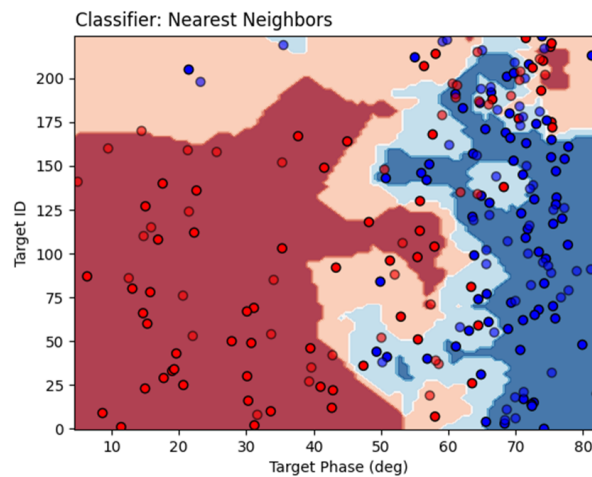


Fig. 3.41 Result of the Nearest Neighbors classifier with 82.2% accuracy. Red dots are not-demineralized teeth while blue dots are demineralized teeth.

Table 3.7 Average Nearest Neighbours classifier's performance.

	Accuracy [%]	Recall [%]	F-score [%]	Precision [%]
<b>Near Neigh.</b>	77.9±2.9	79.3±4.5	81.6±4.5	78.6±5.2

The second classifier used is the linear Support Vector Machines. Support Vector Machines are a set of supervised learning that find a combination of samples to build the optimal hyperplane that divides the data into two classes. The hyperparameters associated with SVM are the Kernel and the  $C$  parameter. The latter can be defined as the number of permitted errors, that is, the degree of correct classification that the algorithm has to meet. In this case  $C$  was selected as 0.025. The results of this classifier on 20 iterations are shown in Fig.3.42 and in Tab. 3.8; in particular, the accuracy range was [72.2-80.0]%.

### 3.4 Demineralization: Experimental procedure

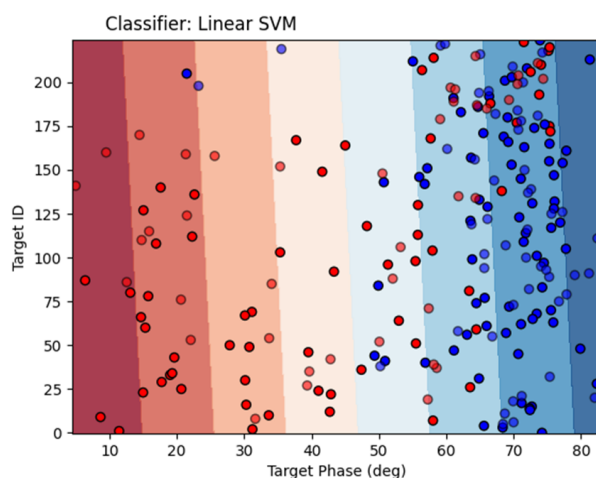


Fig. 3.42 Result of Linear SVM with linear Kernel classifier with accuracy 76%

Table 3.8 Support Vector Machine with linear Kernel classifier's performance.

	Accuracy [%]	Recall [%]	F-score [%]	Precision [%]
<b>SVM</b>	76.6±2.3	81.3±2.0	96.0±1.9	70.9±2.2

The kernel function can be also a Radial Basis Function (RBF) centered at each point. In this case, two parameters must be considered, the before mentioned  $C$  which controls the trade-off between achieving a good fit to the training data and a simple decision boundary, and the  $\Gamma$ .

$\Gamma$  is a parameter for non-linear hyperplanes that controls the distance of the influence of a single training point. The results of the RBF SVM are shown in Fig. 3.43 and Tab. 3.9 where  $\Gamma$  was set as 2 and  $C$  as 1. The minimum and the maximum accuracy value were 72.2% and 84.4% respectively.

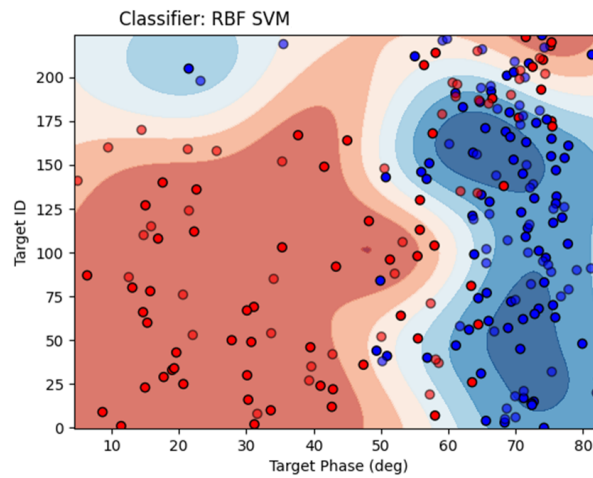


Fig. 3.43 Result of Radial Basis Function SVM with 79% accuracy

Table 3.9 RBF SVM classifier's performance.

	Accuracy [%]	Recall [%]	F-score [%]	Precision [%]
<b>RBF SVM</b>	78.9±3.0	80.1±4.6	83.3±4.9	79.2±5.8

The Gaussian Process Classifier (GPC) uses Gaussian Processes (GP) to classify, especially for probabilistic classification, where test predictions have the form of class probabilities. For GPC different kernels can be specified, in this case, the BF (Radial Basis Function) kernel was implemented. The RBF kernel enables the GP to acquire non-linear relationships between input variables and output labels by appointing higher weights to points that are closer together in the input space. The results of the implemented Gaussian Process are listed in Tab. 3.10 and shown in Fig. 3.44. Accuracy range: [ 72.2%-84.4%].

### 3.4 Demineralization: Experimental procedure

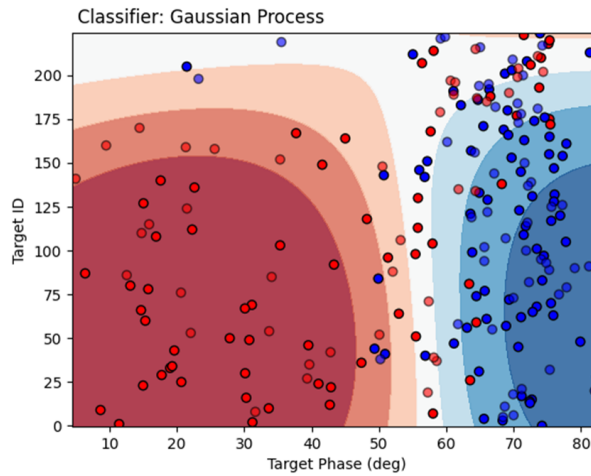


Fig. 3.44 Result of Gaussian Process classifier with 76.0% accuracy.

Table 3.10 Gaussian Process classifier's performance.

	<b>Accuracy [%]</b>	<b>Recall [%]</b>	<b>F-score [%]</b>	<b>Precision [%]</b>
<b>Gaussian Pro</b>	78.7±2.8	80.7±5.0	84.8±4.6	78.6±6.1

Another implemented classifier was the decision tree classifier. It works by creating a tree-like model of decisions. The root node is at the top of the tree, it represents the entire dataset. Each node specifies a test on an attribute, it is split into two or more branches, each one corresponds to one of the possible values for that attribute. The root node is split into two or more child nodes based on the most significant feature that best separates the data into different classes.

The depth of a decision tree is a critical hyperparameter that determines how many splits (the maximum number of levels or nodes from the root node) a tree can make before coming to a prediction. In this case, the depth was set at 5. The corresponding results are shown in Fig. 3.45 and Tab. 3.11, where the accuracy varies between 72.2% and 82.2%.

Table 3.11 Decision tree classifier's performance.

	<b>Accuracy [%]</b>	<b>Recall [%]</b>	<b>F-score [%]</b>	<b>Precision [%]</b>
<b>Decision Tree</b>	75.9±2.8	77.6±5.1	77.0±6.0	81.1±4.9

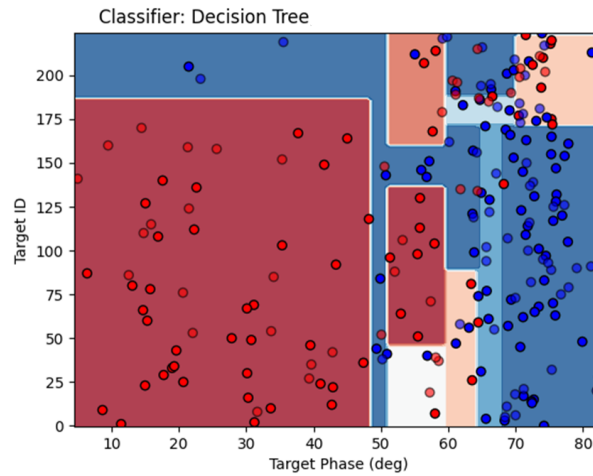


Fig. 3.45 Result of the Decision tree classifier with 74.0% accuracy.

Random Forest builds multiple decision trees and combines their predictions to make a final decision. Random Forest includes a number of decision trees, each one trained on a different subset of the training data and a random subset of input features. The random selection of data and feature reduces the risk of overfitting and increase the model’s generalization performance. In order to improve the model’s performance, several parameters can be tuned. Among them, the *n-estimators*, in which T specifies the number of decision trees in the Random Forest was set as 10; the *max-depth* which controls the maximum depth of each decision tree, set as 5, and the *max-features* that controls the maximum number of features that can be used for each split in each decision tree, set as 1. By selecting this parameter the following results were obtained (Fig. 3.46 and Tab. 3.12) and the accuracy ranged from 70.0% to 85.6%.

Table 3.12 Random Forest classifier’s performance.

	Accuracy [%]	Recall [%]	F-score [%]	Precision [%]
<b>Random Forest</b>	78.2±3.7	77.9±4.8	79.1±4.7	78.8±5.5

A Multilayer Perceptron has input and output layers, and one or multiple hidden layers of interconnected neurons. The output layer generates the final prediction for the classification. The input layer collects the input features, and each neuron in the hidden layers performs a non-linear transformation to the input and moves the output

### 3.4 Demineralization: Experimental procedure

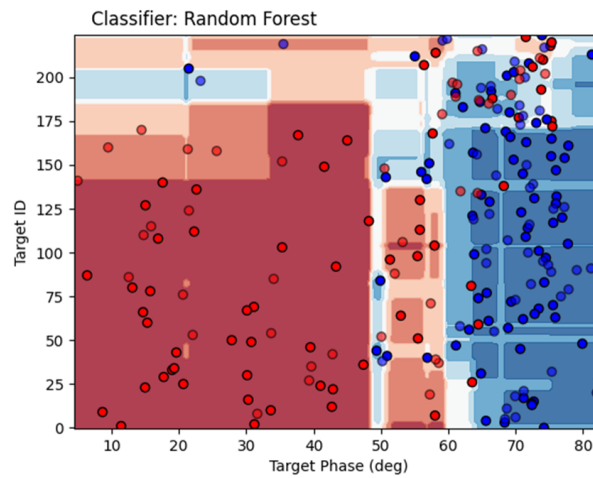


Fig. 3.46 Result of Random Forest classifier with 80.0% accuracy.

to the next layer.

The model's performance can be improved by several parameters, in this application the Alpha parameter (set as 1), known as the penalty term, which combats overfitting by constraining the size of the weights. A higher Alpha value may reduce overfitting, but may also reduce the model's accuracy.

Subsequently, the max iterations, which represent the maximum number of iterations allowed for the optimization algorithm was set as 1000. A large number of iterations may improve the model's accuracy but also increases the training time. The results of MLP are presented in Fig. 3.47 and Tab. 3.13 and the accuracy varies from a minimum of 72.2% to 85.6%.

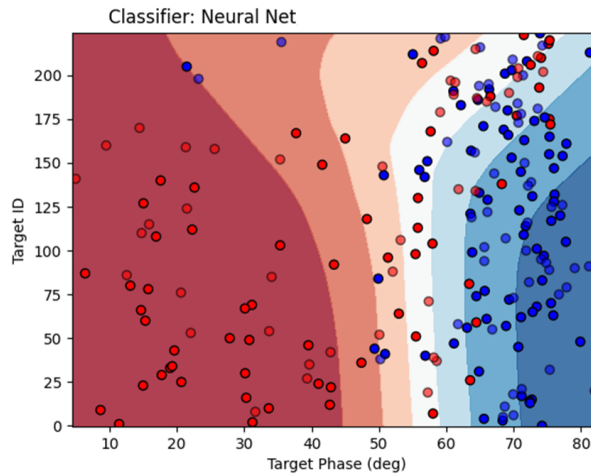


Fig. 3.47 Result of Neural Net Multilayer Perceptron classifier with 77.2% accuracy.

Table 3.13 Multilayer Perceptron Neural Net classifier’s performance.

	<b>Accuracy [%]</b>	<b>Recall [%]</b>	<b>F-score [%]</b>	<b>Precision [%]</b>
<b>Neural Net</b>	77.7±2.8	80.6±3.5	86.2±4.2	76.5±4.1

The AdaBoost classifier combines multiple poorly performing classifiers to build a stronger classifier able to achieve high accuracy. The algorithm combines these weak classifiers by allocating higher weights to the samples that are misclassified by the former classifiers. This iterative process lasts when a selected number of weak classifiers have been trained, or until the desired accuracy has been achieved. The results for this classification algorithm are shown in Tab. 3.14 and Fig. 3.48 and the accuracy range [66.4-84.4]%.



### 3.4 Demineralization: Experimental procedure

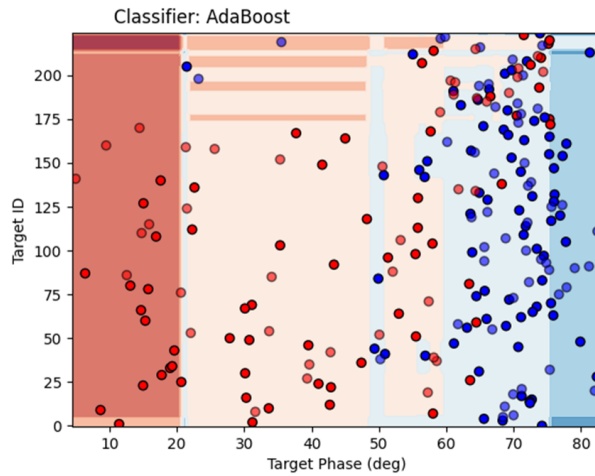


Fig. 3.48 Result of Ada Boost classifier with 79.0% accuracy.

Table 3.14 Ada Boost classifier's performance.

	Accuracy [%]	Recall [%]	F-score [%]	Precision [%]
<b>QDA</b>	75.1±4.5	75.6±5.8	76.4±6.2	78.8±6.2

Gaussian Naive Bayes (GNB) algorithm for classification is a variant of the Naive Bayes algorithm where the likelihood of the features is assumed to have a Gaussian probability distribution with a mean and variance calculated from the training data [200]. GNB computes the likelihood of each class feature and then associates them through Bayes' theorem to calculate the posterior probability of each class. The class with the highest posterior probability is thus assigned to the new instance. Fig. 3.49 and Tab. 3.15 represent the results, in particular, the accuracy varies from 77.4 % to 85.6%.

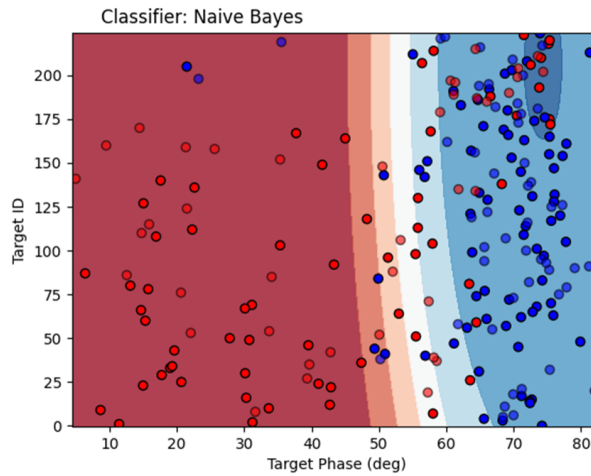


Fig. 3.49 Result of Gaussian Naive Bayes classifier with 76.0% accuracy

Table 3.15 Gaussian Naive Bayes classifier’s performance.

	Accuracy [%]	Recall [%]	F-score [%]	Precision [%]
<b>G. Naive Bayes</b>	78.4±2.3	81.8±2.7	91.6±3.4	74.6±3.2

The last computed classifier was Quadratic Discrimination, namely the general form of Bayesian discrimination. Quadratic Discriminant Analysis (QDA) assumes that each class follows a Gaussian distribution; in particular, the likelihood of a specific class is modeled as a multivariate Gaussian distribution with a mean and a covariance matrix assessed from the training data. As the GNB, computes the likelihood of each class feature and then associates them through Bayes’ theorem to calculate the posterior probability of each class and classify a new instance. The class with the highest posterior probability is thus assigned to the new instance. The results of this classifier are shown in Fig. 3.50 and Tab. 3.16. The accuracy range was [77.4-85.6]%.

### 3.4 Demineralization: Experimental procedure

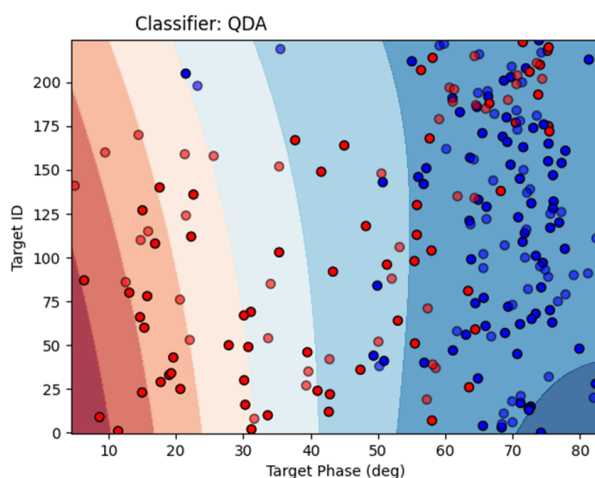


Fig. 3.50 Result of Quadratic Discriminant Analysis with 75% accuracy.

Table 3.16 Quadratic Discriminant Analysis classifier's performance.

	Accuracy [%]	Recall [%]	F-score [%]	Precision [%]
<b>QDA</b>	77.9±2.3	81.6±2.8	91.1±3.3	74.6±3.1

The classification was carried out over 20 iterations and the average performance achieved by each classifier is shown in Tab. 3.17. In particular, the average accuracy represents the average fraction of correctly classified teeth while the standard deviation of the accuracy gives information on the variability of the accuracy over the 20 iterations for each one of the tested classifiers. All the classifiers reached an accuracy higher than 75%. However, the best performance was reached by the Radial Basis Function Support Vector Machine classifier with 78.9% accuracy. While the performance results of all the classifiers are shown in Fig. 3.51.

## Impedance measurements in dentistry

Table 3.17 Performance of different classification algorithms.

Classifier	Reported Accuracy [%]	Standard Deviation [%]
Nearest Neighbors	77.9	2.9
Linear SVM	76.6	2.3
RBF SVM	78.9	3.0
Gaussian Process	78.7	2.8
Decision Tree	75.9	2.8
Random Forest	78.2	3.7
Neural Net	77.7	2.3
AdaBoost	75.1	4.5
Naive Bayes	78.4	2.3
QDA	77.9	2.3

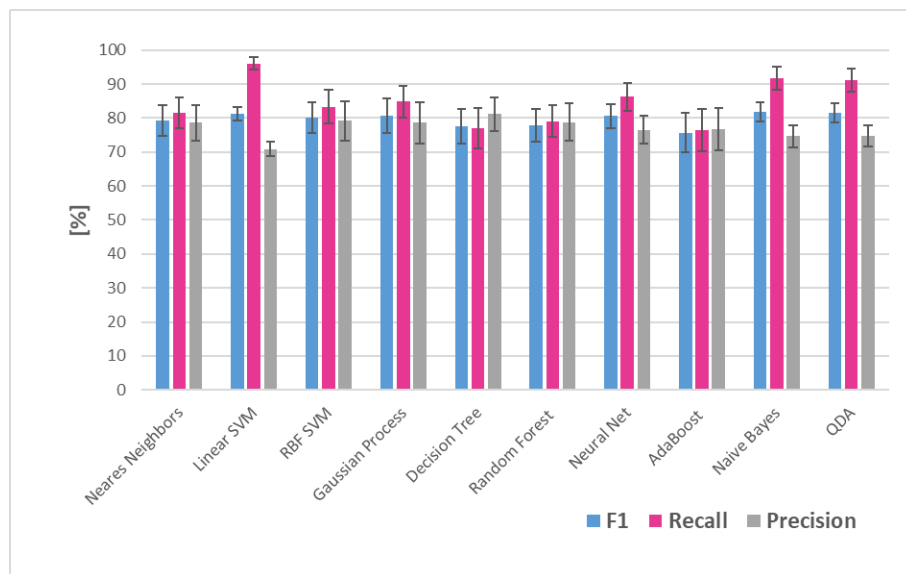


Fig. 3.51 Results of performance of each classifier: F-score (blue), Recall (pink), and Precision (grey).

# Chapter 4

## Conclusions

This dissertation presented the results of innovative measurement techniques that exploit impedance spectroscopy for human tissue characterization in different medical fields. The first part of the dissertation focuses on the application of impedance spectroscopy in medicine, by paying particular attention to drug bioavailability assessment and tissue characterization.

In the second Chapter impedance spectroscopy is proposed as a non-invasive, low-cost, and effective method for the bioavailability assessment of insulin.

Bioavailability, in case of systemic drugs, is defined as the amount of an administered drug that reaches the systemic circulation. Since at present, there are no standardized methods for non-invasive measuring of the drug delivered in-vivo; the distinct non-invasiveness of impedance analysis would persuade people with diabetes to control more often, or even continuously, their glucose concentration. An instrument, namely Insulin Meter, based on an on-chip transducer and prototyped by using off-the-shelf components was presented. The Insulin Meter allows to measure the electric impedance variation in the frequency over time, thus was used to monitor insulin absorption in real-time. The Insulin Meter design was described, by focusing on the architecture and the operating characteristics. Then, the calibration procedure was performed, showing that instrument performance is compatible with the metrological targets of the Insulin Meter design, and thus suitable for clinical application. Therefore, the Insulin Meter was characterized metrologically, in-vitro, on eggplants, and ex-vivo, on pigs tissue, by means of insulin injection.

The basic idea is that insulin bioavailability is assessed non-invasively and in real-time after administration in a specific injection site of a known amount, as in common

## Conclusions

---

therapy for people with diabetes. The Insulin Meter implements a personalized model identification by measuring step by step the impedance variation corresponding to the injection of a known amount of insulin.

The personalized model of insulin appearance is peculiar for each subject. It is identified and validated during each insulin injection. Hence, inter-and intra-individual reproducibility can be improved.

The experimental results presented in terms of accuracy performance, non-linearity, repeatability, and reproducibility, are compatible with clinical application. Proving, thus, that impedance spectroscopy is a powerful, harmless, and painless, measurement method, that can be considered a winning choice in clinical diabetology, and specifically the device could be used to customize diabetes therapies.

The last part of the second Chapter faces the problem of improving the sensitivity of the measurement method described in the first part, in order to make it more performing for clinical application.

Since experimental evidence showed that any pressure exerted during the injection procedure, and the resulting tissues' deformation, affect the impedance measurement, arising sensibility issues on the signal ascribed to the drug presence under the skin. Hence, a Finite Element Model (FEM) was implemented to model the electrical and mechanical behaviour of human tissues and, thus, to measure insulin transdermally delivered, manage intra-individual reproducibility uncertainty, and as well as improve sensitivity.

Several injection sites are available for diabetic patients, although the injection site strongly affects the pharmacokinetic absorption profile of insulin. Every injection site has a different insulin absorption kinetic, due to the different vascularization and thus subcutaneous blood flow. The abdomen is the favorite site due to its easy access and faster insulin absorption.

However modeling human tissues is challenging owing to the intrinsic complexity of biological structures; thus simplified abdomen model was described, and it consists of 3 layers, namely skin (including epidermis and dermis), fat, and muscle. The mechanical parameters used to model the abdomen are: the tissue density, elastic modulus, namely Young's modulus, and Poisson's ratio. While the electrical properties of tissues for the model, such as permittivity and conductivity, have been evaluated by the model proposed by Gabriel.

By exploiting the electrical model, different configurations of electrodic distances were tested, by changing the distance between different electrodes, in order to find

---

the one that can maximize the sensitivity of the impedance measurements during the insulin injection. The sensitivity analysis shows that the most significant parameter is the Voltmetric electrode distance from the center.

Finally, an experimental campaign on 12 volunteers was conducted to identify the condition which maximize the stability of the setup (e.g., sample subject movement's test, the pressure exerted during the injection phase and/or breathing) and to experimentally identify a relationship between applied force, related to insulin injection, and its impact, together with any mechanical stress acting on the human abdomen, on the impedance measurement.

By comparing the experimental results with the model simulations, the validity of the proposed method can be stated, and the latter can greatly improve the personalization of insulin thereby by calculating the correct dose of insulin to be injected, and taking into account that the absorption curve may change according to the applied injection force. Once validated the method on human volunteers, further studies will consider the possibility to equip the insulin pens with a force sensor that estimates the force applied to the tissue during the injection and transmit the information in real-time to the artificial pancreas, allowing thus, the optimal bolus calculation.

The third Chapter shows the advantages of employing impedance spectroscopy for dental disease assessment. In particular, in two main applications: to detect the carious lesion, and then to assess the enamel demineralization, which represents the earlier stage of the dynamic carious process. After the description of the tooth anatomy and composition, the employed setup was shown and the different analysis techniques, used to validate impedance measurements, were described.

The first part deals with the design and development of a non-invasive though rather effective solution to detect carious lesions. The possibility to use impedance spectroscopy measurements in caries detection is based on the typical loss of mineral content due to the caries process, resulting in an increased porosity of the tooth structure, which entails a higher liquid content than healthy tissue.

Thus, both sound and teeth with carious lesions were analyzed and impedance measurements were performed by means of a two-electrode measuring system and the Ivium-n-Stat potentiostat. Different types of electrodes were tested, that is, a Ni-Cr wire electrode with a diameter of 0.5 mm, and a hydrogel agar probe with a diameter of 5 mm.

The preliminary obtained results evidenced that impedance measurement is able to

## Conclusions

---

detect differences among the tested samples by highlighting a different behaviour and a shift in the phase spectra. In particular, a shift from the resistive behaviour to the capacitive-like occurs at different frequencies if the measurement is collected on the healthy tooth or in correspondence with a carious lesion, this enables simple discrimination between sound teeth and teeth with caries.

The second part deals with the development of a simple automatic approach for the assessment of tooth demineralization. To this aim, impedance measurements were performed on 50 extracted frontal human incisors. Teeth were demineralized *in-vitro* in accordance with a validated protocol. Then, a morphological analysis of the tooth surface was performed by SEM to confirm enamel demineralization, together with Raman spectroscopy, which gives information on the structure and chemical composition of the teeth surface. In particular, SEM images show a smooth and homogeneous surface for the teeth that did not experience the demineralization, while for the demineralized teeth the hexagonal structures, with an alveolar appearance typical of exposed HA crystals, were visible. While the intensity of  $PO_4^{3-}$  band ( $\sim 960\text{ cm}^{-1}$ ) and crystallinity, monitored by Raman spectroscopy, decrease with the demineralization.

Also, in this case, a change of impedance phase due to the demineralization process occurs. Data analysis confirmed that at about 15 Hz, is possible to discriminate between demineralized and non-demineralized teeth; and that this frequency value can be employed to build up an automatic classifier base on MLP topology which can reach an error rate of about 7% in classifying demineralized and healthy teeth. Then, different automatic classifiers were tested, since for *in-vivo* application the previous status of the tooth is known. All the classifiers reached an average accuracy higher than 75%, which can reach about 87% in some cases.

This work proved the possibility to discriminate between sound and demineralized teeth, and thus the carious lesion, by using impedance spectroscopy measurements. Therefore, impedance measurement can be considered an additional diagnostic method in dental practice thanks to its safety, reliability, simplicity, rapid response, cost-effectiveness, robustness, and adequate detection limit. Indeed, a portable, low-cost, non-invasive, and low-power device for the detection of caries at an early stage is under implementation.



## References

- [1] Pasquale Arpaia, Umberto Cesaro, Nicola Moccaldi, and Isabella Sannino. *Non-Invasive Monitoring of Transdermal Drug Delivery*. CRC Press, 2022.
- [2] Sanjay Kalra, Ambrish Mithal, Rakesh Sahay, Mathew John, AG Unnikrishnan, Banshi Saboo, Sujoy Ghosh, Debmalya Sanyal, Laurence J Hirsch, Vandita Gupta, et al. Indian injection technique study: injecting complications, education, and the health care professional. *Diabetes Therapy*, 8(3):659–672, 2017.
- [3] Pasquale Arpaia, Umberto Cesaro, Mirco Frosolone, Nicola Moccaldi, and Maurizio Tagliatalata. A micro-bioimpedance meter for monitoring insulin bioavailability in personalized diabetes therapy. *Scientific Reports*, 10(1):1–11, 2020.
- [4] Analog devices aducm350. Accessed: 2021-07-21.
- [5] Pasquale Arpaia, Davide Cuneo, Sabrina Grassini, Francesca Mancino, Simone Minucci, Nicola Moccaldi, and Isabella Sannino. A finite element model of abdominal human tissue for improving the accuracy in insulin absorption assessment: A feasibility study. *Measurement: Sensors*, 18:100218, 2021.
- [6] Pasquale Arpaia, Davide Cuneo, Francesca Mancino, Simone Minucci, Nicola Moccaldi, and Isabella Sannino. Preliminary investigation of the impact of mechanical stresses on bioimpedance spectroscopy-based insuline bioavailability assessment. In *2021 International Workshop on Impedance Spectroscopy (IWIS)*, pages 52–55. IEEE, 2021.
- [7] Sherif S Morcos and Pravin K Patel. The vocabulary of dentofacial deformities. *Clinics in plastic surgery*, 34(3):589–599, 2007.
- [8] Nigel B Pitts, Kim R Ekstrand, and ICDAS Foundation. International caries detection and assessment system (icdas) and its international caries classification and management system (iccms)—methods for staging of the caries process and enabling dentists to manage caries. *Community dentistry and oral epidemiology*, 41(1):e41–e52, 2013.
- [9] Isabella Sannino, Emma Angelini, Marco Parvis, Pasquale Arpaia, and Sabrina Grassini. Impedance spectroscopy for monitoring sound teeth and carious

## References

---

- lesions. In *2022 IEEE International Instrumentation and Measurement Technology Conference (I2MTC)*, pages 1–5. IEEE, 2022.
- [10] Isabella Sannino, Luca Lombardo, Emma Angelini, Marco Parvis, Pasquale Arpaia, and Sabrina Grassini. Preliminary impedance spectroscopy study for carious lesions detection. In *2022 IEEE International Symposium on Medical Measurements and Applications (MeMeA)*, pages 1–6. IEEE, 2022.
- [11] Isabella Sannino, Leonardo Iannucci, Luca Lombardo, Marco Parvis, Allegra Comba, Pasquale Arpaia, Emma Angelini, and Sabrina Grassini. Impedance measurements for demineralized tooth lesions assessment. In *2023 IEEE International Symposium on Medical Measurements and Applications (MeMeA)*, pages 1–6. IEEE, 2023.
- [12] Sami Gabriel, RW Lau, and Camelia Gabriel. The dielectric properties of biological tissues: II. measurements in the frequency range 10 Hz to 20 GHz. *Physics in medicine & biology*, 41(11):2251, 1996.
- [13] Yu Wu, Dai Jiang, Andy Bardill, Serena De Gelidi, Richard Bayford, and Andreas Demosthenous. A high frame rate wearable EIT system using active electrode ASICs for lung respiration and heart rate monitoring. *IEEE Transactions on Circuits and Systems I: Regular Papers*, 65(11):3810–3820, 2018.
- [14] V Ju Mishlanov, AL Zuev, and Ya V Mishlanov. Development of medical sensor systems in pulmonology based on electrical impedance measurement. *Biophysics*, 67(6):1017–1022, 2022.
- [15] L Nescolarde, A Piccoli, A Román, A Nunez, R Morales, J Tamayo, T Doñate, and J Rosell. Bioelectrical impedance vector analysis in haemodialysis patients: relation between oedema and mortality. *Physiological measurement*, 25(5):1271, 2004.
- [16] Antonio Piccoli, Italian CAPD-BIA Study Group, et al. Bioelectric impedance vector distribution in peritoneal dialysis patients with different hydration status. *Kidney international*, 65(3):1050–1063, 2004.
- [17] Francesco William Guglielmi, Tecla Mastronuzzi, Lorena Pietrini, Alba Panarese, Carmine Panella, and Antonio Francavilla. The RxC graph in evaluating and monitoring fluid balance in patients with liver cirrhosis. *Annals of the New York Academy of Sciences*, 873(1):105–111, 1999.
- [18] Shing-Hong Liu, Da-Chuan Cheng, and Chun-Hung Su. A cuffless blood pressure measurement based on the impedance plethysmography technique. *Sensors*, 17(5):1176, 2017.
- [19] Anders Brahmé. *Comprehensive biomedical physics*. Newnes, 2014.

- [20] GD Jindal, SA Pedhnekar, SN Nerurkar, KL Masand, DK Gupta, HL Deshmukh, JP Bapu, and GB Parulkar. Diagnosis of venous disorders using impedance plethysmography. *Journal of postgraduate medicine*, 36(3):158, 1990.
- [21] Salim Kerai et al. The impedance cardiography technique in medical diagnosis. *Medical Technologies Journal*, 2(3):232–244, 2018.
- [22] Tushar Kanti Bera. Bioelectrical impedance methods for noninvasive health monitoring: a review. *Journal of medical engineering*, 2014, 2014.
- [23] Maurizio Marra, Barbara Da Prat, Concetta Montagnese, Annarita Caldara, Rosa Sammarco, Fabrizio Pasanisi, and Roberto Corsetti. Segmental bioimpedance analysis in professional cyclists during a three week stage race. *Physiological measurement*, 37(7):1035, 2016.
- [24] M Marra, A Caldara, C Montagnese, E De Filippo, F Pasanisi, F Contaldo, and L Scalfi. Bioelectrical impedance phase angle in constitutionally lean females, ballet dancers and patients with anorexia nervosa. *European journal of clinical nutrition*, 63(7):905–908, 2009.
- [25] Carrie Earthman, Diana Traughber, Jennifer Dobratz, and Wanda Howell. Bioimpedance spectroscopy for clinical assessment of fluid distribution and body cell mass. *Nutrition in Clinical Practice*, 22(4):389–405, 2007.
- [26] Ursula G Kyle, Ingvar Bosaeus, Antonio D De Lorenzo, Paul Deurenberg, Marinos Elia, José Manuel Gómez, Berit Lilienthal Heitmann, Luisa Kent-Smith, Jean-Claude Melchior, Matthias Pirlich, et al. Bioelectrical impedance analysis—part i: review of principles and methods. *Clinical nutrition*, 23(5):1226–1243, 2004.
- [27] Xian Huang, Woon-Hong Yeo, Yuhao Liu, and John A Rogers. Epidermal differential impedance sensor for conformal skin hydration monitoring. *Biointerphases*, 7(1):52, 2012.
- [28] Sylvie Verdier-Sévrain and Frédéric Bonté. Skin hydration: a review on its molecular mechanisms. *Journal of cosmetic dermatology*, 6(2):75–82, 2007.
- [29] Ulrik Birgersson, Erik Birgersson, Peter Åberg, Ingrid Nicander, and Stig Ollmar. Non-invasive bioimpedance of intact skin: mathematical modeling and experiments. *Physiological measurement*, 32(1):1, 2010.
- [30] Peter Åberg, Ulrik Birgersson, Peter Elsner, Peter Mohr, and Stig Ollmar. Electrical impedance spectroscopy and the diagnostic accuracy for malignant melanoma. *Experimental dermatology*, 20(8):648–652, 2011.
- [31] SL York, LC Ward, S Czerniec, MJ Lee, KM Refshauge, and SL Kilbreath. Single frequency versus bioimpedance spectroscopy for the assessment of lymphedema. *Breast cancer research and treatment*, 117:177–182, 2009.

## References

---

- [32] Zeynep Erdogan Iyigun, Derya Selamoglu, Gul Alco, Kezban Nur Pilanci, Cetin Ordu, Filiz Agacayak, Filiz Elbüken, Atilla Bozdogan, Serkan Ilgun, Fusun Guler Uysal, et al. Bioelectrical impedance for detecting and monitoring lymphedema in patients with breast cancer. preliminary results of the florence nightingale breast study group. *Lymphatic research and biology*, 13(1):40–45, 2015.
- [33] James J Ackmann and Martin A Seitz. Methods of complex impedance measurements in biologic tissue. *Critical reviews in biomedical engineering*, 11(4):281–311, 1984.
- [34] Leila Es Sebar, Leonardo Iannucci, Emma Angelini, Sabrina Grassini, and Marco Parvis. Electrochemical impedance spectroscopy system based on a teensy board. *IEEE Transactions on Instrumentation and Measurement*, 70:1–9, 2020.
- [35] Pasquale Arpaia, Fabrizio Clemente, Carmine Romanucci, and Antonio Zanesco. Experimental characterization of an eis-based method for low-invasive diagnosis of prosthesis osseointegration. In *XVIII IMEKO Word Congress, Rio de Janeiro (Brasil)*, pages 17–22, 2006.
- [36] Satoru Naito, Masato Hoshi, and Shin Yagihara. Microwave dielectric analysis of human stratum corneum in vivo. *Biochimica et Biophysica Acta (BBA)-General Subjects*, 1381(3):293–304, 1998.
- [37] Kyösti Kontturi, Lasse Murtomäki, Jouni Hirvonen, Petteri Paronen, and Arto Urtti. Electrochemical characterization of human skin by impedance spectroscopy: the effect of penetration enhancers. *Pharmaceutical research*, 10(3):381–385, 1993.
- [38] Sverre Grimnes and Orjan G Martinsen. Cole electrical impedance model—a critique and an alternative. *IEEE transactions on biomedical engineering*, 52(1):132–135, 2004.
- [39] Ulrik Hans Birgersson, Erik Birgersson, and Stig Ollmar. Estimating electrical properties and the thickness of skin with electrical impedance spectroscopy: Mathematical analysis and measurements. *Journal of Electrical Bioimpedance*, 3(1):51–60, 2012.
- [40] Letizia Ventrelli, Lucanos Marsilio Strambini, and Giuseppe Barillaro. Microneedles for transdermal biosensing: current picture and future direction. *Advanced healthcare materials*, 4(17):2606–2640, 2015.
- [41] Owen G Jepps, Yuri Dancik, Yuri G Anissimov, and Michael S Roberts. Modeling the human skin barrier—towards a better understanding of dermal absorption. *Advanced drug delivery reviews*, 65(2):152–168, 2013.
- [42] Sonja Huclova, Dirk Baumann, Mark S Talary, and Jürg Fröhlich. Sensitivity and specificity analysis of fringing-field dielectric spectroscopy applied to a

- multi-layer system modelling the human skin. *Physics in Medicine & Biology*, 56(24):7777, 2011.
- [43] JB Phipps, RV Padmanabhan, and GA Lattin. Transport of ionic species through skin. *Solid State Ionics*, 28:1778–1783, 1988.
- [44] Jim E Riviere and Mark C Heit. Electrically-assisted transdermal drug delivery. *Pharmaceutical research*, 14(6):687–697, 1997.
- [45] Tatsuma Yamamoto and Yoshitake Yamamoto. Electrical properties of the epidermal stratum corneum. *Medical and biological engineering*, 14(2):151–158, 1976.
- [46] Nagahiro H Yoshida and Michael S Roberts. Solute molecular size and transdermal iontophoresis across excised human skin. *Journal of controlled release*, 25(3):177–195, 1993.
- [47] Vicente Aguilera, Marina Belaya, and Victor Levadny. Passive transport of small ions through human stratum corneum. *Journal of controlled release*, 44(1):11–18, 1997.
- [48] Ajay K Banga and Yie W Chien. Iontophoretic delivery of drugs: fundamentals, developments and biomedical applications. *Journal of Controlled Release*, 7(1):1–24, 1988.
- [49] Diabetes Atlas et al. International diabetes federation. *IDF Diabetes Atlas, 7th edn. Brussels, Belgium: International Diabetes Federation*, 2015.
- [50] Cheng Chen, Xue-Ling Zhao, Zhan-Hong Li, Zhi-Gang Zhu, Shao-Hong Qian, and Andrew J Flewitt. Current and emerging technology for continuous glucose monitoring. *Sensors*, 17(1):182, 2017.
- [51] Peter B Lippa, Carolin Müller, Alice Schlichtiger, and Harald Schlebusch. Point-of-care testing (poc): Current techniques and future perspectives. *TrAC Trends in Analytical Chemistry*, 30(6):887–898, 2011.
- [52] Airat K Amerov, Jun Chen, Gary W Small, and Mark A Arnold. Scattering and absorption effects in the determination of glucose in whole blood by near-infrared spectroscopy. *Analytical chemistry*, 77(14):4587–4594, 2005.
- [53] Suresh N Thennadil, Jessica L Rennert, Brian J Wenzel, Kevin H Hazen, Timothy L Ruchti, and Marshall B Block. Comparison of glucose concentration in interstitial fluid, and capillary and venous blood during rapid changes in blood glucose levels. *Diabetes Technology & Therapeutics*, 3(3):357–365, 2001.
- [54] Sandeep Kumar Vashist. Non-invasive glucose monitoring technology in diabetes management: A review. *Analytica chimica acta*, 750:16–27, 2012.

## References

---

- [55] HM Heise and R Marbach. Human oral mucosa studies with varying blood glucose concentration by non-invasive atr-ft-ir-spectroscopy. *Cellular and molecular biology (Noisy-le-Grand, France)*, 44(6):899–912, 1998.
- [56] Boris P Kovatchev, Linda A Gonder-Frederick, Daniel J Cox, and William L Clarke. Evaluating the accuracy of continuous glucose-monitoring sensors: continuous glucose–error grid analysis illustrated by the sense freestyle navigator data. *Diabetes Care*, 27(8):1922–1928, 2004.
- [57] Dachao Li, Zhihua Pu, Wenshuai Liang, Tongkun Liu, Ridong Wang, Haixia Yu, and Kexin Xu. Non-invasive measurement of normal skin impedance for determining the volume of the transdermally extracted interstitial fluid. *Measurement*, 62:215–221, 2015.
- [58] Jajang Juansah and Wina Yulianti. Studies on electrical behavior of glucose using impedance spectroscopy. In *IOP Conference Series: Earth and Environmental Science*, volume 31, page 012039. IOP Publishing, 2016.
- [59] Jingzhen Li, Tobore Igbe, Yuhang Liu, Zedong Nie, Wenjian Qin, Lei Wang, and Yang Hao. An approach for noninvasive blood glucose monitoring based on bioimpedance difference considering blood volume pulsation. *IEEE Access*, 6:51119–51129, 2018.
- [60] Harvey N Mayrovitz, Aldene McClymont, and Naushira Pandya. Skin tissue water assessed via tissue dielectric constant measurements in persons with and without diabetes mellitus. *Diabetes technology & therapeutics*, 15(1):60–65, 2013.
- [61] Harvey N Mayrovitz, Irina Volosko, Bansari Sarkar, and Naushira Pandya. Arm, leg, and foot skin water in persons with diabetes mellitus (dm) in relation to hba1c assessed by tissue dielectric constant (tdc) technology measured at 300 mhz. *Journal of diabetes science and technology*, 11(3):584–589, 2017.
- [62] Rangadhar Pradhan, Analava Mitra, and Soumen Das. Quantitative evaluation of blood glucose concentration using impedance sensing devices. *Journal of Electrical Bioimpedance*, 4(1):73–77, 2013.
- [63] Andreas Caduff, Etienne Hirt, Yu Feldman, Zulfiqur Ali, and Lutz Heinemann. First human experiments with a novel non-invasive, non-optical continuous glucose monitoring system. *Biosensors and Bioelectronics*, 19(3):209–217, 2003.
- [64] Stuart Alan Weinzimer. Analysis: Pendra: the once and future noninvasive continuous glucose monitoring device? *Diabetes technology & therapeutics*, 6(4):442–444, 2004.
- [65] Ghazzi Dorsaf, Manai Yacine, Nouri Khaled, et al. Non-invasive glucose monitoring: application and technologies. *Curr Trends Biomed Eng Biosci*, 14(1):555878, 2018.

## References

---

- [66] Kenneth R Pitzer, Shashi Desai, Tim Dunn, Steve Edelman Yalia Jayalakshmi, John Kennedy, Janet A Tamada, and Russell O Potts. Detection of hypoglycemia with the glucoWatch biographer. *Clinical Diabetology*, 2(4):307–314, 2001.
- [67] MJ Tierney, JA Tamada, RO Potts, L Jovanovic, S Garg, Cygnus Research Team, et al. Clinical evaluation of the glucoWatch® biographer: a continual, non-invasive glucose monitor for patients with diabetes. *Biosensors and Bioelectronics*, 16(9-12):621–629, 2001.
- [68] Spencer L James, Degu Abate, Kalkidan Hassen Abate, Solomon M Abay, Cristiana Abbafati, Nooshin Abbasi, Hedayat Abbastabar, Foad Abd-Allah, Jemal Abdela, Ahmed Abdelalim, et al. Global, regional, and national incidence, prevalence, and years lived with disability for 354 diseases and injuries for 195 countries and territories, 1990–2017: a systematic analysis for the global burden of disease study 2017. *The Lancet*, 392(10159):1789–1858, 2018.
- [69] Nityanand Jain, Upasna Dutt, Igor Radenkov, and Shivani Jain. Who’s global oral health status report 2022: Actions, discussion, & implementation.
- [70] Milica Jevdjevic and Stefan Listl. Economic impacts of oral diseases in 2019 - data for 194 countries, 2022.
- [71] EAM Kidd and Ole Fejerskov. What constitutes dental caries? histopathology of carious enamel and dentin related to the action of cariogenic biofilms. *Journal of dental research*, 83(1\_suppl):35–38, 2004.
- [72] AGR Targino, A Rosenblatt, AF Oliveira, AMB Chaves, and VE Santos. The relationship of enamel defects and caries: a cohort study. *Oral diseases*, 17(4):420–426, 2011.
- [73] NJ Cochrane, F Cai, NL Huq, MF Burrow, and EC Reynolds. New approaches to enhanced remineralization of tooth enamel. *Journal of dental research*, 89(11):1187–1197, 2010.
- [74] Sea Wongkhantee, V Patanapiradej, C Maneenut, and D Tantbirojn. Effect of acidic food and drinks on surface hardness of enamel, dentine, and tooth-coloured filling materials. *Journal of dentistry*, 34(3):214–220, 2006.
- [75] Damiano Pasqualini, Nicola Scotti, Livio Mollo, Elio Berutti, Emma Angelini, Giuseppe Migliaretti, Annamaria Cuffini, and Daniel Adlerstein. Microbial leakage of gutta-percha and resilon™ root canal filling material: A comparative study using a new homogeneous assay for sequence detection. *Journal of Biomaterials Applications*, 22(4):337–352, 2008.
- [76] GR de Sant’Anna, EB Nascimento, AG Higa, EAP Santos, AM Espirito Santo, and AA Martín. Ft raman spectroscopy in the study of human teeth under medications demineralization. In *Biophotonics South America*, volume 9531, pages 427–440. SPIE, 2015.

## References

---

- [77] Clifton M Carey. Tooth whitening: what we now know. *Journal of Evidence Based Dental Practice*, 14:70–76, 2014.
- [78] John Hicks, Franklin Garcia-Godoy, and Catherine Flaitz. Biological factors in dental caries: role of remineralization and fluoride in the dynamic process of demineralization and remineralization (part 3). *Journal of Clinical Pediatric Dentistry*, 28(3):203–214, 2004.
- [79] WM Thomson. Dental caries experience in older people over time: what can the large cohort studies tell us? *British dental journal*, 196(2):89–92, 2004.
- [80] Petros Foros, Elissaios Oikonomou, Despina Koletsi, and Christos Rahiotis. Detection methods for early caries diagnosis: A systematic review and meta-analysis. *Caries Research*, 55(4):247–259, 2021.
- [81] Friederike Litzenburger, Gerrit Schäfer, Reinhard Hickel, Jan Kühnisch, and Katrin Heck. Comparison of novel and established caries diagnostic methods: a clinical study on occlusal surfaces. *BMC Oral Health*, 21(1):1–10, 2021.
- [82] GVA Topping and NB Pitts. Clinical visual caries detection. *Detection, assessment, diagnosis and monitoring of caries*, 21:15–41, 2009.
- [83] Falk Schwendicke, Markus Tzschope, and Sebastian Paris. Radiographic caries detection: a systematic review and meta-analysis. *Journal of dentistry*, 43(8):924–933, 2015.
- [84] EA Kidd and NB Pitts. A reappraisal of the value of the bitewing radiograph in the diagnosis of posterior approximal caries. *British dental journal*, 169(7):195–200, 1990.
- [85] Othman Mahmoud Yassin. In vitro studies of the effect of a dental explorer on the formation of an artificial carious lesion. *ASDC journal of dentistry for children*, 62(2):111–117, 1995.
- [86] E Beltrami, L da Costa Silveira, and RC Perretto. The effect of the exploratory probe on demineralized enamel. *Dens*, 6(1-2):1–4, 1990.
- [87] Amid I Ismail, Woosung Sohn, Marisol Tellez, Ashley Amaya, Ananda Sen, Hana Hasson, and Nigel B Pitts. The international caries detection and assessment system (icdas): an integrated system for measuring dental caries. *Community dentistry and oral epidemiology*, 35(3):170–178, 2007.
- [88] Adejumo A Adeyemi, Fadi D Jarad, Gleb N Komarov, Neil Pender, and Susan M Higham. Assessing caries removal by undergraduate dental students using quantitative light-induced fluorescence. *Journal of Dental Education*, 72(11):1318–1323, 2008.
- [89] Marwa Abdelaziz, Ivo Krejci, Thomas Perneger, Albert Feilzer, and Lydia Vazquez. Near infrared transillumination compared with radiography to detect and monitor proximal caries: A clinical retrospective study. *Journal of dentistry*, 70:40–45, 2018.



- 
- [90] Madhumitha Mohanraj, V Ratna Prabhu, R Senthil, et al. Diagnostic methods for early detection of dental caries-a review. *International Journal of Pedodontic Rehabilitation*, 1(1):29, 2016.
- [91] C Longbottom and M-CDNJM Huysmans. Electrical measurements for use in caries clinical trials. *Journal of Dental Research*, 83(1\_suppl):76–79, 2004.
- [92] Patrick J Carrigan, Donald R Morse, M Lawrence Furst, and Irving H Sinai. A scanning electron microscopic evaluation of human dentinal tubules according to age and location. *Journal of endodontics*, 10(8):359–363, 1984.
- [93] PF Ashley, AS Blinkhorn, and RM Davies. Occlusal caries diagnosis: an in vitro histological validation of the electronic caries monitor (ecm) and other methods. *Journal of dentistry*, 26(2):83–88, 1998.
- [94] Nelly Pradelle-Plasse, François Wenger, and Pierre Colon. Effect of conditioners on dentin permeability using an impedance method. *Journal of dentistry*, 30(5-6):251–257, 2002.
- [95] Mihai Andrei, Cristian Pirvu, and Ioana Demetrescu. Electrochemical impedance spectroscopy in understanding the influence of ultrasonic dental scaling on the dental structure–dental filling interface. *European journal of oral sciences*, 122(6):411–416, 2014.
- [96] Nicola Scotti, Allegra Comba, Milena Cadenaro, Luca Fontanive, Lorenzo Breschi, Carlo Monaco, and Roberto Scotti. Effect of lithium disilicate veneers of different thickness on the degree of conversion and microhardness of a light-curing and a dual-curing cement. *The International journal of prosthodontics*, 29(4):384–388, 2016.
- [97] Cochrane Oral Health Group, Richard Macey, Tanya Walsh, Philip Riley, Anne-Marie Glenn, Helen V Worthington, Janet E Clarkson, and David Ricketts. Electrical conductance for the detection of dental caries. *Cochrane Database of Systematic Reviews*, 2021(12), 1996.
- [98] David Nigel James Ricketts, Edwina Anne Maria Kidd, and Ronald Frederick Wilson. Electronic diagnosis of occlusal caries in vitro: adaptation of the technique for epidemiological purposes. *Community dentistry and oral epidemiology*, 25(3):238–241, 1997.
- [99] DF Cortes, RP Ellwood, and KR Ekstrand. An in vitro comparison of a combined foti/visual examination of occlusal caries with other caries diagnostic methods and the effect of stain on their diagnostic performance. *Caries research*, 37(1):8–16, 2003.
- [100] RP Ellwood and DF Cortes. In vitro assessment of methods of applying the electrical caries monitor for the detection of occlusal caries. *Caries research*, 38(1):45–53, 2004.

## References

---

- [101] Joshua Eric Cohen. *The association between CarieScan Pro readings and histologic depth of caries in non cavitated occlusal lesion in vitro*. The University of Iowa, 2013.
- [102] Diana Mortensen, Katrine Dannemand, Svante Twetman, and Mette Kirstine Keller. Detection of non-cavitated occlusal caries with impedance spectroscopy and laser fluorescence: an in vitro study. *The open dentistry journal*, 8:28, 2014.
- [103] Diana Mortensen, Ilse Helsing-Olsen, Kim Rud Ekstrand, and Svante Twetman. In-vivo performance of impedance spectroscopy, laser fluorescence, and bitewing radiographs for occlusal caries detection. *Quintessence Int*, 49(4):293–299, 2018.
- [104] Giovanni Annuzzi, Pasquale Arpaia, Umberto Cesaro, Ornella Cuomo, Mirco Frosolone, Sabrina Grassini, Nicola Moccaldi, and Isabella Sannino. A customized bioimpedance meter for monitoring insulin bioavailability. In *2020 IEEE International Instrumentation and Measurement Technology Conference (I2MTC)*, pages 1–5. IEEE, 2020.
- [105] Pasquale Arpaia, Federica Crauso, Sabrina Grassini, Simone Minucci, Nicola Moccaldi, and Isabella Sannino. Preliminary experimental identification of a fem human knee model. In *2020 IEEE International Symposium on Medical Measurements and Applications (MeMeA)*, pages 1–6. IEEE, 2020.
- [106] Ananda Basu, Simmi Dube, Michael Slama, Isabel Errazuriz, Jose Carlos Amezcua, Yogish C Kudva, Thomas Peyser, Rickey E Carter, Claudio Cobelli, and Rita Basu. Time lag of glucose from intravascular to interstitial compartment in humans. *Diabetes*, 62(12):4083–4087, 2013.
- [107] B Shashaj, E Busetto, and N Sulli. Benefits of a bolus calculator in pre-and postprandial glycaemic control and meal flexibility of paediatric patients using continuous subcutaneous insulin infusion (csii). *Diabetic Medicine*, 25(9):1036–1042, 2008.
- [108] Robert J Young, W James Hannan, Brian M Frier, Judith M Steel, and Leslie JP Duncan. Diabetic lipohypertrophy delays insulin absorption. *Diabetes Care*, 7(5):479–480, 1984.
- [109] Thomas S Morley, Jonathan Y Xia, and Philipp E Scherer. Selective enhancement of insulin sensitivity in the mature adipocyte is sufficient for systemic metabolic improvements. *Nature communications*, 6(1):1–11, 2015.
- [110] Shein-Chung Chow. Bioavailability and bioequivalence in drug development. *Wiley Interdisciplinary Reviews: Computational Statistics*, 6(4):304–312, 2014.
- [111] Claudio Cobelli, Eric Renard, and Boris Kovatchev. Artificial pancreas: past, present, future. *Diabetes*, 60(11):2672–2682, 2011.

- [112] Chao Tan, Shiwei Liu, Jiabin Jia, and Feng Dong. A wideband electrical impedance tomography system based on sensitive bioimpedance spectrum bandwidth. *IEEE Transactions on Instrumentation and Measurement*, 69(1):144–154, 2019.
- [113] John-Jairo Cabrera-López and Jaime Velasco-Medina. Structured approach and impedance spectroscopy microsystem for fractional-order electrical characterization of vegetable tissues. *IEEE Transactions on Instrumentation and Measurement*, 69(2):469–478, 2019.
- [114] Pasquale Arpaia, Umberto Cesaro, and Nicola Moccaldi. Noninvasive measurement of transdermal drug delivery by impedance spectroscopy. *Scientific Reports*, 7:44647, 2017.
- [115] Pasquale Arpaia, Ornella Cuomo, Nicola Moccaldi, Alessandra Smarra, and Maurizio Tagliatalata. Non-invasive real-time in-vivo monitoring of insulin absorption from subcutaneous tissues. In *Journal of Physics: Conference Series*, volume 1065, page 132008. IOP Publishing, 2018.
- [116] Fiab pg500 disposable gelled electrodes. Accessed: 2021-06-28.
- [117] Analog Devices Inc. Eval-aducm350 evaluation board; <http://www.analog.com/en/design-center/evaluation-hardware-and-software/evaluation-boards-kits/eval-aducm350.html>.
- [118] International Electrotechnical Commission. *IEC 60601-2-33 Medical Electrical Equipment-Part I*, volume 2. 2001.
- [119] Paul De Bièvre. The 2012 international vocabulary of metrology:“vim”. *Accreditation and Quality Assurance*, 17(2):231–232, 2012.
- [120] Bernard Rigaud, Jean-Pierre Morucci, and Nicolas Chauveau. Bioelectrical impedance techniques in medicine part i: bioimpedance measurement second section: impedance spectrometry. *Critical Reviews™ in Biomedical Engineering*, 24(4-6), 1996.
- [121] Long Wu, Yukiharu Ogawa, and Akio Tagawa. Electrical impedance spectroscopy analysis of eggplant pulp and effects of drying and freezing–thawing treatments on its impedance characteristics. *Journal of Food Engineering*, 87(2):274–280, 2008.
- [122] Nabila Sekkat, Yogeshvar N Kalia, and Richard H Guy. Biophysical study of porcine ear skin in vitro and its comparison to human skin in vivo. *Journal of pharmaceutical sciences*, 91(11):2376–2381, 2002.
- [123] Jennifer E Seto, Baris E Polat, Renata FV Lopez, Daniel Blankschtein, and Robert Langer. Effects of ultrasound and sodium lauryl sulfate on the transdermal delivery of hydrophilic permeants: Comparative in vitro studies with full-thickness and split-thickness pig and human skin. *Journal of Controlled Release*, 145(1):26–32, 2010.

## References

---

- [124] Fritz P Schmook, Josef G Meingassner, and Andreas Billich. Comparison of human skin or epidermis models with human and animal skin in in-vitro percutaneous absorption. *International journal of pharmaceutics*, 215(1):51–56, 2001.
- [125] Jingyun Yuan, Yan Chen, Yanting Xuan, Lihong Cao, Jing Zhu, Fenrong Wang, Xiaona Zhou, Qing Ye, Liping Liao, Yun Zheng, et al. Can the upper inner side of the thigh become a new option for insulin injection? *Current Medical Research and Opinion*, 32(7):1319–1324, 2016.
- [126] Christian Binder, Torsten Lauritzen, Ole Faber, and Stig Pramming. Insulin pharmacokinetics. *Diabetes care*, 7(2):188–199, 1984.
- [127] M Berger, HJ Cüppers, H Hegner, V Jörgens, and P Berchtold. Absorption kinetics and biologic effects of subcutaneously injected insulin preparations. *Diabetes Care*, 5(2):77–91, 1982.
- [128] Ramesh Sharma Poudel, Shakti Shrestha, Rano Mal Piryani, Bijaya Basyal, Kalpana Kaucha, and Shital Adhikari. Assessment of insulin injection practice among diabetes patients in a tertiary healthcare centre in nepal: a preliminary study. *Journal of diabetes research*, 2017, 2017.
- [129] Laurence Hirsch, Karen Byron, and Michael Gibney. Intramuscular risk at insulin injection sites—measurement of the distance from skin to muscle and rationale for shorter-length needles for subcutaneous insulin therapy. *Diabetes Technology & Therapeutics*, 16(12):867–873, 2014.
- [130] Christopher Rini, Bruce C Roberts, Didier Morel, Rick Klug, Benjamin Selvage, and Ronald J Pettis. Evaluating the impact of human factors and pen needle design on insulin pen injection. *Journal of diabetes science and technology*, 13(3):533–545, 2019.
- [131] Mahdi Halabian, Borhan Beigzadeh, Alireza Karimi, Hadi Asgharzadeh Shirazi, and Mohammad Hasan Shaali. A combination of experimental and finite element analyses of needle–tissue interaction to compute the stresses and deformations during injection at different angles. *Journal of clinical monitoring and computing*, 30(6):965–975, 2016.
- [132] Abbas Samani, Judit Zubovits, and Donald Plewes. Elastic moduli of normal and pathological human breast tissues: an inversion-technique-based investigation of 169 samples. *Physics in medicine & biology*, 52(6):1565, 2007.
- [133] Kang Hee Sim, Moon Sook Hwang, Sun Young Kim, Hye Mi Lee, Ji Yeun Chang, and Moon Kyu Lee. The appropriateness of the length of insulin needles based on determination of skin and subcutaneous fat thickness in the abdomen and upper arm in patients with type 2 diabetes. *Diabetes & metabolism journal*, 38(2):120, 2014.

- 
- [134] Donatella Lo Presti, Carmela Ingegnosi, and Kenneth Strauss. Skin and subcutaneous thickness at injecting sites in children with diabetes: ultrasound findings and recommendations for giving injection. *Pediatric diabetes*, 13(7):525–533, 2012.
- [135] Michael A Gibney, Christina H Arce, Karen J Byron, and Laurence J Hirsch. Skin and subcutaneous adipose layer thickness in adults with diabetes at sites used for insulin injections: implications for needle length recommendations. *Current medical research and opinion*, 26(6):1519–1530, 2010.
- [136] Gabrielle Rankin, Maria Stokes, and Dianne J Newham. Abdominal muscle size and symmetry in normal subjects. *Muscle & Nerve: Official Journal of the American Association of Electrodiagnostic Medicine*, 34(3):320–326, 2006.
- [137] A Chawla, S Mukherjee, and B Karthikeyan. Mechanical properties of soft tissues in the human chest, abdomen and upper extremities. *Institution of Engineers, J. Mechanical Engineering*, 2006.
- [138] Flaminio Fidanza, Ancel Keys, and Joseph T Anderson. Density of body fat in man and other mammals. *Journal of Applied Physiology*, 6(4):252–256, 1953.
- [139] Samuel R Ward and Richard L Lieber. Density and hydration of fresh and fixed human skeletal muscle. *Journal of biomechanics*, 38(11):2317–2320, 2005.
- [140] Rakshita Panchal, Luke Horton, Peyman Poozesh, Javad Baqersad, and Mohammadreza Nasiriavanaki. Vibration analysis of healthy skin: toward a noninvasive skin diagnosis methodology. *Journal of biomedical optics*, 24(1):015001, 2019.
- [141] C.O. Flynn. The design and validation of a multi-layer model of human skin. *PhD Thesis*, 2007.
- [142] A. Dyachenko, M.V. Veremyeva, and E.S. Fomina. Elasticity and viscosity of surface tissues of the human chest wall. *Russian Journal of Biomechanics*, 21:164–174, 01 2017.
- [143] Kenneth S Cole and Robert H Cole. Dispersion and absorption in dielectrics i. alternating current characteristics. *The Journal of chemical physics*, 9(4):341–351, 1941.
- [144] Andrzej Kraszewski, Maria A Stuchly, and Stanislaw S Stuchly. A calibration method for measurements of dielectric properties. *IEEE Transactions on Instrumentation and Measurement*, 32(2):385–387, 1983.
- [145] Mohammad-Reza Tofghi and Afshin S Daryoush. Biological tissue complex permittivity measured from  $s_{21}$ —error analysis and error reduction by reference measurements. *IEEE Transactions on Instrumentation and Measurement*, 58(7):2316–2327, 2009.

## References

---

- [146] Damijan Miklavčič, Nataša Pavšelj, and Francis X Hart. Electric properties of tissues. *Wiley encyclopedia of biomedical engineering*, 2006.
- [147] Yu-Fen Chen, Xuan-Yi Huang, Ching-Hui Chien, and Jui-Fen Cheng. The effectiveness of diaphragmatic breathing relaxation training for reducing anxiety. *Perspectives in psychiatric care*, 53(4):329–336, 2017.
- [148] Antonio Nanci. *Ten Cate's Oral Histology-e-book: development, structure, and function*. Elsevier Health Sciences, 2017.
- [149] Bin Yu, Jin-Soo Ahn, and Yong-Keun Lee. Measurement of translucency of tooth enamel and dentin. *Acta Odontologica Scandinavica*, 67(1):57–64, 2009.
- [150] Tsuneyuki Yamamoto, Tomoka Hasegawa, Tomomaya Yamamoto, Hiromi Hongo, and Norio Amizuka. Histology of human cementum: Its structure, function, and development. *Japanese dental science review*, 52(3):63–74, 2016.
- [151] Mousa G Ghannam, Hania Alameddine, and Bruno Bordoni. Anatomy, head and neck, pulp (tooth). In *StatPearls [Internet]*. StatPearls Publishing, 2021.
- [152] Ensanya Ali Abou Neel, Anas Aljabo, Adam Strange, Salwa Ibrahim, Melanie Coathup, Anne M Young, Laurent Bozec, and Vivek Mudera. Demineralization–remineralization dynamics in teeth and bone. *International journal of nanomedicine*, 11:4743, 2016.
- [153] Adele L Boskey, Marian F Young, Tina Kilts, and Kostas Verdelis. Variation in mineral properties in normal and mutant bones and teeth. *Cells Tissues Organs*, 181(3-4):144–153, 2005.
- [154] Paola Fattibene and Freddy Callens. Epr dosimetry with tooth enamel: a review. *Applied Radiation and Isotopes*, 68(11):2033–2116, 2010.
- [155] Nigel B Pitts, Domenick T Zero, Phil D Marsh, Kim Ekstrand, Jane A Weintraub, Francisco Ramos-Gomez, Junji Tagami, Svante Twetman, Georgios Tsakos, and Amid Ismail. Dental caries. *Nature reviews Disease primers*, 3(1):1–16, 2017.
- [156] Nobuhiro Takahashi. Microbial ecosystem in the oral cavity: metabolic diversity in an ecological niche and its relationship with oral diseases. In *International Congress Series*, volume 1284, pages 103–112. Elsevier, 2005.
- [157] Vincent Zijngje, M Barbara M Van Leeuwen, John E Degener, Frank Abbas, Thomas Thurnheer, Rudolf Gmür, and Hermie J M. Harmsen. Oral biofilm architecture on natural teeth. *PloS one*, 5(2):e9321, 2010.
- [158] Neeraj Gugnani, IK Pandit, Nikhil Srivastava, Monika Gupta, and Megha Sharma. International caries detection and assessment system (icdas): a new concept. *International journal of clinical pediatric dentistry*, 4(2):93, 2011.

- [159] DJ White. The application of in vitro models to research on demineralization and remineralization of the teeth. *Advances in dental research*, 9(3):175–193, 1995.
- [160] JH Meurman and RM Frank. Progression and surface ultrastructure of in vitro caused erosive lesions in human and bovine enamel. *Caries research*, 25(2):81–87, 1991.
- [161] Jing Xue, Wei Li, and Michael V Swain. In vitro demineralization of human enamel natural and abraded surfaces: A micromechanical and sem investigation. *Journal of dentistry*, 37(4):264–272, 2009.
- [162] Achim Walter Hassel, Koji Fushimi, and Masahiro Seo. An agar-based silver/silver chloride reference electrode for use in micro-electrochemistry. *Electrochemistry communications*, 1(5):180–183, 1999.
- [163] Derrick Butler, Nishit Goel, Lindsey Goodnight, Srinivas Tadigadapa, and Aida Ebrahimi. Detection of bacterial metabolism in lag-phase using impedance spectroscopy of agar-integrated 3d microelectrodes. *Biosensors and Bioelectronics*, 129:269–276, 2019.
- [164] Agnieszka Sobczak-Kupiec, Ewa Olender, Dagmara Malina, and Bożena Tyliszczak. Effect of calcination parameters on behavior of bone hydroxyapatite in artificial saliva and its biosafety. *Materials Chemistry and Physics*, 206:158–165, 2018.
- [165] Christopher MA Brett, Iulia Ioanitorescu, and Florin Trandafir. Influence of the biological fluid on the corrosion of dental amalgam. *Corrosion Science*, 46(11):2803–2816, 2004.
- [166] Norbert Herencsar, Todd J Freeborn, Aslihan Kartci, and Oguzhan Cicekoglu. A comparative study of two fractional-order equivalent electrical circuits for modeling the electrical impedance of dental tissues. *Entropy*, 22(10):1117, 2020.
- [167] Jui-Hsiung Huang, Shi-Chern Yen, and Chun-Pin Lin. Impedance characteristics of mimic human tooth root canal and its equivalent circuit model. *Journal of The Electrochemical Society*, 155(5):P51, 2008.
- [168] Sverre Holm, Thomas Holm, and Ørjan Grøttem Martinsen. Simple circuit equivalents for the constant phase element. *PLoS One*, 16(3):e0248786, 2021.
- [169] M Levinkind, TJ Vandernooti, and JC Elliott. Electrochemical impedance characterization of human and bovine enamel. *Journal of Dental Research*, 69(12):1806–1811, 1990.
- [170] M Levinkind, TJ Vandernoot, and JC Elliott. Evaluation of smear layers on serial sections of human dentin by means of electrochemical impedance measurements. *Journal of dental research*, 71(3):426–433, 1992.

## References

---

- [171] AP Morais, AV Pino, and MN Souza. Detection of questionable occlusal carious lesions using an electrical bioimpedance method with fractional electrical model. *Review of Scientific Instruments*, 87(8):084305, 2016.
- [172] Andréa Pereira Morais, Alexandre Visintainer Pino, and Marcio Nogueira Souza. Assessment of tooth structure using an alternative electrical bioimpedance spectroscopy method. *Brazilian dental journal*, 25:146–152, 2014.
- [173] Celso Silva Queiroz, Anderson Takeo Hara, Adriana Franco Paes Leme, and Jaime Aparecido Cury. ph-cycling models to evaluate the effect of low fluoride dentifrice on enamel de- and remineralization. *Brazilian Dental Journal*, 19:21–27, 2008.
- [174] Iulian Otel. Overall review on recent applications of raman spectroscopy technique in dentistry. *Quantum Beam Science*, 7(1):5, 2023.
- [175] Pavel Matousek and Michael Morris. Emerging raman applications and techniques in biomedical and pharmaceutical fields. 2010.
- [176] Shanmugasundaram Kumaravel. Monitoring of fracture healing by electrical conduction: A new diagnostic procedure. *Indian journal of orthopaedics*, 46:384–390, 2012.
- [177] Giuseppe Pezzotti, Tetsuya Adachi, Isabella Gasparutti, Giulio Vincini, Wenliang Zhu, Marco Boffelli, Alfredo Rondinella, Elia Marin, Hiroaki Ichioka, Toshiro Yamamoto, et al. Vibrational monitor of early demineralization in tooth enamel after in vitro exposure to phosphoric liquid. *Spectrochimica Acta Part A: Molecular and Biomolecular Spectroscopy*, 173:19–33, 2017.
- [178] Sheila Regina Maia Braga, Dalva Lúcia Araújo De Faria, Elisabeth De Oliveira, and Maria Angela Pita Sobral. Morphological and mineral analysis of dental enamel after erosive challenge in gastric juice and orange juice. *Microscopy Research and Technique*, 74(12):1083–1087, 2011.
- [179] Leila Es Sebar, Emma Angelini, Andrea Baldi, Allegra Comba, Marco Parvis, and Sabrina Grassini. Nanoindentation and raman spectroscopy measurements on dual-cure luting cement for dental conservative restoration. In *2022 IEEE International Symposium on Medical Measurements and Applications (MeMeA)*, pages 1–6. IEEE, 2022.
- [180] Sabrina Grassini, Leila Es Sebar, Andrea Baldi, Allegra Comba, Emma Angelini, and Elio Berutti. Measurements for restorative dentistry: shrinkage and conversion degree of bulk-fill composites. In *2022 IEEE International Symposium on Medical Measurements and Applications (MeMeA)*, pages 1–6. IEEE, 2022.
- [181] Elia Marin, Noriko Hiraishi, Taigi Honma, Francesco Boschetto, Matteo Zanocco, Wenliang Zhu, Tetsuya Adachi, Narisato Kanamura, Toshiro Yamamoto, and Giuseppe Pezzotti. Raman spectroscopy for early detection and



- monitoring of dentin demineralization. *Dental Materials*, 36(12):1635–1644, 2020.
- [182] Tattiana Enrich-Essvein, Cristina Benavides-Reyes, Pedro Álvarez-Lloret, María Victoria Bolaños-Carmona, Alejandro B Rodríguez-Navarro, and Santiago González-López. Influence of de-remineralization process on chemical, microstructural, and mechanical properties of human and bovine dentin. *Clinical Oral Investigations*, 25:841–849, 2021.
- [183] Giovanna Orsini, Giulia Orilisi, Valentina Notarstefano, Riccardo Monterubbianesi, Flavia Vitiello, Vincenzo Tosco, Alessia Belloni, Angelo Putignano, and Elisabetta Giorgini. Vibrational imaging techniques for the characterization of hard dental tissues: From bench-top to chair-side. *Applied Sciences*, 11(24):11953, 2021.
- [184] Changqi Xu, Rachel Reed, Jeffrey P Gorski, Yong Wang, and Mary P Walker. The distribution of carbonate in enamel and its correlation with structure and mechanical properties. *Journal of materials science*, 47:8035–8043, 2012.
- [185] Paul HC Eilers and Hans FM Boelens. Baseline correction with asymmetric least squares smoothing. *Leiden University Medical Centre Report*, 1(1):5, 2005.
- [186] Agnieszka Martyna, Alicja Menzyk, Alessandro Damin, Aleksandra Michalska, Gianmario Martra, Eugenio Alladio, and Grzegorz Zadora. Improving discrimination of raman spectra by optimising preprocessing strategies on the basis of the ability to refine the relationship between variance components. *Chemometrics and Intelligent Laboratory Systems*, 202:104029, 2020.
- [187] Gianmaria F Ferrazzano, Ivana Amato, Tiziana Cantile, Giancarla Sangianantoni, and Aniello Ingenito. In vivo remineralising effect of gc tooth mousse on early dental enamel lesions: Sem analysis. *International dental journal*, 61(4):210–216, 2011.
- [188] María Melo, José Luis Sanz, Leopoldo Forner, Francisco Javier Rodríguez-Lozano, and Julia Guerrero-Gironés. Current status and trends in research on caries diagnosis: A bibliometric analysis. *International Journal of Environmental Research and Public Health*, 19(9):5011, 2022.
- [189] James D Bader, Daniel A Shugars, Gary Rozier, Kathleen N Lohr, Arthur J Bonito, Jessica P Nelson, and Anne M Jackman. Diagnosis and management of dental caries. *Evidence report/technology assessment (Summary)*, (36):1–4, 2001.
- [190] DL Carni, Domenico Grimaldi, Paolo F Sciammarella, Alfonso Nastro, Francesco Lamonaca, and Monica Vasile. Measurement technique for the healthy and carious teeth based on thermal analysis. In *2016 IEEE International Symposium on Medical Measurements and Applications (MeMeA)*, pages 1–5. IEEE, 2016.

## References

---

- [191] Jae-Hong Lee, Do-Hyung Kim, Seong-Nyum Jeong, and Seong-Ho Choi. Detection and diagnosis of dental caries using a deep learning-based convolutional neural network algorithm. *Journal of dentistry*, 77:106–111, 2018.
- [192] Mariangela Ivette Guanipa Ortiz, Cristiane de Melo Alencar, Brennda Lucy Freitas De Paula, Marcela Barauna Magno, Lucianne Cople Maia, and Cecy Martins Silva. Accuracy of near-infrared light transillumination (nilt) compared to bitewing radiograph for detection of interproximal caries in the permanent dentition: A systematic review and meta-analysis. *Journal of Dentistry*, 98:103351, 2020.
- [193] Falk Schwendicke, Karim Elhennawy, Sebastian Paris, Philipp Friebertshäuser, and Joachim Krois. Deep learning for caries lesion detection in near-infrared light transillumination images: A pilot study. *Journal of dentistry*, 92:103260, 2020.
- [194] Hartmut Schneider, Martin Ahrens, Michaela Strumpski, Claudia Rüger, Matthias Häfer, Gereon Hüttmann, Dirk Theisen-Kunde, Hinnerk Schulz-Hildebrandt, and Rainer Haak. An intraoral oct probe to enhanced detection of approximal carious lesions and assessment of restorations. *Journal of clinical medicine*, 9(10):3257, 2020.
- [195] Hossein Mohammad-Rahimi, Saeed Reza Motamedian, Mohammad Hossein Rohban, Joachim Krois, Sergio Uribe, Erfan Mahmoudi Nia, Rata Rokhshad, Mohadeseh Nadimi, and Falk Schwendicke. Deep learning for caries detection: A systematic review: DL for caries detection. *Journal of Dentistry*, page 104115, 2022.
- [196] Christopher M Bishop and Nasser M Nasrabadi. *Pattern recognition and machine learning*, volume 4. Springer, 2006.
- [197] Fabian Pedregosa, Gaël Varoquaux, Alexandre Gramfort, Vincent Michel, Bertrand Thirion, Olivier Grisel, Mathieu Blondel, Peter Prettenhofer, Ron Weiss, Vincent Dubourg, et al. Scikit-learn: Machine learning in python. *the Journal of machine Learning research*, 12:2825–2830, 2011.
- [198] Najat Ali, Daniel Neagu, and Paul Trundle. Evaluation of k-nearest neighbour classifier performance for heterogeneous data sets. *SN Applied Sciences*, 1:1–15, 2019.
- [199] Andrea Apicella, Pasquale Arpaia, Mirco Frosolone, and Nicola Moccaldi. High-wearable eeg-based distraction detection in motor rehabilitation. *Scientific Reports*, 11(1):5297, 2021.
- [200] Pedro Domingos and Michael Pazzani. On the optimality of the simple bayesian classifier under zero-one loss. *Machine learning*, 29:103–130, 1997.